



UNIVERSITÀ DEGLI STUDI DI TRIESTE

XXXII CICLO DEL DOTTORATO DI RICERCA IN FISICA

FEMTOSECOND COVARIANCE SPECTROSCOPY

Settore scientifico-disciplinare: FIS/03

DOTTORANDA:

GIORGIA SPARAPASSI

Giorgia Sparapassi

COORDINATORE:

PROF. FRANCESCO LONGO

Francesco Longo

SUPERVISORE DI TESI:

PROF. DANIELE FAUSTI

Daniele Fausti

ANNO ACCADEMICO 2018/2019

Abstract

In this Thesis we develop and characterize the Femtosecond Covariance Spectroscopy technique. This is an approach to spectroscopy that aims at exploiting the information encoded in ultrashort light pulses by nonlinear light-matter interaction processes. We consider each transmitted spectrum of a series of repetitions as a unique realization of the experiment and exploit the nonlinear spectral mixing by calculating the covariance between the frequency resolved intensities. In this work we validate the technique on impulsive stimulated light scattering in a benchmark material, α -quartz, using ultrashort near infrared laser pulses randomized with a pulse shaper. With transmission measurements we retrieve the vibrational spectrum of the sample. The experimental evidence is supported by a theoretical quantum model accounting for the self-heterodyned nature of the inelastic light scattering experiment, resulting in off-diagonal covariance signals. The technique is also applied to time resolved experiments, described in the framework of quantum optics. An intense pump pulse excites the vibrations to a coherent state, and a set of properly time delayed randomized probe pulses explore its evolution through the spectral correlation. Finally we show that the technique is based on a simple yet general and powerful concept which can be adapted to different wavelength ranges and interaction processes.

Index

1 Introduction	1
Reading guide	3
2 Inelastic light scattering	7
Classical description	9
2.1 Single pulse interaction	12
2.1.1 Intensity measurement of randomized pulses	20
2.2 Double pulse interaction	27
2.2.1 Time dependent effects on the refractive index	30
2.2.2 Time dependent inelastic scattering of probe pulses	32
2.2.3 Case study: α -quartz	40
3 Experimental realization	45
3.1 Experimental geometries	45
3.1.1 Laser	47
3.1.2 Pulse shaper	48
3.1.3 Detection	56
3.2 Double stage optical parametric amplification	57
3.3 Measurement of the pulse duration	60
4 Transmission experiments	65
4.1 Full modulation	65
4.2 Half modulation	69
4.2.1 Half modulation with mean value shaping	71
4.2.2 Lineshape analysis	73
4.2.3 Average phase dependence	74
4.3 Cross correlation	75
4.4 Selected peaks randomization	76

4.4.1	Randomization of a single peak	76
4.4.2	Randomization of a pair of peaks	77
4.5	Fluence dependence	79
5	Time resolved experiments	83
5.1	Pump probe experiments	84
5.1.1	Polarization dependence	88
5.1.2	Pulse fluence dependence	91
5.2	Coherent pump and randomized probe	93
5.3	Full modulation	95
5.4	Half modulation	97
5.4.1	Half modulation with mean value shaping	98
5.4.2	Polarization dependence	101
6	Applications	105
6.1	Samples	105
6.2	Wavelength range	107
6.3	Scattering process	113
6.4	Higher order correlation coefficients	115
7	Conclusions	117
	Appendices	121
A	Correlation coefficient	121
A.1	Auto correlation	121
A.2	Cross correlation	123
A.3	Simulated pulses	123
B	Supplementary analytical tools	125
B.1	Notes on the Liouville representation	125
B.2	General solution for a forced harmonic oscillator	129
C	Pulse shaper calibrations	133
C.1	Phase	133
C.2	Amplitude	135
C.3	Frequency	136
	Publications	139

INDEX

v

References

141

1 ■ Introduction

In the work presented in this Thesis, we **use light to investigate matter**. As a matter of fact, we follow this procedure on a daily basis, observing the world, as light, reflected by objects around us, enters our **eyes**. The human eye is a detector, and we could simplify its description by comparing it to a camera. The pupil's diameter is adjusted to limit the amount of light entering the eyeball, whose changing shape allows to optimize the focus of the image onto the retina, where photo-receptor cells, rods and cones, are triggered and send electrical signals to the brain. The light we see has interacted with the objects around us: even if a broad sunlight spectrum reaches the Earth's surface through the atmosphere, objects will typically absorb or transmit a large portion of its components, reflecting the rest. This linear response of an object is what we see and call "colour". Just as it happens with a camera, where a finite *exposure time* is used to properly impress an image onto the film, the eye accumulates light for a finite time interval before sending an image to the brain [1, 2]. We experience the importance of this mechanism whenever, for instance, we look at, or photograph, stars in the night sky.

It is logical to adopt an approach similar to vision when using **light to perform a measurement**. We expose our detector to light reflected or transmitted by a sample for a time interval long enough to obtain a measure of the sample response. In this case, we say that the detector integrates light over some time window. In the framework of ultrafast spectroscopy, *laser light pulses* are employed as a probe. They have a broad spectral bandwidth, and a fixed phase relationship between the components guarantees their coherent sum in short wavepackets [3, 4]. The pulses are produced with a fixed time distance between

each other, therefore integrating over time means averaging over repetitions of the experiment. Even when a single shot acquisition is possible, it is common to perform many repetitions of an experiment to **average the spectra**, to increase the signal to noise ratio.

The electric field of a light pulse can reach a very high amplitude, comparable to that found between nuclei and electrons in an atom [5]. This can give rise, in a medium, to *nonlinear processes*, prompted by the mixing of electric fields at different frequencies and mediated by the sample nonlinear response. Through these interactions one can, for instance, access excited states of a complex material, whose properties and dynamics unveil information about the interplay between different degrees of freedom. Interactions in nonlinear media enable, as well, to produce ultrashort pulses in a laser [6].

The spectral signatures of a nonlinear interaction can be very weak, as they are related to a small cross section, and are often overcome by linear effects. As a consequence, when performing an experiment with the aim of revealing such a tiny signal, noise is seen as a limitation to eliminate. It is common to put much effort into mitigating as much as possible the amount of experimental noise, and to feed the average with as many iterations of the experiment as possible. In doing so we are discarding **spectral features which are unique to each repetition**, which, from an alternative perspective, could be considered as measurements under different conditions. From this point of view, **the deviation of a measured value from its average is source of additional information** [7]. In fact, if treated properly, noise can assist processes [8, 9] and amplify or reveal signals [10]. In this perspective, the average value is no longer a suitable analytical tool to treat the data, and higher order momenta of the data distribution are needed [11–13].

To change the paradigm of average based spectroscopy, it comes as a great advantage that a nonlinear process necessarily involves several spectral components within the pulse bandwidth. In a scattering experiment, this manifests as a mutual dependence of the spectral weight at different points within the spectrum. This coupling, imprinted in the light pulse by the interaction, can be revealed in the form of a statistical correlation. Therefore, in this framework,

only statistical momenta beyond the average are able to convey information on the process.

In this Thesis, we establish this new paradigm under the name of **Femtosecond Covariance Spectroscopy (FCS)**, that aims at revealing the low energy levels of a sample exploiting the correlations imprinted in a light pulse. To validate the technique, we apply it on a transparent sample, α -quartz. The pulses are inelastically scattered by the sample vibrational modes, that have been studied in the past by means of traditional techniques. The scattering results in a global shift of the average transmitted spectrum with respect to the input one, therefore it is not possible to distinguish the contribution of different vibrational modes, nor their symmetry. In FCS instead, the measured single shot spectra are input to a suitable statistical tool. We employ a normalized covariance, the Pearson correlation coefficient ρ , as a two dimensional function of the frequency resolved intensity. We will show that the correlation coefficient carries plenty of information on the interaction process. In the following, we will use ρ as a novel tool to analyze the measured data and extract the sample low energy vibrational spectrum.

■ Reading guide

The Thesis is structured as follows. In **Chapter 2** we present the theoretical tools necessary to describe a third order inelastic light scattering interaction. The chapter is divided in two parts. First, we discuss *single pulse experiments*, with a fully quantum model that allows to calculate the total transmitted field. Moreover, the role of a stochastic spectral phase is discussed and predictions are made on the resulting covariance, computed on randomized pulses before and after their interaction with a sample. This model was developed in collaboration with the group of S. Mukamel (University of California at Irvine) [14]. The second part of the chapter describes *double pulse experiments*, in which a first intense pulse excites the sample out of equilibrium, and the variably delayed pulse probes the material. Within the language of quantum optics, we describe the dynamics of the average transmitted intensity. At the end of the chapter, we calculate the expected time, frequency and symmetry dependent response from the sample under consideration, α -quartz. The work reported

in this part of the chapter stems from a collaboration with the group of F. Benatti (University of Trieste) [15].

The various experimental techniques employed, and the setup built to perform the measurements is discussed in **Chapter 3**. We outline the principles of functioning of the laser, then we describe the pulse shaper, a versatile device that allows to randomize the pulses, and the single shot detectors. Then we present the optical parametric amplification setup, that was employed to frequency convert the pump pulses for a subset of the experiments. At the end of the chapter we describe the frequency resolved optical gating technique, used to measure the duration of ultrafast pulses.

In **Chapter 4** we present single pulse experiments on α -quartz and discuss the results. With the pulse shaper, we modulate randomly the spectral phase or amplitude of each pulse, along the whole spectral bandwidth or portions of it. We retrieve the low energy vibrational modes of the sample. We show the similarities and differences between the vibrational spectra obtained within the different regimes, with a focus on the effect on the signal lineshape. We then study the effect of the application of an average phase jump and of the randomization of selected points within the spectrum. We discuss the appearance of the vibrational features in a cross correlation coefficient. The measurements shown in this chapter and in second part of Chapter 5 were performed with Angela Montanaro [16] and Jonathan Tollerud, respectively a Master student and a PostDoc in our group at the time of the experiments.

In **Chapter 5** we show and discuss the results of experiments conducted with pairs of ultrashort pulses on α -quartz. We begin with double pulse experiments, in which both the pump and the probe pulses are spectrally coherent, and we measure the average transmitted probe spectrum. The vibrational features are retrieved, as they modulate the average response in time. The signal strength is tested by varying the pump or probe fluence, and their relative polarization. These measurements were carried out and analyzed with Filippo Glerean [17], a former Master student in our group. Then we show the results obtained applying a covariance based detection when randomizing the probe pulses. We find that the correlation due to the vibrational modes evolves in time, oscillating.

The strength of this signal is studied in the main modulation configurations adopted in Chapter 4.

Finally, in **Chapter 6**, we consider the adaptation of the technique to different experimental schemes. We start by showing results on a complex material, CuGeO_3 . Then we discuss the application of the covariance based detection to an experiment conducted at a Free Electron Laser, where noise is intrinsic to the generation of X-ray pulses, which inherit a stochastic structure. Finally we present a simulation used to investigate the potential results of a covariance based detection in a inelastic X-ray scattering process involving electronic levels in CuGeO_3 .

In **Appendix A**, we discuss the properties of the correlation coefficient. In **Appendix B** we provide some additional details on the analytical tools of Chapter 2, to aid in the comprehension of the models. In **Appendix C** we briefly describe the calibrations of the pulse shaper.

2 ■ Inelastic light scattering

The field of **nonlinear optics** deals with phenomena which occur when light with very high intensity interacts with a material. It was made possible by the invention of the laser and currently represents a very active research field, being pushed forward by frequent technological developments [3]. Light frequency conversion, amplification, time compression [4] are only a few of the techniques stemming from this field which are now common to the whole condensed matter and quantum optics physics world, sometimes changing the way in which a spectroscopy is performed. It follows that the interaction between matter and light is described using a number of different analytical approaches, relying on the proper approximations depending on the context.

A laser produces high intensity beams, able to drive nonlinear processes that can be exploited to unravel the properties of a material. Of the possible processes taking place during a nonlinear interaction, we will focus on inelastic scattering, when light transmitted or reflected off a sample is frequency converted following an energy exchange with the material. This process is called **Raman scattering** [18]. As we will discuss in this Chapter, the scattered radiation contains specific information on the material. In fact, a number of non-destructive different applications are based on the Raman effect, exploiting its chemical sensitivity to study surfaces, reaction dynamics, photochemical processes, in a wide range of both soft and condensed matter materials, or to frequency convert the radiation [19–22].

When using infrared, visible or ultraviolet light as a means to retrieve the vibrational properties of a solid, the technique is often referred to as vibra-

tional spectroscopy. We will describe materials whose ionic equilibrium positions form a microscopically ordered structure. The normal frequencies of the ionic motion depend on the lattice type as well as on the strength of the chemical bonds involved, and fall in the Terahertz (THz) range. It is possible to probe the vibrational modes with visible and near-infrared radiation even if the ions cannot be driven directly by such electric fields. In fact, the latter oscillate hundreds or thousands of times per second and can only couple with the material's electrons. Nonetheless, the electronic potential is determined by the ionic structure, so that the electronic response is necessarily carrying information on the lattice.

We will discuss the process in the framework of ultrafast spectroscopy, a technique using **broadband pulses** to excite and investigate matter. When this is the case, the nonlinear mixing of the components results in an effective field that can resonantly drive the vibrations. This process is usually referred to as stimulated Raman scattering (SRS) [23] and will be the focus of the first section of the chapter. Several variations of this technique have been proposed, which use combinations of pulses with different duration or frequency content, as Femtosecond SRS (FSRS) [24], coherent Anti-Stokes Raman scattering (CARS) [25] or coherent Stokes Raman scattering (CSRS) [26, 27]. Moreover a SRS experiment can be carried out in combination with microscopy [28, 29], multiple wave mixing techniques [30], even with a single pulse whose properties are appropriately modified [10, 31].

We must also take into account that the duration of an ultrashort pulse is orders of magnitude shorter than the period of one vibrational oscillation. This means that the effective driving field can excite the vibrations *coherently*, in other words in phase. To investigate the dynamics of such excitations, a different time delayed pulse is used as a probe. This *pump-probe* experiment is called, in this context, Impulsive Stimulated Raman Scattering (ISRS) [32–34] and will be the subject of the second part of the chapter. We will make use of classical and quantum formulations, providing different levels of accuracy and depth of description.

Classical description

We consider the interaction of an electric field $E(t)$ with the electrons of a solid. We define their field-induced displacement from the equilibrium position as $r(t)$ and calculate the established electric dipole moment as $\mu(t) = -e \cdot r(t)$, where e is the electron charge. By adding up all the N electric dipoles per unit volume, we get the macroscopic polarization of the material

$$P(t) = N\mu(t), \quad (2.1)$$

which we rewrite in terms of the electric field as

$$P(t) = \epsilon_0 \chi E(t), \quad (2.2)$$

where ϵ_0 is the dielectric permittivity of vacuum and the susceptibility of the material χ encloses the sample contribution to the optical response. For the sake of simplicity, we have taken $P(t)$ and $E(t)$ to be scalar.

When the incident field is weak with respect to the field binding the electrons to the nuclei, the force exerted on the electrons can be approximated by a harmonic perturbation, and the dependence of $r(t)$ on $E(t)$ will be linear. To stronger fields correspond larger displacements, thus anharmonic effects become more significant and corrections have to be made by including higher orders of the field [5]. Hence we expand $P(t)$ in powers of $\chi E(t)$:

$$P(t) = \epsilon_0 [\chi^{(1)} E(t) + \chi^{(2)} E^2(t) + \chi^{(3)} E^3(t) + \dots] \equiv P^{(1)}(t) + P^{(2)}(t) + P^{(3)}(t) + \dots \quad (2.3)$$

The relationship between $P(t)$ and $E(t)$ defines an interaction as *linear* or *non-linear*. Each order of the expansion describes different effects, whose relative magnitude is governed by the strength of the product of n incoming fields and the amplitude of the n^{th} -order susceptibility. The linear term describes, for instance, absorption, while the second term is related to sum and difference frequency generation in materials in which $\chi^{(2)}$ is non-vanishing due to the lattice symmetry. The effects that take place during an inelastic light scattering experiment result from the third-order contribution to the nonlinear polarization $P^{(3)}(t)$, whose relationship with the driving field is depicted in Figure 2.1.

Once an expression for $P^{(3)}(t)$ is computed, directly observable features can be predicted. We are searching for a signal originating from a perturbation in the

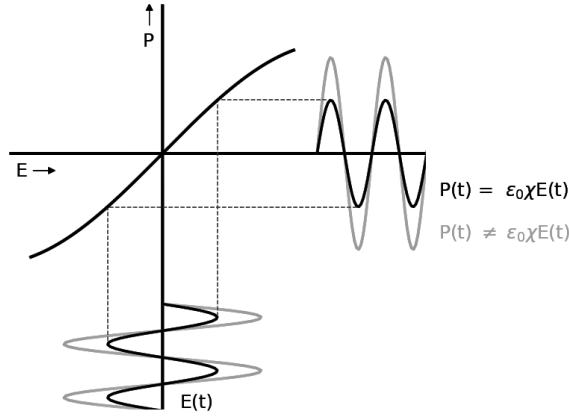


Figure 2.1: Third-order nonlinearity between the driving field and the induced polarization due to anharmonic contributions. Weak and strong electric fields are indicated by black and grey solid lines, respectively. When intense electric fields are applied, the polarization profile no longer matches the sinusoidal profile of the incoming field. Adapted from [5].

electronic polarizability due to the presence of the nuclear motion. Assuming that the driving frequency is far from any electronic resonances, we can express the electric dipole moment $\mu(t)$ in terms of the electronic polarizability $\alpha(t)$ and then expand the latter in a Taylor series of the nuclear coordinate $Q(t)$:

$$\mu(t) = \alpha E(t) = [\alpha_0 + \left(\frac{\delta\alpha}{\delta Q}\right)_0 Q(t) + \dots]E(t), \quad (2.4)$$

where the magnitude of the first order correction to the polarizability $(\delta\alpha/\delta Q)_0$ can be interpreted as the coupling strength between nuclear and electronic coordinates.

In order to work out a simple expression for the resulting polarization, we assume that the vibrational motion can be described by a damped harmonic oscillator with resonance frequency ω_V . For the sake of simplicity, we shall consider a single harmonic nuclear mode, but the extension to multiple modes is straightforward. We also consider only a pair of spectral components inside the bandwidth of the pulse, which we model as plane waves $E_i(t) = A_i e^{-i\omega_i t} + c.c.$ ($i = 1, 2$). The pulse is such that $\omega_1, \omega_2 \gg \omega_V$ and we take $\omega_1 > \omega_2$. If the fields are sufficiently intense for nonlinear effects to take place, the electron cloud will experience oscillations at the fundamental frequencies and also at the difference frequency $\Omega = \omega_1 - \omega_2$. The process will be thus ruled by the following equations

of motion:

$$\begin{cases} \frac{d^2 Q(t)}{dt^2} + 2\gamma \frac{dQ(t)}{dt} + \omega_V Q(t) = \frac{F(t)}{m} \\ F(t) \propto \left(\frac{\delta \alpha}{\delta Q} \right)_0 [f e^{-i\Omega t} + c.c.] \end{cases} \quad (2.5)$$

where γ is the damping constant, m the reduced mass of the nuclear oscillator, and f the force amplitude. The analytic solution of Equation 2.5 [5] yields the time-varying nuclear displacement

$$Q(t) \propto \left(\frac{\delta \alpha}{\delta Q} \right)_0 \frac{f e^{-i\Omega t}}{\omega_V^2 - \Omega^2 - 2i\Omega\gamma} + c.c. \quad (2.6)$$

The nuclear mode is thus driven into resonance by the combined action of the two incoming fields. The amplitude of the nuclear displacement is directly proportional to the amplitude of the driving fields and to the coupling strength between the electronic and the vibrational degrees of freedom. Furthermore, nuclear oscillation are resonantly enhanced when $\Omega = \omega_V$.

The modulation of the nuclear coordinate affects the optical properties of the material. Combining equations 2.1, 2.4 and 2.6 we compute the polarization of the material following the excitation:

$$\begin{aligned} P(t) &= N[\alpha_0 + \left(\frac{\delta \alpha}{\delta Q} \right)_0 Q(t) + \dots][E_1(t) + E_2(t)] = \\ &= P_L + P(\omega_1)e^{-i\omega_1 t} + P(\omega_2)e^{-i\omega_2 t} + P(\omega_2 - \Omega)e^{-i(\omega_2 - \Omega)t} + P(\omega_1 + \Omega)e^{-i(\omega_1 + \Omega)t} \\ &\equiv P_L + P^{(3)} \end{aligned} \quad (2.7)$$

which contains a linear contribution due to the constant polarizability α_0 , and a nonlinear contribution due to $P^{(3)}$ (the third-order nonlinear term due to the driven oscillation and proportional to $(\delta\alpha/\delta Q)_0$) [5]. In $P^{(3)}$ we recognize two frequency components shifted from the incoming ones. They are retained in the measured signal, which is generated by the nonlinear polarization and can be calculated using Maxwell's equations [35]

$$E_s(l, t) = \frac{2\pi i}{n(\omega_s)} \frac{\omega_s}{c} l P^{(3)}(t) \text{sinc} \left(\frac{\Delta k l}{2} \right) e^{i \frac{\Delta k l}{2}} \quad (2.8)$$

with $\Delta k \equiv |k_s - k'_s|$ the wavevector mismatch between the signal and the incident field and $n(\omega_s)$ the equilibrium refractive index at the signal frequency.

When employing broadband pulses, the sidebands (fourth and fifth terms of Equation 2.7) overlap with the rest of the pulse; moreover the process takes place for multiple pairs of frequencies within the bandwidth of the pulse. For this reason it is experimentally challenging to distinguish the signal in transmission experiments with broadband pulses. This experimental configuration has, nonetheless, the advantage of providing an intrinsic amplification of the signal. In fact the total detected intensity is the superposition of the signal field $E_s(t)$ with the field within the pulse spectrum at the same frequency of the signal, $E_0(t)$. The total intensity resulting from the sum reads

$$\begin{aligned} I(t) &= \frac{n(\omega_s)c}{4\pi} |E_0(t) + E_s(t)|^2 = \\ &= I_0(t) + I_s(t) + 2\frac{n(\omega_s)c}{4\pi} \Re e [E_0^*(t) \cdot E_s(t)]. \end{aligned} \quad (2.9)$$

Since the signal intensity $I_s(t)$ is usually much weaker than the intensity of the field at the same frequency, $I_0(t)$, the second term in Equation 2.9 can be neglected. $I_0(t)$ is estimated as the incident intensity, therefore the meaningful contribution to the signal is the interference term, which is linear in the polarization. Within several experimental configurations adopted in nonlinear optics, an external reference field, the *local oscillator*, is overlapped to the signal to *heterodyne* it. In our particular case, the local oscillator coincides with the driving field. For this reason the signal is said to be **self-heterodyned**.

2.1 ■ Single pulse interaction

As mentioned above, a $n+1$ process is commonly described as a two step process. First, the sample is exposed to n fields, which induce a n^{th} order polarization in the material. In the second step, the nonlinear polarization acts as a source, generating the signal, which is revealed by an external local oscillator. In the present case, the local oscillator is part of the incident field. This peculiarity of the experiment is conveniently described by developing **a theoretical framework in which the $n+1$ fields involved in a $\chi^{(n)}$ process, including the signal, are treated on the same level**. We will use a fully quantum approach, in which both the light field and the vibrational fields are quantized. In particular, the sample is described in terms of energy levels, rather than susceptibilities, in order to formulate the nonlinear wave mixing process in terms of transition amplitudes between the material quantum states. Using such a scheme, we

establish a clear picture of the underlying microscopic processes [36–38]. Because of the fact that in most practical cases the sample quantum state is not accessible, it is studied by means of the density operator $\hat{\rho}$ and the density matrix ρ (the matrix representation of $\hat{\rho}$). This operator allows to associate a probability to each of the sample possible quantum "pure" states. Through $\hat{\rho}$, we calculate the expected value of any operator, and its time evolution. In particular, to perform the latter task, the time evolution of the density operator needs to be calculated. This is obtained through the Liouville – Von Neumann Equation (Equation B.6), that can be recast in the same form of a Schrödinger equation, therefore treated using the powerful formalism of quantum mechanics. To perform this transformation, we introduce the Liouville space, whose elements are the the so called superoperators, defined by their action on Hilbert space operators (Equation B.7). Once this notation is introduced, we can switch to the interaction picture in the Liouville space. A further description of this analytical tools is given in Appendix B.

The quantized **electric field** is completely described by a wavefunction, denoted by $|\Psi_F\rangle$. The expectation value of the electric field is $\langle\Psi_F|\hat{E}(\mathbf{r},t)|\Psi_F\rangle$, where

$$\hat{E}(\mathbf{r},t) = \hat{\mathcal{E}}(\mathbf{r},t) + \hat{\mathcal{E}}^\dagger(\mathbf{r},t) \quad (2.10)$$

is the optical electric field operator, whose positive-frequency component reads (in cgs units)

$$\hat{\mathcal{E}}(\mathbf{r},t) = \sum_s \left(\frac{2\pi\hbar\omega_s}{v} \right)^{1/2} \hat{a}_s e^{i(\mathbf{k}_s \cdot \mathbf{r} - \omega_s t)}. \quad (2.11)$$

We have indicated by v the quantization volume and by \hat{a}_s (\hat{a}_s^\dagger) the boson annihilation (creation) operator of the mode s , which satisfies the boson commutation relation

$$[\hat{a}_s, \hat{a}_{s'}^\dagger] = \delta_{ss'} \quad (2.12)$$

The action of the bosonic operators on the field is defined as follows:

$$\begin{aligned} \hat{a}_s^\dagger |\Psi_F^s(n)\rangle &= n_s^{1/2} |\Psi_F^s(n+1)\rangle \\ \hat{a}_s |\Psi_F^s(n)\rangle &= (n_s - 1)^{1/2} |\Psi_F^s(n-1)\rangle \end{aligned} \quad (2.13)$$

where n_s is the photon occupation number of the mode s . We assume the field to be, initially, in a coherent state $|\Psi_C\rangle = A_0 e^{\sum_s \hat{a}_s^\dagger \alpha_s} |0\rangle$ with $A_0 = \exp\left(-\sum_s |\alpha_s|^2\right)$, where α_s is the eigenvalue of the photon annihilation operator on the coherent

state ($\hat{a}_s |\Psi_C\rangle = \alpha_s |\Psi_C\rangle$), and $|0\rangle$ is the vacuum state. The expectation value of the positive frequency term of the field is then:

$$\mathcal{E}(\mathbf{r}, t) = \sum_s \left(\frac{2\pi\hbar\omega_s}{\Omega} \right)^{1/2} \alpha_s e^{i(\mathbf{k}_s \cdot \mathbf{r} - \omega_s t)} \quad (2.14)$$

The photon occupation number operator $\hat{\mathcal{N}}$ is defined as

$$\hat{\mathcal{N}} \equiv \sum_s \hat{a}_s^\dagger \hat{a}_s \quad (2.15)$$

Because of the fact that the index s runs over frequency modes within the bandwidth, the eigenvalue of $\hat{\mathcal{N}}$ is the total number of photons (for all modes).

The **total Hamiltonian** of a molecule interacting with an optical electric field, assuming that the magnetic degrees of freedom are negligible and the coupling happens only through the electric charges, reads

$$\hat{H} = \hat{H}_M + \hat{H}_F + \hat{H}_{int} \quad (2.16)$$

where \hat{H}_M represents the free unperturbed molecule, \hat{H}_F the field degrees of freedom, and \hat{H}_{int} the interaction between the molecule and the field. The electric field Hamiltonian is $\hat{H}_F = \sum_s \hbar\omega_s \hat{a}_s^\dagger \hat{a}_s$ [39].

The **interaction term** represents the energy required to establish an electric dipole in the material, in classical terms $U(t) = -\vec{\mu} \cdot \vec{E}(t)$. The electric dipole operator $\hat{\mu}$ reads

$$\hat{\mu} = \hat{V} + \hat{V}^\dagger, \quad (2.17)$$

with \hat{V}^\dagger (\hat{V}) being the creation (annihilation) operator of an excitation, written, in the dipole approximation¹ as

$$\hat{V} = \sum_a \sum_{b>a} \mu_{ab} |a\rangle \langle b|. \quad (2.18)$$

Neglecting the fast oscillating terms (Rotating Wave Approximation, RWA), we finally compute the interaction Hamiltonian

$$\hat{H}_{int}(t) = \hat{\mathcal{E}}(t) \hat{V}^\dagger + \hat{\mathcal{E}}^\dagger(t) \hat{V}. \quad (2.19)$$

¹Dipole approximation: when the optical wavelength is much greater than the sample dimensions, the field can be considered constant across the sample.

In the quantum approach under consideration, and in the interaction picture, a self heterodyned signal is obtained as the **net change in the number of photons** between the initial (i) and the final (f) states [38]

$$S \equiv \int dt \frac{d}{dt} \langle \hat{\mathcal{N}} \rangle_\rho = \langle \hat{\mathcal{N}} \rangle_f - \langle \hat{\mathcal{N}} \rangle_i. \quad (2.20)$$

In the last Equation, $(\dots)_\rho$ denotes the expectation value with respect to the total density matrix of the system (a trace as in Equation B.3), while $\langle \dots \rangle$ is an ensemble average over the non-interacting density matrix. Using perturbation theory $(\dots)_\rho$ can be expanded in terms of $\langle \dots \rangle$.

We denote by the subscript H operators in the Heisenberg picture. In this space the density matrix is constant, and the time derivative in Equation 2.20 can be evaluated as

$$\frac{d}{dt} \langle \hat{\mathcal{N}} \rangle_\rho \equiv \left\langle \frac{d}{dt} \hat{\mathcal{N}}_H \right\rangle = \left\langle \sum_s \frac{i}{\hbar} \left[\hat{H}_{int}(t), \hat{a}_{s,H}^\dagger \hat{a}_{s,H} \right] \right\rangle. \quad (2.21)$$

We have used the Heisenberg equations of motion, which make use of the total Hamiltonian, but in this case only the commutator with \hat{H}_{int} survives. By substituting the expression of the interacting Hamiltonian (Equation 2.19) and that of the electric field operator (Equation 2.11), we obtain an equation for commutators between bosonic operators, which can be rewritten as:

$$S = \frac{2}{\hbar} \Im \int dt \langle \hat{\mathcal{E}}^\dagger(t) \hat{V} \rangle_\rho \quad (2.22)$$

Equation 2.22 can be further manipulated to obtain a more explicit expression [37] by considering the perturbative expansion (Equation B.21) of the time dependent density operator (whose evolution is ruled by Equation B.13).

We express the Hamiltonian in the last Equation as a combination of "left" and "right" Liouville space superoperators [38], which are defined by the action:

$$\begin{aligned} \hat{A}_L \hat{X} &\equiv \hat{A} \hat{X} \\ \hat{A}_R \hat{X} &\equiv \hat{X} \hat{A} \end{aligned} \quad (2.23)$$

where on the right-hand side the operators \hat{A} and \hat{X} are in the Hilbert space. The linear combinations "+" or "-" superoperators can be constructed as

$$\hat{A}_\pm \equiv \frac{1}{\sqrt{2}} [\hat{A}_L \pm \hat{A}_R]. \quad (2.24)$$

Because of the equivalence $\hat{A}_- \Leftrightarrow \mathbb{A}$, we rewrite the Hamiltonian in Equation B.13 as a "-" operator. Combining the new notation to the evolution of the density operator, Equation 2.22 becomes:

$$S = \frac{2}{\hbar} \mathfrak{Tr} \int dt \left\langle \hat{\mathcal{E}}_L^\dagger(t) \hat{V}_L(t) \mathcal{T} e^{-\frac{i}{\hbar} \int_{-\infty}^t d\tau \sqrt{2} \mathcal{H}_{int-}(\tau)} \right\rangle \quad (2.25)$$

where \mathcal{H}_{int-} is the "-" superoperator corresponding to \hat{H}_{int} (Equation 2.19) and the time dependence of the dipole superoperator comes from the transformation to the interaction picture. $\hat{\mathcal{E}}_L^\dagger$ is the negative frequency component of the electric field operator and \hat{V}_L the positive frequency component of the electric dipole operator, both expressed in the "left"/"right" Liouville representation.

We are interested in the spectrally dispersed signal $S(\omega)$, representing the frequency resolved intensity. To calculate $S(\omega)$, we Fourier transform the negative-frequency component of the electric field operator and then add a frequency gating $\delta(\omega - \bar{\omega})$. By substituting $\bar{\omega} \rightarrow \omega$ we get:

$$S(\omega) = \frac{2}{\hbar} \mathfrak{Tr} \int dt e^{i\omega t} \left\langle \hat{\mathcal{E}}_L^\dagger(\omega) \hat{V}_L(t) \mathcal{T} e^{-\frac{i}{\hbar} \int_{-\infty}^t d\tau \sqrt{2} \mathcal{H}_{int-}(\tau)} \right\rangle \quad (2.26)$$

By using Equation 2.4, we can write the non-resonant polarization (with respect to electronic absorptions) in terms of the polarizability $\alpha(t)$:

$$S(\omega) = \frac{2}{\hbar} \mathfrak{Tr} \int dt e^{i\omega t} \left\langle \hat{\mathcal{E}}_L^\dagger(\omega) \hat{\mathcal{E}}_L(t) \alpha_L(t) \mathcal{T} e^{-\frac{i}{\hbar} \int_{-\infty}^t d\tau \sqrt{2} \mathcal{H}_{int-}(\tau)} \right\rangle \quad (2.27)$$

The last equation (as well as Equation 2.25) is a general expression for a heterodyned signal in the fully quantum approach, applies to both spontaneous and stimulated signals, and contains all orders in the fields. The different terms in the perturbative expansion represent the various possible optical signals. In the following, we shall ignore spontaneous emission and consider only stimulated scattering [38]. We perform a perturbative expansion of Equation 2.27, by considering the explicit action of the time ordering operator \mathcal{T} . Since the 0^{th} -order contains only one light-matter interaction (α_L), it vanishes when traced over the non-interacting density matrix. We thus expand Equation 2.27 to the first order as:

$$S(\omega) = \frac{2}{\hbar} \mathfrak{Tr} \int dt e^{i\omega t} \left\langle \hat{\mathcal{E}}_L^\dagger(\omega) \hat{\mathcal{E}}_L(t) \alpha_L(t) \left(-\frac{i}{\hbar} \sqrt{2} \right) \int_{-\infty}^t d\tau \mathcal{H}_{int-}(\tau) \right\rangle \quad (2.28)$$

By recalling the definition of the "-" superoperator (Equation B.7), the first-

order contribution to the signal splits into two terms:

$$\begin{aligned} S(\omega) &= \frac{2}{\hbar^2} \Re e \int dt e^{i\omega t} \left\langle \hat{\mathcal{E}}_L^\dagger(\omega) \hat{\mathcal{E}}_L(t) \alpha_L(t) \left[\int_{-\infty}^t d\tau \mathcal{H}_{int,R}(\tau) - \int_{-\infty}^t d\tau \mathcal{H}_{int,L}(\tau) \right] \right\rangle \\ &\equiv S_a(\omega) - S_b(\omega) \end{aligned} \quad (2.29)$$

The first term (S_a) involves interactions from both the left and the right, while the second one (S_b) only interactions from the left. We can calculate them using the *Closed-Time-Path-Loop* (CTPL) representation, a diagrammatic expansion that is most suitable when the signal is expressed in the frequency domain [37]. The diagram on the left in Figure 2.2 represents the energy loss of the electric field while the one on the right represents its energy gain [32].

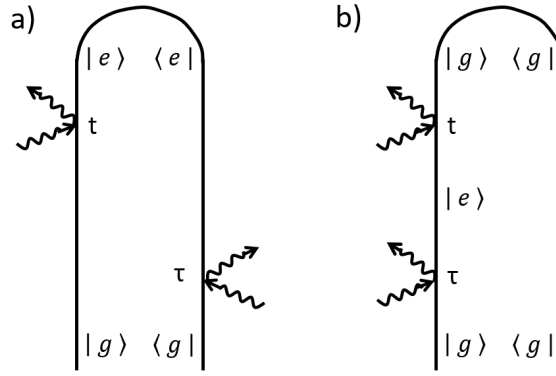


Figure 2.2: CTPL diagrammatic representation of the stimulated Raman scattering process. The diagram a) and b) represent the term $S_a(\omega)$ (Stokes process) and $S_b(\omega)$ (Anti-Stokes process) respectively.

We start by calculating S_a :

$$\begin{aligned} S_a(\omega) &= \frac{2}{\hbar^2} \Re e \int dt e^{i\omega t} \left\langle \hat{\mathcal{E}}_L^\dagger(\omega) \hat{\mathcal{E}}_L(t) \alpha_L(t) \int_{-\infty}^t d\tau \mathcal{H}_{int,R}(\tau) \right\rangle \\ &= \frac{2}{\hbar^2} \Re e \int dt e^{i\omega t} \left\langle \hat{\mathcal{E}}_L^\dagger(\omega) \left[\int \frac{d\omega_1 d\omega_2}{(2\pi)^2} e^{-i(\omega_1 + \omega_2)t} \hat{\mathcal{E}}_L(\omega_1) \alpha_L(\omega_2) \right] \times \right. \\ &\quad \left. \times \int_{-\infty}^t d\tau \int \frac{d\omega_3 d\omega_4 d\omega_5}{(2\pi)^3} e^{-i(-\omega_3 + \omega_4 + \omega_5)\tau} \hat{\mathcal{E}}_R^\dagger(\omega_3) \hat{\mathcal{E}}_R(\omega_4) \alpha_R(\omega_5) \right\rangle \end{aligned} \quad (2.30)$$

where in the second step we have substituted the expression of the interaction Hamiltonian in terms of α and Fourier transformed both the electric field operators and the polarizabilities. Since the average $\langle \dots \rangle$ is performed over the unperturbed density matrix, we can now separate the sample degrees of free-

dom (denoted by η) from the field ones (denoted by ϕ):

$$S_a(\omega) = \frac{2}{\hbar^2} \Re \iint \frac{d\omega_1 d\omega_2 d\omega_3 d\omega_4 d\omega_5}{(2\pi)^5} \left\langle \hat{\mathcal{E}}_L^\dagger(\omega) \hat{\mathcal{E}}_L(\omega_1) \hat{\mathcal{E}}_R^\dagger(\omega_3) \hat{\mathcal{E}}_R(\omega_4) \right\rangle_\phi \times \underbrace{\langle \alpha_L(\omega_2) \alpha_R(\omega_5) \rangle_\eta \int dt e^{i(\omega - \omega_1 - \omega_2)t} \int_{-\infty}^t d\tau e^{-i(-\omega_3 + \omega_4 + \omega_5)\tau}}_{\equiv I} \quad (2.31)$$

The average over ϕ does not include the stochastic degrees of freedom over which our covariance-based analysis is performed, it refers only to the light field.

We can now separately solve the integrals over t and τ :

$$\begin{aligned} I &= \int dt e^{i(\omega - \omega_1 - \omega_2)t} \left(\lim_{\gamma \rightarrow 0} \frac{i e^{-i(-\omega_3 + \omega_4 + \omega_5)t}}{-\omega_3 + \omega_4 + \omega_5 - i\gamma} \right) \\ &= i \lim_{\gamma \rightarrow 0} \int dt \frac{e^{-i(-\omega_3 + \omega_4 + \omega_5 + \omega_1 + \omega_2 - \omega)t}}{-\omega_3 + \omega_4 + \omega_5 - i\gamma} \\ &= i \lim_{\gamma \rightarrow 0} \frac{2\pi \delta(\omega_1 + \omega_2 + \omega_4 + \omega_5 - \omega_3 - \omega)}{-\omega_3 + \omega_4 + \omega_5 - i\gamma} \end{aligned} \quad (2.32)$$

We span the polarizability in the energy eigenstates of the material. We consider a two-level system (the vibrational ground state is denoted by $|g\rangle$, while the excited one by $|e\rangle$) with energy difference $\hbar\Omega$. The term involving the polarizability is then given by:

$$\begin{aligned} \langle \alpha_L(\omega_2) \alpha_R(\omega_5) \rangle_\eta &= \text{Tr}(\alpha(\omega_2) \hat{\rho} \alpha(\omega_5)) \\ &= \text{Tr}(\alpha(\omega_2) |g\rangle \langle g| \alpha(\omega_5)) \\ &= \langle e | \alpha(\omega_2) | g \rangle \langle g | \alpha(\omega_5) | e \rangle \\ &= |\alpha_{ge}|^2 (2\pi)^2 \delta(\omega_2 + \Omega) \delta(\omega_5 - \Omega) \end{aligned} \quad (2.33)$$

where in the last step we have expressed the average in the Kramers-Heisenberg (KH) form (a generalized Fermi golden rule) [37]. We have denoted by α_{ge} the polarizability transition amplitude between the two states. The generalized KH form allows to recast heterodyne optical signals in terms of the scattering amplitudes rather than the standard nonlinear susceptibilities. The equivalence of the two formulations is discussed and demonstrated in [37]. We prefer to take the KH approach as it reveals the process from the point of view of the sample. By solving the Dirac deltas, we get the final expression for S_a :

$$S_a = \lim_{\gamma \rightarrow 0} \frac{2 |\alpha_{ge}|^2}{\hbar^2} \Im \iint \frac{d\omega_1 d\omega_2}{(2\pi)^2} \frac{\mathcal{E}^*(\omega) \mathcal{E}(\omega + \omega_1 - \omega_2) \mathcal{E}^*(\omega_1) \mathcal{E}(\omega_2)}{-\omega_1 + \omega_2 + \Omega - i\gamma} \quad (2.34)$$

where we have replaced the electric field operators with their expectation values (Equation B.2), since we detect intense fields (i.e. fields in a classical regime). The term S_b can be evaluated similarly, with the term involving the polarization being

$$\begin{aligned} \langle \alpha_L(\omega_2) \alpha_L(\omega_5) \rangle_\eta &= \langle g | \alpha(\omega_2) | e \rangle \langle e | \alpha(\omega_5) | g \rangle \\ &= |\alpha_{ge}|^2 (2\pi)^2 \delta(\omega_2 - \Omega) \delta(\omega_5 + \Omega) \end{aligned} \quad (2.35)$$

since all the operators act from the left in S_b . By recombining the two terms, we get:

$$\begin{aligned} S(\omega) &= \lim_{\gamma \rightarrow 0} \frac{2 |\alpha_{ge}|^2}{\hbar^2} \Im \iint \frac{d\omega_1 d\omega_2}{(2\pi)^2} \mathcal{E}^*(\omega) \mathcal{E}(\omega + \omega_1 - \omega_2) \mathcal{E}^*(\omega_1) \mathcal{E}(\omega_2) \times \\ &\quad \times \left[\frac{1}{\omega_2 - \omega_1 + \Omega - i\gamma} - \frac{1}{\omega_2 - \omega_1 - \Omega - i\gamma} \right] \end{aligned} \quad (2.36)$$

We apply the Sokhotski-Plemelj theorem

$$\lim_{\gamma \rightarrow 0} \frac{1}{\omega - i\gamma} = \mathcal{P} \frac{1}{\omega} + i\pi \delta(\omega) \quad (2.37)$$

to explicitly calculate the terms within the square brackets. We introduced the symbol \mathcal{P} for the principal value. Equation 2.36 should now be split into four distinct integrals, two involving the principal values and two involving the Dirac deltas. However, since $\mathcal{E}^*(\omega) \mathcal{E}(\omega + \omega_1 - \omega_2) \mathcal{E}^*(\omega_1) \mathcal{E}(\omega_2)$ is smooth and even around the poles of the integrand function, the principal values vanish when the integration over $\omega_{1,2}$ is performed. Therefore, by considering the action of the Dirac deltas only, we get the final expression of the signal:

$$\begin{aligned} S(\omega) &= \frac{|\alpha_{ge}|^2}{\hbar^2} \Re e \int \frac{d\omega'}{2\pi} \times \\ &\quad \times [\mathcal{E}^*(\omega) \mathcal{E}(\omega + \Omega) \mathcal{E}^*(\omega') \mathcal{E}(\omega' - \Omega) - \mathcal{E}^*(\omega) \mathcal{E}(\omega - \Omega) \mathcal{E}^*(\omega') \mathcal{E}(\omega' + \Omega)] \end{aligned} \quad (2.38)$$

The equation above should not be confused with the total frequency resolved intensity we measure in the experiment. Recalling that we have worked out $S(\omega)$ starting from Equation 2.20, $S(\omega)$ does not probe any background: the signal in Equation 2.38 accounts only for intensity fluctuations from the average.

We have not yet discussed the **temperature dependence** of the system. If the sample has a finite temperature, two more processes must be considered, since the system can be initially either in the ground state or in the vibrationally excited one. This is the physical meaning behind the Stokes and anti-Stokes

processes: when the sample is in the vibrational ground state, it can only take energy from the pulses; conversely when the excited state is populated, energy can be given to the pulses. If we assume the system to be at thermal equilibrium of inverse temperature β , the temperature dependence can be included by considering the thermal population given by the Boltzmann factor:

$$\begin{cases} p_g = \frac{1}{1+e^{-\beta\hbar\Omega}} & \text{for the ground state} \\ p_e = \frac{1}{1+e^{+\beta\hbar\Omega}} & \text{for the first excited state} \end{cases} \quad (2.39)$$

The Anti-Stokes contribution is identical to 2.38 with a minus sign, as the substitution $\Omega \rightarrow -\Omega$ must be made. The overall signal, including the thermal factor $p_{ge}(\beta) = p_g - p_e$, reads:

$$\begin{aligned} S(\omega; \Gamma) = & \frac{|\alpha_{ge}|^2 p_{ge}(\beta)}{\hbar^2} \Re \int \frac{d\omega'}{2\pi} \times \\ & \times [\mathcal{E}^*(\omega)\mathcal{E}(\omega + \Omega)\mathcal{E}^*(\omega') \mathcal{E}(\omega' - \Omega) - \mathcal{E}^*(\omega)\mathcal{E}(\omega - \Omega)\mathcal{E}^*(\omega') \mathcal{E}(\omega' + \Omega)] \end{aligned} \quad (2.40)$$

In the above equation we have introduced Γ , which includes all the field parameters that can be tuned in the experiment. Note that this equation is consistent with the fact that, if the temperature is infinite, the Stokes and Anti-Stokes processes contribute equally and the variation of the number of photons is zero.

2.1.1 ■ Intensity measurement of randomized pulses

We start from the expression for the frequency dependent signal in Equation 2.40 that is expected when the SRS process takes place. This expression has general validity for a single pulse experiment with classical fields. We will now calculate the signal when the electric fields have a **random spectral phase**, a crucial ingredient in our approach.

We consider the a slow transition towards the stochastic state, by assuming the random spectral phase to have a Gaussian correlation function:

$$\langle \phi(\omega_1) \phi(\omega_2) \rangle \propto e^{-\left(\frac{\omega_1 - \omega_2}{\Delta_{corr}}\right)^2} \quad (2.41)$$

where $\phi(\omega_i)$ is the spectral phase at frequency ω_i and $\langle \dots \rangle$ denotes the average over repeated measurements. The *correlation length* of the phase fluctuations,

Δ_{corr} , can be experimentally controlled. This quantity sets an inferior limit for the frequency correlation that can be revealed, thus represents the spectral resolution of the method. In the following we will consider $\Omega \gg \Delta_{corr}$, so that $\varphi(\omega_i)$ and $\varphi(\omega_i \pm \Omega)$ can be safely considered as statistically independent variables. This treatment is not limited to Gaussian correlation functions only: it could be generalized to any kind of decaying correlation functions whose scale is defined by a characteristic length.

Under these conditions, we can rewrite the signal by explicitly splitting each factor \mathcal{E} into its envelope $E(\omega)$ and its spectral phase $\varphi(\omega)$. By gathering the phase factors of each four-field product and taking the real part of the formula, we get:

$$\begin{aligned} S(\omega; \Gamma) = & \frac{|\alpha_{ge}|^2 p_{ge}(\beta)}{\hbar^2} \int \frac{d\omega'}{2\pi} \times \\ & \times [E^*(\omega)E(\omega + \Omega)E^*(\omega')E(\omega' - \Omega) \cos(\gamma) - E^*(\omega)E(\omega - \Omega)E^*(\omega')E(\omega' + \Omega) \cos(\beta)] \end{aligned} \quad (2.42)$$

where we have defined the following phases:

$$\begin{cases} \gamma = \varphi(\omega + \Omega) - \varphi(\omega) + \varphi(\omega' - \Omega) - \varphi(\omega') \\ \beta = \varphi(\omega - \Omega) - \varphi(\omega) + \varphi(\omega' + \Omega) - \varphi(\omega') \end{cases} \quad (2.43)$$

We can now compute the **average signal**, which we measure by taking the mean over the subsequent repetitions of the transmission experiment, each pulse having with a unique random spectral phase. Since we have assumed that $\Omega \gg \Delta_{corr}$, the average values of $\cos(\gamma)$ and $\cos(\beta)$ vanish (and so does the average value of the signal) unless γ and β are both zero, in formulae unless:

$$\begin{cases} \omega' = \omega + \Omega & \text{for the first sum} \\ \omega' = \omega - \Omega & \text{for the second sum} \end{cases} \quad (2.44)$$

We can thus write the average transmitted signal as:

$$\langle S(\omega; \Gamma) \rangle = \frac{|\alpha_{ge}|^2 p_{ge}(\beta)}{2\pi\hbar^2} \{ |E(\omega)E(\omega + \Omega)|^2 - |E(\omega)E(\omega - \Omega)|^2 \} \quad (2.45)$$

where the average is calculated over the stochastic degrees of freedom, included in the distribution Γ . Equation 2.45 correctly describes the spectral (red or blue) shift due to the inelastic scattering [32]. As we mentioned in the introduction, when the pulse spectrum is broad, as is the case for ultrashort pulses, similar

shifts involve all the spectral components within the pulse bandwidth, so that it is not possible in general to retrieve the vibrational excitation spectrum.

We now calculate explicitly the **frequency covariance on the transmitted field**, with respect to the stochastic degrees of freedom, and get a sense of what to expect from the experiment. We start by the average of a product of signals:

$$\begin{aligned} \langle S(\omega_i; \Gamma) S(\omega_j; \Gamma) \rangle &= \frac{|\alpha_{ge}|^4 p_{ge}^2(\beta)}{\hbar^4} \int \frac{d\omega'}{2\pi} \int \frac{d\omega''}{2\pi} \\ &\langle [E^*(\omega_i)E(\omega_i + \Omega)E^*(\omega')E(\omega' - \Omega) \cos \gamma'_i - E^*(\omega_i)E(\omega_i - \Omega)E^*(\omega')E(\omega' + \Omega) \cos \beta'_i] \\ &[E^*(\omega_j)E(\omega_j + \Omega)E^*(\omega'')E(\omega'' - \Omega) \cos \gamma''_j - E^*(\omega_j)E(\omega_j - \Omega)E^*(\omega'')E(\omega'' + \Omega) \cos \beta''_j] \rangle \end{aligned} \quad (2.46)$$

where we have used the expression of the signal in Equation 2.42. We have introduced the symbols γ_r^s and β_r^s , where the subscript $r = (i, j)$ refers to the pair of frequency factors $\omega_{i,j}$ on which the average is calculated, and the superscript $s = (', '')$ refers to the corresponding integration variables. The product within the angle brackets gives rise to four distinct terms

$$\begin{aligned} \text{a) } \langle \cos \gamma'_i \cos \gamma''_j \rangle &= \frac{1}{2} \langle \cos(\gamma'_i + \gamma''_j) + \cos(\gamma'_i - \gamma''_j) \rangle \\ \text{b) } \langle \cos \beta'_i \cos \beta''_j \rangle &= \frac{1}{2} \langle \cos(\beta'_i + \beta''_j) + \cos(\beta'_i - \beta''_j) \rangle \\ \text{c) } \langle \cos \gamma'_i \cos \beta''_j \rangle &= \frac{1}{2} \langle \cos(\gamma'_i + \beta''_j) + \cos(\gamma'_i - \beta''_j) \rangle \\ \text{d) } \langle \cos \beta'_i \cos \gamma''_j \rangle &= \frac{1}{2} \langle \cos(\beta'_i + \gamma''_j) + \cos(\beta'_i - \gamma''_j) \rangle \end{aligned} \quad (2.47)$$

where we have used the Werner formula for the product of cosines. Equation 2.46 thus splits into eight terms. Each term in Equation 2.47 yields delta functions upon averaging: we focus on those that can be satisfied simultaneously by multiple terms. Respectively, equalities in a) and b) and in c) and d) give rise to the conditions:

$$\begin{aligned} \text{i) } \langle \cos(\gamma'_i - \gamma''_j) \rangle &= \delta(\omega'' - \omega') \delta(\omega_j - \omega_i) \\ \text{ii) } \langle \cos(\gamma'_i + \beta''_j) \rangle &= \delta(\omega' - \omega'' - \Omega) \delta(\omega_i - \omega_j + \Omega) \end{aligned} \quad (2.48)$$

The terms which contribute with contractions of type i) are trivial, since represent an autocorrelation. Instead, contractions of type ii) represent a correlation between pairs of frequencies separated by Ω . We explicitly calculate the signal

coming from the contributions of kind ii):

$$\begin{aligned}
\langle S(\omega_i; \Gamma) S(\omega_j; \Gamma) \rangle_{\gamma'_i + \beta''} &= \frac{|\alpha_{ge}|^4 p_{ge}^2(\beta)}{\hbar^4} \int \frac{d\omega'}{2\pi} \int \frac{d\omega''}{2\pi} \delta(\omega' - \omega'' - \Omega) \delta(\omega_i - \omega_j + \Omega) \\
&E^*(\omega_i) E(\omega_i + \Omega) E^*(\omega') E(\omega' - \Omega) E^*(\omega_j) E(\omega_j - \Omega) E^*(\omega'') E(\omega'' + \Omega) \\
&= \frac{|\alpha_{ge}|^4 p_{ge}^2(\beta)}{\hbar^4} |E(\omega_i) E(\omega_i + \Omega)|^2 \int \frac{d\omega'}{(2\pi)^2} |E(\omega') E(\omega' - \Omega)|^2 \delta(\omega_i - \omega_j + \Omega)
\end{aligned} \tag{2.49}$$

We remind that two frequencies whose distance is smaller or comparable to Δ_{corr} are statistically dependent, therefore the signal around the "lines" $\omega_i = \omega_j$ and $\omega_i = \omega_j \pm \Omega$ is blurred (in other words the deltas above should be considered as having a finite width)². In any case, the key concept resulting from the discussion above is that **the distances between the components giving rise to non vanishing features in the correlation match the vibrational frequencies of the sample**. Therefore, by simply scaling one frequency axis to the central value of the probe spectrum, one can directly map the correlation coefficient to the sample vibrational spectrum.

It is important to characterize the **frequency correlations of the reference pulses**, those that do not interact with the sample. The comparison allows to discriminate the sample induced signals. We introduce here a phenomenological model that describes the randomized pulses and allows to comprehend the measurements we will show in the following chapters. It is of utmost importance to take into account, in the model, the role of the intensity detection to reproduce the experimental results. Since we use detectors with a finite frequency resolution, we consider a frequency gating $G(\omega - \omega)$, extending over a spectral region centred around ω . The spectral extension of the gating is set by the size of the photodiode arrays pixels. We write the intensity measured by the pixel centred at ω by considering the superposition of the fields within this region, as:

$$I(\omega) = \Re \int d\omega' d\omega'' G(\omega' - \omega) G(\omega'' - \omega) E^*(\omega') E(\omega'') e^{-i[\varphi(\omega') - \varphi(\omega'')]} \tag{2.50}$$

²The \pm sign has been considered here since the cross-correlation signal is symmetric under the exchange $i \leftrightarrow j$. This symmetry can be also retrieved by evaluating the term $\beta'_i + \gamma''_j$ in Equation 2.47, which yields $\delta(\omega' - \omega'' - \Omega) \delta(\omega_i - \omega_j + \Omega)$.

where $\varphi(\omega')$ and $\varphi(\omega'')$ are the randomized spectral phases, and the integration variables ω' and ω'' span the spectral size of the pixel. We assume that the field amplitudes and the spectral phases vary slowly across the gate. This assumption corresponds to considering the correlation length of the phase fluctuations (Δ_{corr}) larger than the pixel size, so that it is expected that the phase does not change within a single pixel. We consider only the value of the fields at the central frequency ω and consider the phase at the same point, $\Phi(\omega)$, as the difference between the phases of the superposed components. To evaluate it we expand the phase to its first order around each point and get:

$$\varphi(\omega'') - \varphi(\omega') \approx (\omega'' - \omega') \left. \frac{\partial \varphi}{\partial \omega} \right|_{\omega} \equiv \Phi(\omega) \quad (2.51)$$

The intensity measured by the pixel centred at ω is:

$$I(\omega) = \Re [E^*(\omega)E(\omega)e^{i\Phi(\omega)}] = |E(\omega)|^2 \cos[\Phi(\omega)] \quad (2.52)$$

whose positivity is guaranteed by the fact that we assume $\Phi(\omega)$ to be small. Equation 2.52 clearly highlights that phase fluctuations are mapped into amplitude ones, as a consequence of the detection procedure.

We can now write the average of a product of intensities measured at two distinct pixels centred at ω_1 and ω_2 as:

$$\langle I(\omega_1) I(\omega_2) \rangle = I(\omega_1) I(\omega_2) \langle \cos[\Phi(\omega_1)] \cos[\Phi(\omega_2)] \rangle \quad (2.53)$$

We recall that we have assumed a Gaussian correlation between distinct spectral phases (Equation 2.41), which results in a non-zero correlation also between their derivatives $\Phi(\omega_1)$ and $\Phi(\omega_2)$. We thus expect the cross average to have a different behaviour when ω_1 and ω_2 lie within the correlation length and when they don't:

$$\langle I(\omega_1) I(\omega_2) \rangle - \langle I(\omega_1) \rangle \langle I(\omega_2) \rangle = \begin{cases} (1 - \kappa_{12}^2) & \text{if } |\omega_1 - \omega_2| \lesssim \Delta_{corr} \\ 0 & \text{if } |\omega_1 - \omega_2| \gg \Delta_{corr} \end{cases} \quad (2.54)$$

In the last equation, to be consistent with the treatment of the sample beam, we have calculated the average of a product after subtracting to each intensity its average, and defined $\kappa_{12}^2 \equiv \langle \cos[\Phi(\omega_1)] \cos[\Phi(\omega_2)] \rangle - \langle \cos[\Phi(\omega_1)] \rangle \langle \cos[\Phi(\omega_2)] \rangle$. We recall that points in the spectral phase whose distance is greater than the correlation length, are statistically independent, thus $\langle \cos[\Phi(\omega_1)] \cos[\Phi(\omega_2)] \rangle$

can be factorized as $\langle \cos [\Phi (\omega_1)] \rangle \langle \cos [\Phi (\omega_2)] \rangle$, which vanishes.

Equation 2.54 is the key to interpret the correlation coefficient from the reference light pulses. Note that, even if we have discussed here only the role of the detectors, the results we obtained are valid for any instruments introducing discretization effects. **The interference effect taking place on the photodiode arrays reveals the randomization applied onto the spectral phase**, which would be concealed measuring the intensity with an infinitely frequency resolving detector or within a non frequency resolved scheme. Each measured reference intensity spectrum, as can be inferred from Equation 2.52, is characterized by noisy spikes, whose amplitude, average width and position is directly determined by the unique random spectral phase introduced. The correlation coefficient calculated on such spectra is, as a consequence, able to reveal the actual statistical relationship between the spectral components. The result of a simulation is shown in panel a) of Figure 2.3, where we employed a set of phase randomized intensity spectra to calculate the coefficient ρ . The map is zero for all of the pairs of components outside the diagonal, whose width is directly proportional to the correlation length.

A different approach was taken to calculate the covariance of two frequency dependent intensities when the spectrum is measured after the sample. Within a fully quantum model we were able to directly obtain an expression for the self-heterodyned scattering signal. The field spectral phase is explicitly accounted for in the formula, therefore the calculation for the average of a product of two points within the spectrum, Equation 2.49, necessarily is affected by the phase distribution, meaning that fields which are farther than Δ_{corr} give a vanishing signal, unless they are coupled by the scattering process. **This coupling is revealed by the presence of sidebands, offset from the diagonal, in the correlation coefficient.** This can be seen in the plot of panel b) of Figure 2.3, where we report ρ calculated on a set of simulated randomized pulses. The particular relationship between pairs of coupled spectral components at the phonon frequency distance holds along the whole spectrum, as a consequence we expect the correlation features to show up as lines (not, e.g. dots).

The spectra transmitted by the sample are processed by the discrete detector

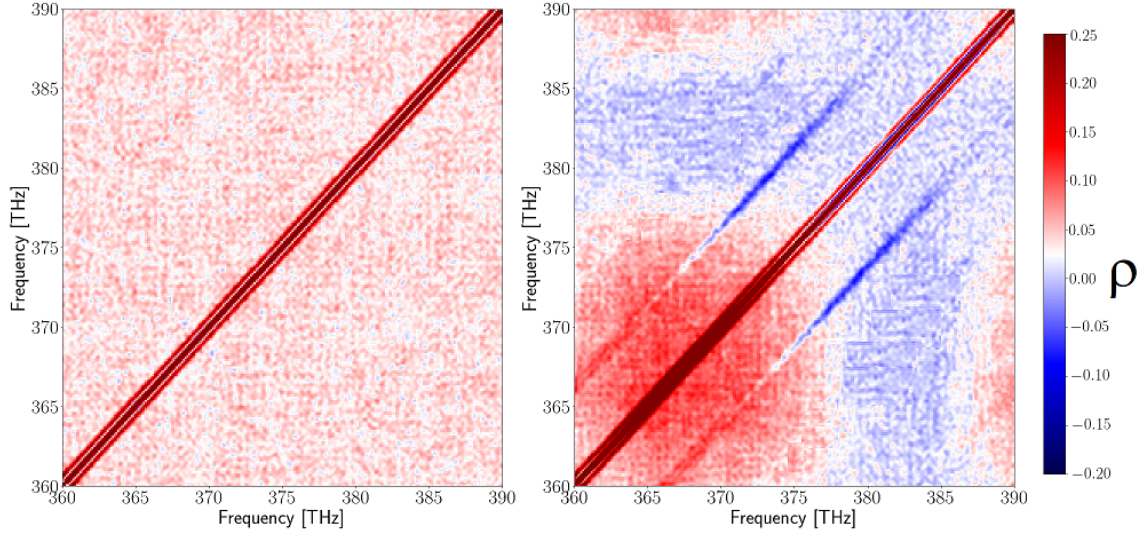


Figure 2.3: Correlation coefficient ρ calculated on a) reference and b) transmitted pulses using Equations 2.45, 2.54 and 2.49. We note the presence of the diagonal in both plots and of offset sidebands in b) (the value of the phonon shift is arbitrary in the calculation for the Figure).

as well, therefore the measurement reveals a noisy intensity profile, as we will show in Chapter 4. This effect allows, similarly to what happens to the reference correlation coefficient, to remove from the map the global pulse fluctuations. Nonetheless, the background of ρ could still be affected by the global statistical properties of the pulses, and retain a large scale structure. In Figure 2.3 we have an example of this effect: the spectral shift introduced by the inelastic scattering process determines "blocks" of positive and negative correlation (the reason for this behaviour is explained in Appendix A). This results in a relatively small offset in the correlation value. At a closer inspection of Figure 2.3, we find that the sign of the correlation signal is in agreement with the sign of the global correlation. This hints to the possible interpretation of the sign of the sidebands as an information on the nature and frequency directionality of the underlying scattering process.

We have seen how the information on vibrational levels of a sample, interacting with noisy light in an inelastic scattering process, is mapped onto characteristic sidebands in the frequency dependent correlation coefficient. In the following we will focus, instead, on the description of the time evolution of the sample properties and of the light quantum state after the interaction,

with the aim, in the near future, to merge the description of a time resolved experiment with that of a noise based acquisition.

2.2 ■ Double pulse interaction

We start this section going back to the intuitive classical picture of the beginning of the Chapter, showing how, properly choosing the boundary conditions, the system of Equation 2.5 can describe both pump and probe in a double pulse experiment. As sketched in Figure 2.4, a first, very intense pump pulse finds the sample at equilibrium and excites coherent vibrations. A weaker pulse, the probe, variably delayed in time, finds the crystal out of equilibrium and further interacts with it.

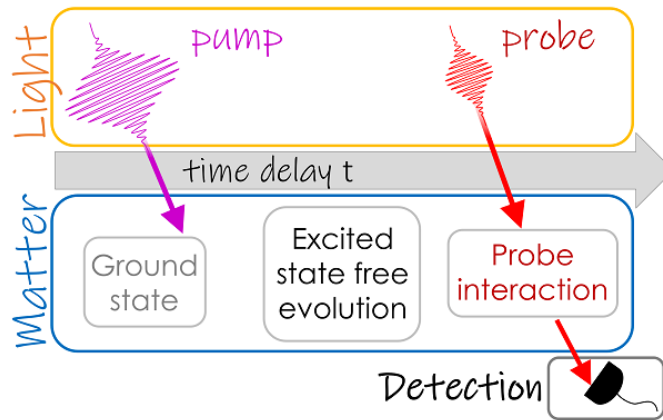


Figure 2.4: Scheme of the time ordering of the interactions of the pump and probe light pulses with the crystal.

The ultrashort light pulses, propagating along the z direction, can be described by the superposition $\mathbf{E}(t') = \sum_{\omega} \mathbf{E}(\omega)e^{-i\omega t'} + c.c.$ denoting the time and space coordinates as $t' = t - \frac{n(\omega)}{c}z$. Introducing a tensor notation (with indices i, j, k) to denote the vector components, we write the induced polarization as

$$P_i = \alpha_{ij}E^j, \quad (2.55)$$

where α_{ij} is the polarizability tensor, which we use to calculate the energy required to establish the polarization in the dipole approximation

$$V = -\mathbf{P} \cdot \mathbf{E} = -\alpha_{ij}E^i E^j \quad (2.56)$$

The polarizability tensor can be expanded up to the first order as a function of the vibrational amplitude Q^k around the equilibrium polarizability α_{ij}^0 (as done in Equation 2.4):

$$\alpha_{ij}(Q^k) = \alpha_{ij}^0 + \left[\left(\frac{\delta\alpha}{\delta Q^k} \right) \Big|_{Q^k=0} \right]_{ijk} Q^k \quad (2.57)$$

As we did in Section 2, we consider two generic components $\omega_{1,2}$ in the bandwidth of the pulse. The electric fields exert a force on the charges that can be derived as

$$\begin{aligned} F_k(t') &= -\frac{dV}{dQ^k} = \left(\frac{\delta\alpha}{\delta Q^k} \right)_{ijk} E^i E^j = \\ &= \left(\frac{\delta\alpha}{\delta Q^k} \right)_{ijk} \left(\sum_{\omega_1} E^i(\omega_1) e^{-i\omega_1 t'} + c.c. \right) \left(\sum_{\omega_2} E^j(\omega_2) e^{-i\omega_2 t'} + c.c. \right) \end{aligned} \quad (2.58)$$

We make two simplifying assumptions: we neglect the damping and only consider one normal vibrational mode with frequency Ω .

We know that the nonlinear coupling in the material determines a mixing of the components within the pulse bandwidth. When the condition $\omega_1 - \omega_2 = \pm\Omega$ is fulfilled, the driving is resonant with the vibration and is most effective. Considering such pairs of frequency and the field real parts we get

$$\begin{aligned} F_k(t') &= \left(\frac{\delta\alpha}{\delta Q^k} \right)_{ijk} \sum_{\omega} \left(E^i(\omega) E^j(\omega - \Omega) e^{-i\Omega t'} + E^i(\omega) E^j(\omega + \Omega) e^{+i\Omega t'} + c.c. \right) = \\ &= \left(\frac{\delta\alpha}{\delta Q^k} \right)_{ijk} \left(\sum_{\omega} E^i(\omega) (E^j(\omega - \Omega) + E^j(\omega + \Omega)) \right) (e^{+i\Omega t'} + e^{-i\Omega t'}) = \\ &= 2 \left(\frac{\delta\alpha}{\delta Q^k} \right)_{ijk} \left(\sum_{\omega} E^i(\omega) (E^j(\omega - \Omega) + E^j(\omega + \Omega)) \right) \cos(\Omega t') = \\ &\equiv f_k \cos(\Omega t') \end{aligned} \quad (2.59)$$

Thus the force is a sinusoidal function of time with frequency Ω and amplitude

$$f_k = 2 \left(\frac{\delta\alpha}{\delta Q^k} \right)_{ijk} \left(\sum_{\omega} E^i(\omega) (E^j(\omega - \Omega) + E^j(\omega + \Omega)) \right) \quad (2.60)$$

The differential equation describing the dynamics of the vibrational amplitude $Q(t')$, approximated by the solution of a harmonic oscillator, forced by the pulse, is thus:

$$\begin{aligned} \frac{d^2 Q(t')}{dt'^2} + \Omega^2 \frac{dQ(t')}{dt'} &= F(t') \\ &= f_k \cos(\Omega t') \end{aligned} \quad (2.61)$$

where in the last line we have used Equation 2.60. A general solution is derived in Appendix B (Equation B.32) considering that the forcing takes place for a

very short time τ , representing the pulse duration.

We calculate the **solution for the interaction with the pump**

$$Q_k(t') = \frac{\tau f_k^{pump}}{2\Omega} \sin(\Omega t') \quad (2.62)$$

being f_k^{pump} Equation 2.60 calculated on the pump field, with the following initial conditions for the vibrational amplitude

$$\left\{ \begin{array}{l} Q_k(t' = 0) = 0 \\ \frac{dQ_k}{dt} \Big|_{t'=0} = \max \end{array} \right. \quad (2.63)$$

As the pump-induced coherent oscillation, Equation 2.62, has a definite phase, for a given pump-probe time delay we expect a specific effect of the interaction on the probe spectrum and the vibrational amplitude. This can be anticipated with an intuitive argument: the energy exchange between the light and the sample depends on the scalar product between the forcing electric field and the vibration momentum. If the scalar product is zero, when the oscillator has maximum amplitude, there is no energy exchange. We will see in the next section that there are other effects taking place during the interaction at maximum amplitude, which are due to the system being out of equilibrium.

To calculate explicitly the dynamical probe intensity, we drop the tensor indices. We start from the Maxwell equations for a neutral system [35]

$$\left\{ \begin{array}{l} \nabla \cdot \mathbf{E} = 0 \\ \nabla \cdot \mathbf{B} = 0 \\ \nabla \times \mathbf{E} = -\frac{\partial \mathbf{B}}{\partial t} \\ \nabla \times \mathbf{B} = \mu_0 \mathbf{J} + \frac{1}{c^2} \frac{\partial \mathbf{E}}{\partial t} \end{array} \right. \quad (2.64)$$

with \mathbf{E} , \mathbf{B} and \mathbf{J} the electric and magnetic fields of the probe pulse and the current in the sample respectively. We apply the rotor to the third equation, insert the fourth and get

$$\begin{aligned} \nabla \times \nabla \times \mathbf{E} &= \nabla(\nabla \cdot \mathbf{E}) - \nabla^2 \mathbf{E} = -\frac{\partial}{\partial t}(\nabla \times \mathbf{B}) = \\ &= -\mu_0 \frac{\partial \mathbf{J}}{\partial t} - \frac{1}{c^2} \frac{\partial^2 \mathbf{E}}{\partial t^2} \end{aligned} \quad (2.65)$$

The current is function of the polarization field \mathbf{P} , thus we use the relation $\mathbf{J} = \frac{\partial \mathbf{P}}{\partial t}$, together with Equations 2.55 and 2.57 to write

$$\begin{aligned}\nabla^2 \mathbf{E} &= \mu_0 \frac{\partial^2 \mathbf{P}}{\partial t^2} + \frac{1}{c^2} \frac{\partial^2 \mathbf{E}}{\partial t^2} = \\ &= \mu_0 \frac{\partial^2 \alpha \mathbf{E}}{\partial t^2} + \frac{1}{c^2} \frac{\partial^2 \mathbf{E}}{\partial t^2} \\ &= \mu_0 \alpha_0 \frac{\partial^2 \mathbf{E}}{\partial t^2} + \frac{1}{c^2} \frac{\partial^2 \mathbf{E}}{\partial t^2} + \mu_0 \left(\frac{\delta \alpha}{\delta Q} \right)_{Q=0} \frac{\partial^2 (Q \mathbf{E})}{\partial t^2}\end{aligned}\quad (2.66)$$

We make use of the relation between polarizability and refractive index

$$\frac{1}{c^2} + \mu_0 \alpha_0 = \frac{1}{c^2} \left(1 + \frac{\alpha_0}{\epsilon_0} \right) \frac{1}{c^2} (1 + \chi) = \frac{n^2}{c^2} \quad (2.67)$$

and get

$$\nabla^2 \mathbf{E}(t') - \frac{n^2}{c^2} \frac{\partial^2 \mathbf{E}(t')}{\partial t'^2} = \mu_0 \left(\frac{\delta \alpha}{\delta Q} \right)_{Q=0} \frac{\partial^2 Q(t' + \Delta t) \mathbf{E}(t')}{\partial t'^2} \quad (2.68)$$

which is a corrected wave equation because of the appearance, on the right hand side, of a nonlinear term. We have written explicitly the dependence on the time variable $t' = t - \frac{n}{c}z$ and added the quantity Δt representing the pump-probe delay.

2.2.1 ■ Time dependent effects on the refractive index

We describe in this section the effects of the coherent distortion on the refractive index of the material. We start from the expansion of the polarizability tensor, Equation 2.57, as a function of the vibrational amplitude. We consider the time dependent vibrational amplitude after the interaction with the pump, Equation 2.62, and by simple substitution we obtain (in scalar notation)

$$\alpha(Q) = \alpha^0 + \left(\frac{\delta \alpha}{\delta Q} \right) \Big|_{Q=0} \frac{\tau f^{pump}}{2\Omega} \sin(\Omega t') \quad (2.69)$$

We observe that the polarizability is modulated at the phonon frequency. Knowing the relationship between equilibrium polarizability α_0 and dielectric susceptibility χ

$$\alpha_0 = \epsilon_0 \chi \quad (2.70)$$

and that χ determines the index of refraction [35]

$$n = \sqrt{1 + \chi} \quad (2.71)$$

we expect the pump to affect the optical response of the material to the propagation of a field. To display this effect we explicit the right hand side of Equation 2.68 to collect the second order time derivatives of the electric field and

recognize the coefficient

$$\tilde{n}^2(\Delta t) = n^2 + c^2 \mu_0 \left(\frac{\delta \alpha}{\delta Q} \right)_{Q=0} Q(\Delta t) \quad (2.72)$$

representing a time- (and implicitly frequency-) dependent refractive index, whose intensity varies with the phonon frequency according to the amplitude Q . We assumed a reference frame in which the pump excitation starts at $t' = 0$.

In case of normal incidence of the probe pulse on the sample we can use the Fresnel equation [35] to write the transmission coefficient $\mathbf{T}(\Delta t, \omega)$ of the excited material, in the frequency domain, as

$$\mathbf{T}(\Delta t, \omega) = \frac{2}{1 + \tilde{n}(\Delta t)} \quad (2.73)$$

Given that $\tilde{n} - n \ll n$ we expand the transmittivity around the equilibrium refractive index

$$\mathbf{T}(\Delta t, \omega) = \frac{2}{1 + n} \left[1 - \frac{c^2 \mu_0}{2n(1 + n)} \left(\frac{\delta \alpha}{\delta Q} \right)_{Q=0} Q(\Delta t) \right] \quad (2.74)$$

which is modulated in phase with the vibrational amplitude. Using this coefficient and Equation 2.60, we write the transmitted intensity as

$$I(\omega, \Delta t) = I(\omega, 0) - \gamma |E^I(\omega)|^2 \left(\sum_{\omega} E^{PU}(\omega) (E^{PU}(\omega - \Omega) + E^{PU}(\omega + \Omega)) \right) \sin(\Omega \Delta t) \quad (2.75)$$

where we have collected all the constants in a factor γ and indicated with E^{PU} the pump field and E^I the incident probe field. We notice that the transmitted intensity depends linearly on the intensity of both pump and probe.

It is convenient to define a relative differential transmitted intensity

$$\frac{I(\omega, \Delta t) - I(\omega)_{\Delta t < 0}}{I(\omega)_{\Delta t < 0}} = \frac{\Delta I}{I} \quad (2.76)$$

which allows to visualize directly the induced changes. In Figure 2.5 we plot $\Delta I/I$, calculated using Equation 2.75, as a function of ω and Δt , showing the periodic increase and decrease of the transmittivity.

As anticipated at the end of the last paragraph, this transmittivity modulation is particularly apparent in the nodes of the spectral shift of the probe, which happen when the vibrational momentum is zero, in other words at all the delays between the red-shifts and blue-shift of the probe spectrum. The inelastic scattering of the probe will be studied in the next paragraph.

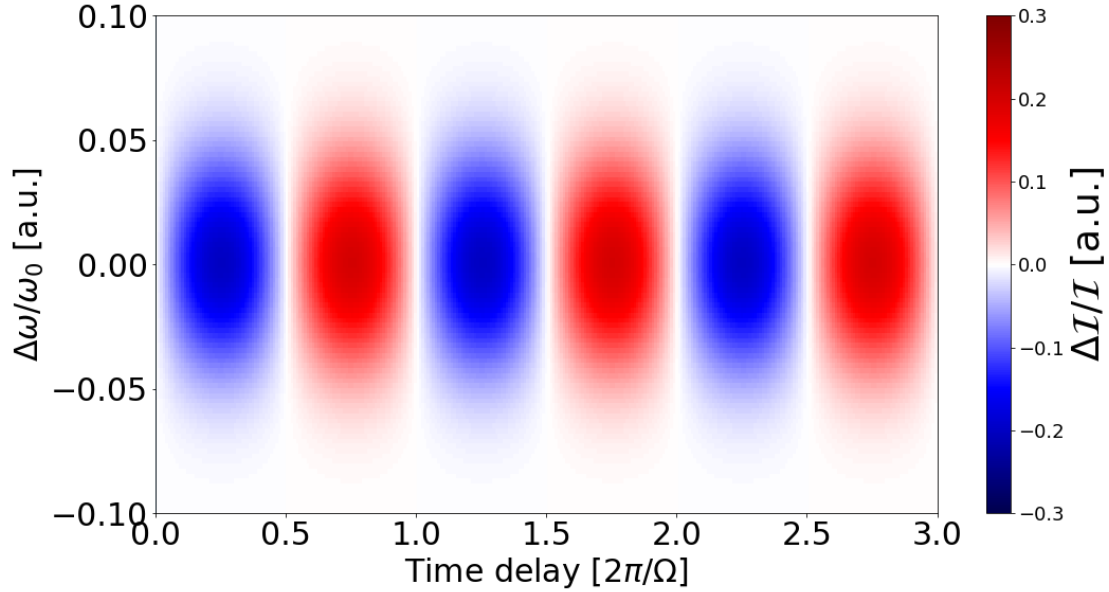


Figure 2.5: Relative differential transmitted intensity $\Delta I/I$ calculated using Equation 2.75, showing the effect of a nonlinear refractive index modulation, induced by the coherent pumping of a vibrational mode, on the spectrum of the transmitted probe pulses.

2.2.2 ■ Time dependent inelastic scattering of probe pulses

The starting point is Equation 2.68, which will be explicitly solved. Considering the variable $t' = t - \frac{n}{c}z$, the following relations for a generic function $f(t')$ hold

$$\begin{cases} \frac{\partial f(t')}{\partial t} = \frac{\partial f(t')}{\partial t'} \\ \frac{\partial^2 f(t')}{\partial z^2} = -\frac{n^2}{c^2} \frac{\partial^2 f(t')}{\partial t'^2} = -\frac{n}{c} \frac{\partial^2 f(t')}{\partial z \partial t'} \end{cases} \quad (2.77)$$

and allow to rewrite Equation 2.68 as

$$-2\frac{n}{c} \frac{\partial^2 \mathbf{E}(t')}{\partial z \partial t'} = \mu_0 \left(\frac{\delta \alpha}{\delta Q} \right)_{Q=0} \frac{\partial^2 Q(t' + \Delta t) \mathbf{E}(t')}{\partial t'^2} \quad (2.78)$$

We integrate such equation in space considering a sample with thickness z , with initial condition $\mathbf{E}(t', z = 0) = \mathbf{E}^I(t')$

$$-2\frac{n}{c} \left(\frac{\partial \mathbf{E}(t', z)}{\partial t'} - \frac{\partial \mathbf{E}^I(t')}{\partial t'} \right) = \mu_0 \left(\frac{\delta \alpha}{\delta Q} \right)_{Q=0} \frac{\partial^2 Q(t' + \Delta t) \mathbf{E}(t')}{\partial t'^2} \quad (2.79)$$

and then integrate over t' , which depends also on the space coordinate and accounts for the propagation time of the field through the sample. We set the initial condition $\mathbf{E}(t' = 0) = \mathbf{E}^I(t')$ and use, on the right hand side, the fact that the variation of the polarizability is small, therefore choosing to set it to its initial value

$$\mathbf{E}(t') - \mathbf{E}^I(t') = -\frac{\mu_0 c z}{2n} \left(\frac{\delta \alpha}{\delta Q} \right)_{Q=0} \frac{\partial^2 Q(t' + \Delta t) \mathbf{E}(t')}{\partial t'^2} \quad (2.80)$$

We look for a solution calculating the right hand side of the equation in the frequency domain, using the Fourier expansion

$$\mathbf{E}(t) = \int d\omega \mathbf{E}(\omega) e^{i\omega t} \quad (2.81)$$

To explicit its time dependence, we rewrite the vibrational amplitude in the form

$$Q(t' + \Delta t) = Q_0 \sin(\Omega(t' + \Delta t)) \quad (2.82)$$

Using Equations 2.81 and 2.82, we rewrite the right hand side of Equation 2.80 as

$$\begin{aligned} \frac{\partial Q(t' + \Delta t) \mathbf{E}^I(t')}{\partial t'} &= \\ &= Q_0 \int d\omega \mathbf{E}^I(\omega) \left(\sin(\Omega(t' + \Delta t)) \frac{\partial e^{i\omega t'}}{\partial t'} + \frac{\partial \sin(\Omega(t' + \Delta t))}{\partial t'} e^{i\omega t'} \right) = \\ &= Q_0 \int d\omega \mathbf{E}^I(\omega) \left(i\omega \sin(\Omega(t' + \Delta t)) + \Omega \cos(\Omega(t' + \Delta t)) e^{i\omega t'} \right) = \\ &= \frac{Q_0}{2} \int d\omega \mathbf{E}^I(\omega) \left((\omega + \Omega) e^{i(\omega + \Omega)t'} e^{i\Omega \Delta t} - (\omega - \Omega) e^{i(\omega - \Omega)t'} e^{-i\Omega \Delta t} \right) \end{aligned} \quad (2.83)$$

We notice the dependence on the phonon frequency Ω , thus we change the integration variable from ω to $\omega \pm \Omega$, getting

$$\frac{\partial Q(t' + \Delta t) \mathbf{E}^I(t')}{\partial t'} = \frac{Q_0}{2} \int d\omega \omega \left(\mathbf{E}^I(\omega - \Omega) e^{i\Omega \Delta t} - \mathbf{E}^I(\omega + \Omega) e^{-i\Omega \Delta t} \right) e^{i\omega t'} \quad (2.84)$$

Fourier expanding the left hand side of 2.80 we get an explicit formula for the spectrum of the transmitted field:

$$\mathbf{E}(\omega)(\Delta t) = \mathbf{E}^I(\omega) + \frac{cz\mu_0}{4n} \left(\frac{\delta\alpha}{\delta Q} \right)_{Q=0} Q_0 \omega \left(\mathbf{E}^I(\omega + \Omega) e^{-i\Omega \Delta t} - \mathbf{E}^I(\omega - \Omega) e^{i\Omega \Delta t} \right) \quad (2.85)$$

where we notice the dependence of the ω component on the components at $\omega \pm \Omega$, due to the coupling introduced by the inelastic scattering.

Defining the coupling constant $k_\Omega = \frac{cz\mu_0}{2\bar{n}} \left(\frac{\delta\alpha}{\delta Q} \right)_{Q=0} Q_0 \omega$, we finally calculate the transmitted intensity as a function of frequency and pump probe time delay, that reads:

$$I(\omega, \Delta t) = I^I(\omega) + k_\Omega \mathbf{E}^I(\omega) \left[\mathbf{E}^I(\omega + \Omega) - \mathbf{E}^I(\omega - \Omega) \right] \cos(\Omega \Delta t) \quad (2.86)$$

We extract from k_Ω the pump field E^{PU} (redefining the gathered factors as k'_Ω)

and explicit the dependence on all the fields

$$\begin{aligned}
 I(\omega, \Delta t) &= \\
 &= I^I(\omega) + k'_\Omega \left(\sum_{\omega} E^{PU}(\omega) (E^{PU}(\omega - \Omega) + E^{PU}(\omega + \Omega)) \right) \cdot \\
 &\cdot [\mathbf{E}^I(\omega) (\mathbf{E}^I(\omega + \Omega) - \mathbf{E}^I(\omega - \Omega))] \cos(\Omega \Delta t)
 \end{aligned} \tag{2.87}$$

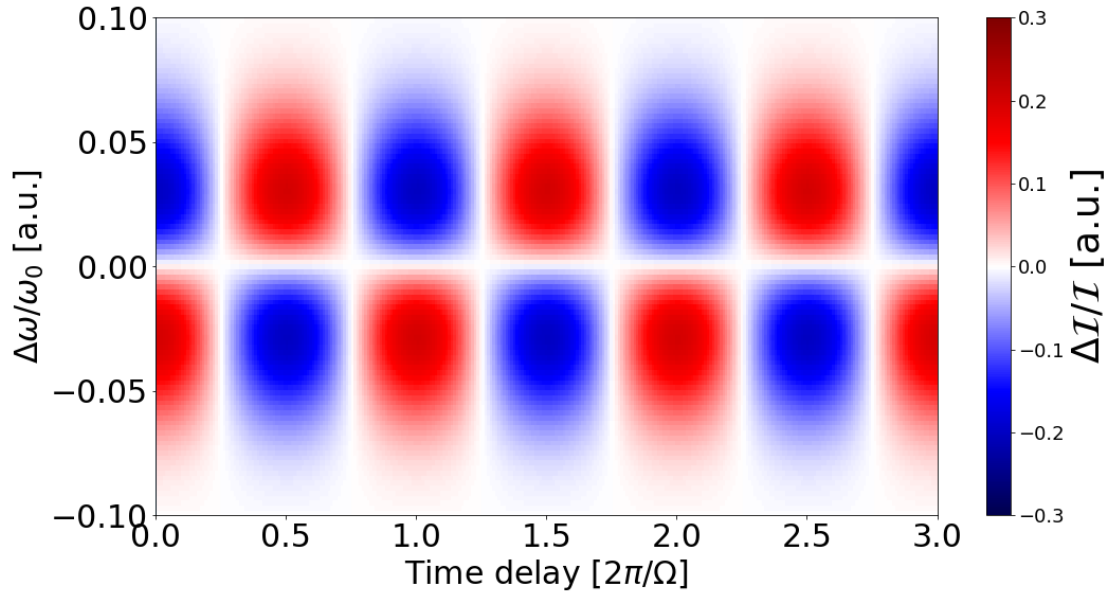


Figure 2.6: Relative differential transmitted intensity $\Delta I/I$ calculated using Equation 2.87, showing the spectrum of the transmitted pulses undergoing inelastic scattering in a medium where a coherent vibration was excited by a pump.

In Figure 2.6 we plot $\Delta I/I$ calculated with appropriate parameters using Equation 2.87 to display the probe inelastic scattering. At all the time delays when the cosine is non vanishing, we observe a shift of the spectrum towards the low or high frequency side. Being these points distant a vibrational period, the single mode signal oscillates at the phonon frequency Ω as a function of Δt , but its absolute phase changes depending on the position of ω in the spectrum. When the cosine is zero, no shift in the spectrum is present, and the effect due to the nonlinear modulation in the refractive index emerges, as it is $\pi/2$ shifted in time with respect to the inelastic scattering induced dynamics (compare Equation 2.75 to Equation 2.87). In other words we can say that

$$\begin{aligned}
 \Delta I(\Delta t)/I &\propto Q(\Delta t) \quad \text{refractive index nonlinearity} \\
 \Delta I(\Delta t)/I &\propto P(\Delta t) \quad \text{inelastic scattering}
 \end{aligned} \tag{2.88}$$

At the foundations of the discussion we just concluded lie considerations on the mechanics of the ions, regarding them as springs, generating during their motion an instantaneous electric field with the electrons which couples to the electric field of the pulses. The predictions of this phenomenological model will be validated by the results of the quantum mechanical reformulation of the problem, presented in the next paragraph, starting from *operators* for both light and matter, whose expected values for the *observables* represent measurable quantities.

We will now set the basis for the **quantum description of the pump probe experiment** by developing a common formalism for light and matter at all the stages of the interaction. In the following the electromagnetic fields of the light pulses and the elastic field of the material will be expressed in terms of *photonic* and *phononic* creation (and annihilation) operators \hat{a}^\dagger (\hat{a}) and \hat{b}^\dagger (\hat{b}), that satisfy the bosonic commutation relations (Equation 2.12) in their quantized form that is, respectively [39, 40]

$$\hat{E}_\lambda(t, z) = i \sum_{\omega} \sqrt{\frac{\omega}{2v\epsilon_0}} \left(\hat{a}_{\omega, \lambda} e^{-i(\omega t - \vec{k} \cdot \vec{r})} - \hat{a}_{\omega, \lambda}^\dagger e^{i(\omega t - \vec{k} \cdot \vec{r})} \right) \quad (2.89)$$

$$\hat{Q}(t, \vec{r}) = \frac{1}{\sqrt{m\Omega v_S}} \left(\hat{b}_{\Omega, \vec{u}} e^{-i(\Omega t - \vec{u} \cdot \vec{r})} + \hat{b}_{\Omega, \vec{u}}^\dagger e^{i(\Omega t - \vec{u} \cdot \vec{r})} \right) \quad (2.90)$$

where we introduced the indices of two orthogonal linear polarizations λ and λ' composing the electric field, v is the quantization volume, v_S is the sample volume, Ω is the phonon frequency and m the ionic effective mass.

We use these equations to redefine the energy required to establish the polarization in the medium when an ultrashort pulse is interacting with it, Equation 2.56. The quantity we get is the **interaction Hamiltonian** of the system

$$\begin{aligned} \hat{H}_{\text{INT}} = \int_{v_S} d\vec{r} \sum_{\lambda, \lambda'} \left[\alpha_{0\lambda\lambda'} + \left(\frac{\delta\alpha}{\delta Q} \right) \Big|_{Q=0} \frac{1}{\sqrt{m\Omega v_S}} \left(\hat{b}_{\Omega, \vec{u}} e^{-i(\Omega t - \vec{u} \cdot \vec{r})} + \text{h.c.} \right) \right] \times \\ \times \sum_{\omega, \omega'} \frac{\sqrt{\omega\omega'}}{2v\epsilon_0} \left(\hat{a}_{\omega, \lambda} e^{-i(\omega t - \vec{k} \cdot \vec{r})} - \text{h.c.} \right) \left(\hat{a}_{\omega', \lambda'} e^{-i(\omega' t - \vec{k}' \cdot \vec{r})} - \text{h.c.} \right) \end{aligned} \quad (2.91)$$

Of the many terms which arise from the products, we focus on the two terms which describe the nonlinear refractive index modulation and the inelastic scattering. The first reads

$$\hat{H}_{\text{REF}} = -\frac{v_S}{2v} \sum_{\lambda, \lambda', j} \omega_j \left(\chi_{\lambda\lambda'}^{(0)} + \chi_{\lambda\lambda'}^{(1)} \hat{q} \right) \left(\hat{a}_{\lambda j}^\dagger \hat{a}_{\lambda' j} + \hat{a}_{\lambda j} \hat{a}_{\lambda' j}^\dagger \right) \quad (2.92)$$

with v the quantization volume. This term describes the redistribution of photons between two polarizations λ and λ' which is mediated by the static susceptibility $\chi_{\lambda\lambda'}^{(0)}$ and the time dependent susceptibility $\chi_{\lambda\lambda'}^{(1)}$ that is ruled by the instantaneous atomic position. We thus split Equation 2.92 in two terms: an equilibrium one

$$H_{REF}^{(0)} = -\frac{v_S}{2v} \sum_{\lambda\lambda',j} \omega_j \chi_{\lambda\lambda'}^{(0)} \left(\hat{a}_{\lambda j}^\dagger \hat{a}_{\lambda' j} + \hat{a}_{\lambda j} \hat{a}_{\lambda' j}^\dagger \right) \quad (2.93)$$

and a dynamical one

$$H_{REF}^{(1)} = -\frac{v_S}{2v} \hat{Q} \sum_{\lambda\lambda',j} \omega_j \chi_{\lambda\lambda'}^{(1)} \left(\hat{a}_{\lambda j}^\dagger \hat{a}_{\lambda' j} + \hat{a}_{\lambda j} \hat{a}_{\lambda' j}^\dagger \right) \quad (2.94)$$

$\chi^{(0)}$ is the equilibrium susceptibility that describes static effects like polarization rotation and birefringence. We consider the case of an isotropic sample with an hermitian susceptibility of the form

$$\chi^{(0)} = \begin{pmatrix} u & |w|e^{i\phi} \\ |w|e^{-i\phi} & u \end{pmatrix} \quad (2.95)$$

where $|w|$ and ϕ quantify respectively the polarization rotation and ellipticity induced in a linearly polarized input beam. The phonon related nonlinear susceptibility $\chi_{\lambda\lambda'}^{(1)}$ is assumed to be real, such that $\chi_{\lambda\lambda'}^{(1)} = \chi_{\lambda'\lambda}^{(1)}$, and small in absolute value, representing a perturbative modification to the equilibrium tensor. We anticipate that in the experimental realization the equilibrium polarization rotation is accounted for by using an analyzer parallel or orthogonal to the output polarization. In the model, we account for this with an additional term in the Hamiltonian.

The second term contributing to the Hamiltonian is

$$\hat{H}_{ILS} = -\frac{\sqrt{v_S}}{2v\sqrt{2m\Omega}} \sum_{\lambda\lambda',j} \omega_j \chi_{\lambda\lambda'}^{(1)} \left[\left(\hat{a}_{\lambda j}^\dagger \hat{a}_{\lambda' j + \frac{\Omega}{\delta}} \right) \hat{b}_\Omega^\dagger + \left(\hat{a}_{\lambda j} \hat{a}_{\lambda' j + \frac{\Omega}{\delta}}^\dagger \right) \hat{b}_\Omega \right] \quad (2.96)$$

Photons with energy ω_j and polarization λ are destroyed by $\hat{a}_{\lambda j}$ and photons of energy $\omega_j \pm \Omega$ and polarization λ' are created by $\hat{a}_{\lambda' j \pm \frac{\Omega}{\delta}}^\dagger$ while a phonon is created by \hat{b}_Ω^\dagger or annihilated by \hat{b}_Ω , respectively. We also notice that while \hat{H}_{REF} acts as a beamsplitter, relocating photons at a fixed frequency between the two polarizations, without implying an effective transfer of energy between the light and the sample, \hat{H}_{ILS} involves the exchange of a quantum of energy between

the elastic field and the light pulse.

The combination of \hat{H}_{REF} and \hat{H}_{ILS} allows to obtain the system dynamics when acting on the appropriate initial state, considering a finite interaction time τ shorter than the phonon oscillation period $1/\Omega$. We consider the evolution induced by the term \hat{H}_{ILS} on the phonon operator \hat{b}_Ω

$$\hat{b}_\Omega(\tau) = \hat{b}_\Omega(0) + i \frac{\tau \sqrt{v_S}}{2v\sqrt{2m\Omega}} \hat{g} \quad (2.97)$$

where $\hat{g} = \sum_{\lambda\lambda',j} \chi_{\lambda\lambda'}^{(1)} \omega_j \hat{a}_{\lambda j}^\dagger \hat{a}_{\lambda'j+\frac{\Omega}{\delta}}$ which in turn allows to calculate the evolved position and momentum with respect to a generic initial state

$$\begin{cases} \langle \hat{Q}(\tau) \rangle = \langle \hat{Q}(0) \rangle \\ \langle \hat{P}(\tau) \rangle = \langle \hat{P}(0) \rangle + \frac{\tau}{2v} \gamma \end{cases} \quad (2.98)$$

defining $\gamma = \langle \hat{g} \rangle = \sum_{\lambda\lambda',j} \chi_{\lambda\lambda'}^{(1)} \omega_j \left| \alpha_{\lambda j} \right| \left| \alpha_{\lambda'j+\frac{\Omega}{\delta}} \right|$.

We can visualize the result of a sudden Raman interaction as a displacement along the momentum axis defining the evolution radius R , as sketched in Figure 2.7. The squared radius R^2 gives the mean value of the phonon number $\hat{N}_\Omega = \hat{b}_\Omega^\dagger \hat{b}_\Omega$ which, to second order in the $\tau \chi^{(1)}$ coupling parameter, reads

$$\langle \hat{N}_\Omega(\tau) \rangle = \langle \hat{N}_\Omega(0) \rangle + \frac{\tau v_S}{2vm\Omega} \gamma \langle \hat{P}(0) \rangle + \frac{\tau^2 v_S}{8v^2 m \Omega} \langle \hat{g}^\dagger \hat{g} \rangle \quad (2.99)$$

We notice that the first order contribution depends on the value of the momentum \hat{P} before the interaction, while the second order term is proportional to the mean value of the operator $\hat{g}^\dagger \hat{g}$, which equals γ^2 for classical light states (coherent states with very large amplitude). The second order term is usually negligible with respect to the first one unless $\langle \hat{P}(0) \rangle = 0$.

We calculate now the **effect of the interaction on the photonic degrees of freedom**. The light pulses are well described in their initial state by a multimode coherent state $|\alpha\rangle$, where α stands for the vector with components $\alpha_{\lambda j}$, given by

$$|\alpha\rangle = \exp\left(\sum_{\lambda,j} \alpha_{\lambda j} a_{\lambda j}^\dagger - \alpha_{\lambda j}^* a_{\lambda j}\right) |0\rangle, \quad a_{\lambda j} |\alpha\rangle = \alpha_{\lambda j} |\alpha\rangle \quad (2.100)$$

where $|0\rangle$ is the vacuum state and ω_j is the photon frequency indexed by j . The bandwidth of the pulse is represented by a set of modes $\omega_j = j\delta + \omega_0$ centred

around the frequency ω_0 and spaced by δ .

The measured intensity is proportional to the expected value $\langle \hat{N}_{\lambda j}(\tau) \rangle := \langle \hat{a}_{\lambda j}^\dagger(\tau) \hat{a}_{\lambda j}(\tau) \rangle$ on coherent states and results in the quantity [39]

$$\langle \hat{N}_{\lambda j}(\tau) \rangle = \langle \hat{N}_{\lambda j}(0) \rangle + \frac{\tau V_S}{2V m \Omega} \sum_{\lambda'} \chi_{\lambda \lambda'}^{(1)} \omega_j |\alpha_{\lambda j}| \left(\left| \alpha_{\lambda' j + \frac{\Omega}{\delta}} \right| - \left| \alpha_{\lambda' j - \frac{\Omega}{\delta}} \right| \right) \left(\langle \hat{P}(0) \rangle + \frac{\tau}{4V} \gamma \right) + \tau^2 \gamma'_j \quad (2.101)$$

The term proportional to $\langle \hat{P}(0) \rangle$ results from first order contributions and is proportional to the difference between the field amplitude at frequencies $\omega_j \pm \Omega$. The terms in γ and γ' arise from second order interactions.

We use these tools to calculate the output spectra. We assume the **pump** finding the sample at thermal equilibrium, when phonon position and momentum have zero average $\langle \hat{Q}(0) \rangle = \langle \hat{P}(0) \rangle = 0$. The transmitted pump intensity is thus given by Equation 2.101, with the appropriate proportionality factors:

$$\begin{aligned} \langle I_{\lambda j}^{PU}(\tau) \rangle_0 &= \langle I_{\lambda j}^{PU}(0) \rangle_0 \\ &+ \frac{\tau^2 v_S}{8v^2 m \Omega} \gamma^{PU} \sum_{\lambda'} \chi_{\lambda \lambda'}^{(1)} \omega_j |\alpha_{\lambda j}^{PU}| \left(\left| \alpha_{\lambda' j + \frac{\Omega}{\delta}}^{PU} \right| - \left| \alpha_{\lambda' j - \frac{\Omega}{\delta}}^{PU} \right| \right) \end{aligned} \quad (2.102)$$

where we have neglected the term proportional to γ' because the phonon population is negligible with respect to the photon number. We indicate with $\langle I_{\lambda j}^{PU}(0) \rangle_0$ the intensity before the interaction. The second term can be interpreted as an effective red-shift of the spectrum. The effect on the phonon, using Equation 2.98, is a shift along the momentum axis with radius

$$R = \frac{\tau}{2v} \gamma^{PU} \quad (2.103)$$

Given that we are neglecting the dissipation, after the pump excitation and before the probe interaction, the sample evolves with the Hamiltonian of a quantum free harmonic oscillator. As a consequence, the initial conditions for the probe interaction at a given time delay Δt are

$$\begin{cases} \Delta t < 0, & \langle \hat{Q}(0) \rangle_t = \langle \hat{P}(0) \rangle_t = 0 \\ \Delta t > 0, & \langle \hat{Q}(0) \rangle_t = \frac{R}{m\Omega} \sin(\Omega t), \quad \langle \hat{P}(0) \rangle_t = R \cos(\Omega t) \end{cases} \quad (2.104)$$

In the following we consider positive time delays $\Delta t > 0$ and estimate the dynamical intensity modulation $\langle \Delta I_{\lambda j}^{PR} \rangle_{\Delta t > 0} = \langle I_{\lambda j}^{PR}(\tau) \rangle_{\Delta t > 0} - \langle I_{\lambda j}^{PR}(\tau) \rangle_{\Delta t < 0}$ with respect to the unperturbed condition ($\Delta t < 0$). We get

$$\langle \Delta I_{\lambda j}^{PR} \rangle_{\Delta t > 0} = \frac{\tau v_S}{2v m \Omega} \sum_{\lambda'} \chi_{\lambda \lambda'}^{(1)} \omega_j |\alpha_{\lambda j}^{PR}| \left(\left| \alpha_{\lambda' j + \frac{\Omega}{\delta}}^{PR} \right| - \left| \alpha_{\lambda' j - \frac{\Omega}{\delta}}^{PR} \right| \right) \langle \hat{P}(0) \rangle_{\Delta t > 0} \quad (2.105)$$

where we have neglected the second order terms considering that $\gamma^{PR} \ll \langle \hat{p}(0) \rangle_{\Delta t}$ due to the relation $|\alpha^{PU}| \gg |\alpha^{PR}|$.

Applying \hat{H}_{REF} up to first order in $\tau \chi^{(1)}$, the dynamical response due to the pump effect on the refractive index is dependent on the phonon position and reads

$$\langle \Delta I_{\lambda j}^{PR} \rangle_{\Delta t > 0} = -\frac{v_S}{2v} \sum_{\lambda' \lambda''} (\mathbf{K}(\tau, \chi^{(0)}, \chi^{(1)}))_{\lambda, \lambda' \lambda''} |\alpha_{\lambda' j}| |\alpha_{\lambda'' j}| \langle \hat{Q}(0) \rangle_{\Delta t > 0} \quad (2.106)$$

where all the terms which account for the equilibrium refractive properties are collected in the \mathbf{K} tensor.

It is insightful to visualize the pump-probe experiment at a few selected time delays from the point of view of the $\langle \hat{Q} \rangle, \langle \hat{P} \rangle$ phonon phase space and of the relative differential probe intensity $\Delta I/I$, as sketched in Figure 2.7. At equilibrium, the phonon is in a thermal state (blurred circle in the origin of the plane). The pump leaves energy into the system, and displaces the phonon state along the momentum axis. The probe further interacts with the phonon, losing a small amount of energy to it, the pulse spectrum being red shifted. The phonon evolves, reaching its maximum amplitude, where the probe experiences minimum transmittivity. When the phonon has maximum negative momentum, the probe extracts energy from the sample. The phonon is therefore pushed towards a smaller trajectory, and the probe spectrum is blue shifted. Finally, the phonon amplitude reaches a minimum, and the probe transmittivity is maximum. From here the cycle will repeat.

We recognize that the results of the quantum model, Equations 2.106 and 2.105 agree with their classical counterparts, Equations 2.75 and 2.87, respectively. **The microscopic model therefore validates the classical one, and constitutes the basis for a future investigation of the role of the stochasticity in a pump-probe experiment where the probe spectra are randomized.** In fact a

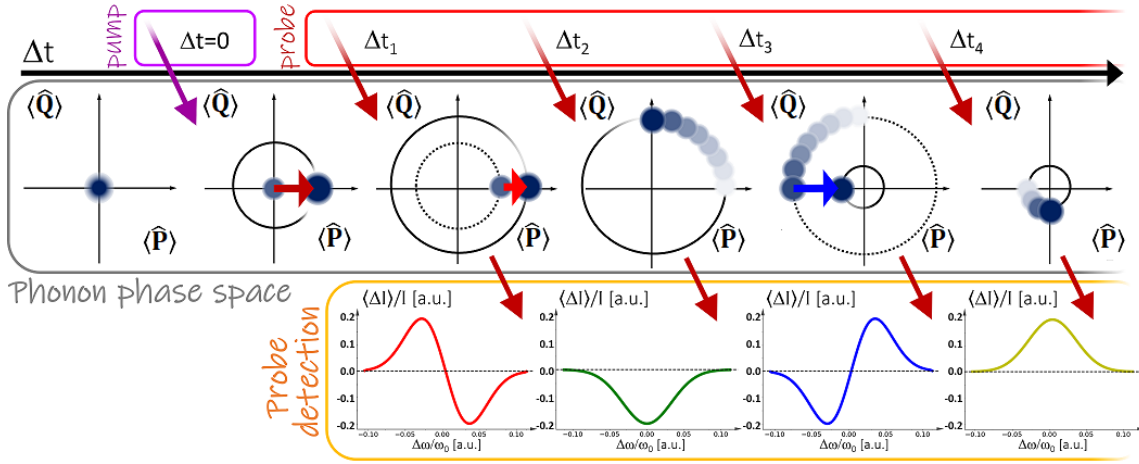


Figure 2.7: Impulsive Stimulated Raman Scattering experiment in the phonon phase space, showing the resulting probe intensity spectrum $\Delta I / I$.

quantum model taking into account the randomized spectral phase will be developed and used to clarify the role of the coherent phonon state in determining the shape and sign of the signal obtained in the preliminary measurements of Section 5.2.

2.2.3 ■ Case study: α -quartz

Applying the quantum formalism, we calculate the probe observables taking into account the material response through a specific susceptibility tensor. Since we are interested in the first order corrections to the transmittivity of the probe pulse, the contributions of different phonon modes add independently to a total susceptibility $\chi = \sum_p \chi_p$, where p denotes the p^{th} phonon mode. The symmetry of χ_p determines the photon polarizations involved in the exchange during the interaction; in other words the contributions of phonons with different symmetry can be selected by a proper combination of the pump and probe polarizations [41].

We focus on the material probed in the measurements of the present Thesis, α -quartz (the prefix refers to the low temperature phase of this material, opposed to the β phase found at temperatures higher than 848 K), that has a trigonal structure with D_3 symmetry and 9 atoms per unit cell. Its 27 degrees of freedom give rise to 2 acoustic modes with $A_2 + E$ symmetry and 16 optical modes with symmetry $4A_1 + 4A_2 + 8E$. Of these, 4 A_1 are infrared-active, 4 A_2

are Raman active, and 8 are doubly degenerate E modes.

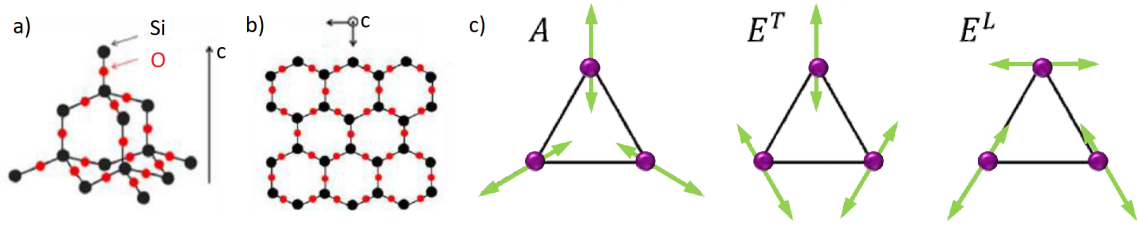


Figure 2.8: a) Atomic arrangement of crystalline quartz unit cell and b) projection on the plane perpendicular to the c -axis. c) Vibrational motion with symmetry A , E_L and E_T (green lines) around the ionic equilibrium positions (purple dots) in a triangular lattice. Adapted from [42].

The unit cell of quartz is sketched in Figure 2.8, together with its projection on the microscopic ab plane, along which the sample is cut. Therefore the sample is excited and probed with fields propagating along its microscopic c -axis, lying in the ab plane. They can only access a few of α -quartz vibrational modes, those of a system with C_3 rotational symmetry. They are compatible with the vibrations allowed for a triatomic molecule with 3 atoms of equal masses placed at the corners of an equilateral triangle, one A mode and two doubly degenerate E modes (separated in longitudinal and transverse, indicated in the following by the subscripts L and T), as sketched in panel c) of Figure 2.8. These modes have matrix representation [42, 43]

$$A_{ij} = \begin{pmatrix} a & 0 \\ 0 & a \end{pmatrix} \quad E_{ij}^L = \begin{pmatrix} c_L & 0 \\ 0 & -c_L \end{pmatrix} \quad E_{ij}^T = \begin{pmatrix} 0 & -c_T \\ -c_T & 0 \end{pmatrix} \quad (2.107)$$

and constitute the susceptibility tensor as

$$\begin{aligned} \chi_{ijkl}^{(3)} &= A_{ij}A_{kl} + E_{Lij}E_{Lkl} + E_{Tij}E_{Tkl} = \\ &= \begin{pmatrix} \begin{pmatrix} a^2 + c^2 & 0 \\ 0 & a^2 - c^2 \end{pmatrix} & \begin{pmatrix} 0 & c^2 \\ c^2 & 0 \end{pmatrix} \\ \begin{pmatrix} 0 & c^2 \\ c^2 & 0 \end{pmatrix} & \begin{pmatrix} a^2 - c^2 & 0 \\ 0 & a^2 + c^2 \end{pmatrix} \end{pmatrix} \end{aligned} \quad (2.108)$$

as $c_T = c_L$ (due to the degeneracy).

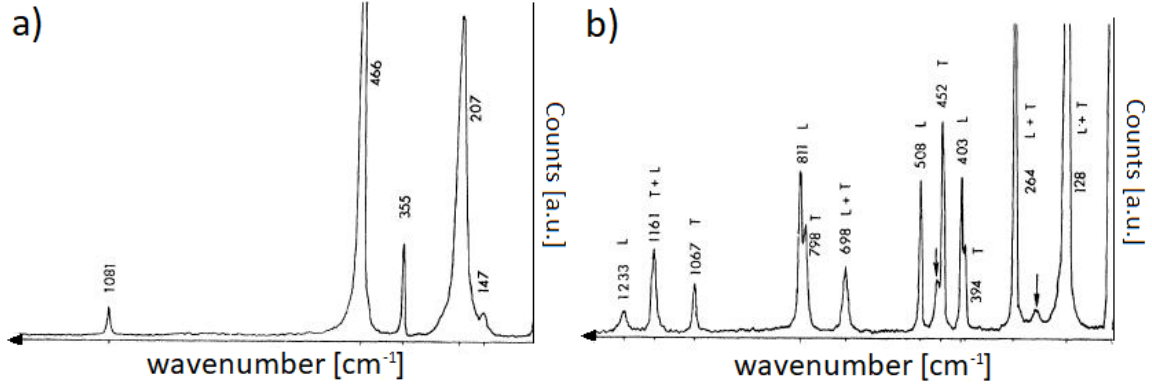


Figure 2.9: Complete vibrational spectrum of α -quartz. Phonons with a) A and b) E symmetry. The arrows indicate A modes that could not be completely extinguished. Adapted from [43].

In Figure 2.9 we plot the full vibrational (Raman) spectrum of α -quartz, as retrieved by measuring the spontaneously inelastically scattered light. **The central frequencies of the α -quartz phonons lying within the bandwidth of our pulses are 3.8, 6.2, 10.7, 14 THz.**

In order to make quantitative predictions, we make some assumptions on the spectral shape of the pulses. Both pump and probe are chosen to be linearly polarized with a Gaussian spectrum whose maximum is $\alpha_0 > 0$ and width σ

$$\alpha_j = \alpha_0 e^{-\frac{1}{2} \left(\frac{j\delta}{\sigma} \right)^2} \quad (2.109)$$

We consider a reference frame in which the z axis is parallel to the microscopic c axis of the sample, while the x and y axes lie on the orthogonal plane. The probe electric field is initially linearly polarized along the x axis and the pump electric field lies in the same plane with an angle θ with respect to the probe (and the x axis). We explicit this dependence on θ by redefining the pump amplitude as

$$\alpha_{xj}^{PU} = \alpha_j^{PU} \cos(\theta), \quad \alpha_{yj}^{PU} = \alpha_j^{PU} \sin(\theta) \quad (2.110)$$

The transmittivity of the probe depends on the radial parameter R defined in Equation 2.103. We calculate it explicitly for the each of the phonons and get

$$\begin{aligned} R_A &= a \eta_{\Omega_A}^{PU} \\ R_{EL} &= c_L \cos(2\theta) \eta_{\Omega_E}^{PU} \\ R_{ET} &= -c_T \sin(2\theta) \eta_{\Omega_E}^{PU} \end{aligned} \quad (2.111)$$

where the parameter η_{Ω}^{PU} is defined as

$$\eta_{\Omega}^{PU} = \frac{\tau}{2v} \sum_j \omega_j \left| \alpha_j^{PU} \right| \left| \alpha_{j+\frac{\Omega}{\delta}}^{PU} \right| \quad (2.112)$$

The expression of the dynamical intensity modulation is simplified considering a small equilibrium rotation, in other words considering only the first order term in $|w|$ (see Equation 2.95). In this case, when the analyzer selects the transmitted intensity along the x axis, this is dominated by the inelastic scattering (which is of order zero in $|w|$):

$$\begin{aligned} \left\langle \Delta I_{xj}^{PR}(\tau) \right\rangle_t &= \frac{\tau v_S}{2v} \omega_j \left| \alpha_j^{PR} \right| \\ &\left[a^2 \left(\left| \alpha_{j+\frac{\Omega_A}{\delta}}^{PR} \right| - \left| \alpha_{j-\frac{\Omega_A}{\delta}}^{PR} \right| \right) \frac{\eta_{\Omega_A}^{PU}}{m_A \Omega_A} \cos(\Omega_A t) \right. \\ &\left. + c_L^2 \cos(2\theta) \left(\left| \alpha_{j+\frac{\Omega_E}{\delta}}^{PR} \right| - \left| \alpha_{j-\frac{\Omega_E}{\delta}}^{PR} \right| \right) \frac{\eta_{\Omega_E}^{PU}}{m_E \Omega_E} \cos(\Omega_E t) \right] \end{aligned} \quad (2.113)$$

evolving at frequencies Ω_A and Ω_E , in phase with the phonon momenta. When selecting the y parallel polarization, instead, the dominating contributions are proportional to $|w|$

$$\begin{aligned} \left\langle \Delta I_{yj}^{PR}(\tau) \right\rangle_t &= \frac{\tau v_S}{2v} \frac{c_T^2 \eta_{\Omega_E}^{PU}}{m_E \Omega_E} \tau |w| \sin(2\theta) (1 - \cos \phi) \left| \alpha_j^{PR} \right| \\ &\times \left[2 \left| \alpha_j^{PR} \right| + \left(\left| \alpha_{j+\frac{\Omega_E}{\delta}}^{PR} \right| + \left| \alpha_{j-\frac{\Omega_E}{\delta}}^{PR} \right| \right) \right] \sin(\Omega_E t) \end{aligned} \quad (2.114)$$

this equation is evolving at Ω_E , in phase with the phonon amplitude. Its first term is due to $\hat{H}_{REF}^{(1)}$ (Equation 2.94), while the second is due to the combined action of $\hat{H}_{REF}^{(0)}$ (Equation 2.93) and \hat{H}_{ILS} (Equation 2.96).

Both the above Equations depend on 2θ . To sample the angle dependent response we calculate Equations 2.113 and 2.114 at $\theta = [0, \pi/8, \pi/4, 3\pi/8, \pi/2]$. The expected signal when the analyzer selects the polarization parallel to the probe reads

$$\begin{aligned} \left\langle \Delta I_{xj}^{PR} \left(\tau, \theta = 0, \frac{\pi}{2} \right) \right\rangle_t &\propto \left[K a^2 \Delta \alpha_{j, \Omega_A}^{PR} \cos(\Omega_A t) \pm c^2 \Delta \alpha_{j, \Omega_E}^{PR} \cos(\Omega_E t) \right] \\ \left\langle \Delta I_{xj}^{PR} \left(\tau, \theta = \frac{\pi}{8}, \frac{3\pi}{8} \right) \right\rangle_t &\propto \left[K a^2 \Delta \alpha_{j, \Omega_A}^{PR} \cos(\Omega_A t) \pm \frac{\sqrt{2}}{2} c^2 \Delta \alpha_{j, \Omega_E}^{PR} \cos(\Omega_E t) \right] \\ \left\langle \Delta I_{xj}^{PR} \left(\tau, \theta = \frac{\pi}{4} \right) \right\rangle_t &\propto \left[a^2 \Delta \alpha_{j, \Omega_A}^{PR} \cos(\Omega_A t) \right] \end{aligned} \quad (2.115)$$

where we gather the electric field amplitudes giving rise to the spectral weight shift and define

$$\Delta \alpha_{j, \Omega_A}^{PR} = \left| \alpha_j^{PR} \right| \left(\left| \alpha_{j+\frac{\Omega_A}{\delta}}^{PR} \right| - \left| \alpha_{j-\frac{\Omega_A}{\delta}}^{PR} \right| \right) \Delta \alpha_{j, \Omega_E}^{PR} = \left| \alpha_j^{PR} \right| \left(\left| \alpha_{j+\frac{\Omega_E}{\delta}}^{PR} \right| - \left| \alpha_{j-\frac{\Omega_E}{\delta}}^{PR} \right| \right) \quad (2.116)$$

When the analyzer is orthogonal to the probe, the signal is

$$\begin{aligned} \left\langle \Delta I_{yj}^{PR} \left(\tau, \theta = 0, \frac{\pi}{2} \right) \right\rangle_t &= 0 \\ \left\langle \Delta I_{yj}^{PR} \left(\tau, \theta = \frac{\pi}{8}, \frac{3\pi}{8} \right) \right\rangle_t &\propto \frac{\sqrt{2}}{2} c^2 \Sigma \alpha_{j, \Omega_E}^{PR} \sin(\Omega_E t) \\ \left\langle \Delta I_{yj}^{PR} \left(\tau, \theta = \frac{\pi}{4} \right) \right\rangle_t &\propto c^2 \Sigma \alpha_{j, \Omega_E}^{PR} \sin(\Omega_E t) \end{aligned} \quad (2.117)$$

with the terms proportional to the field amplitudes gathered in the factor

$$\Sigma \alpha_{j, \Omega_E}^{PR} = |\alpha_j^{PR}| \left(2 |\alpha_j^{PR}| + \left| \alpha_{j + \frac{\Omega_E}{\delta}}^{PR} \right| + \left| \alpha_{j - \frac{\Omega_E}{\delta}}^{PR} \right| \right) \quad (2.118)$$

It can be observed that exploiting the polarization geometries allows to disentangle the symmetry dependent response of α -quartz. One could in principle select the A or E phonons if the appropriate optical elements are used. We note that the E phonons can be selected thanks to the nonlinear refractive index modulation, which affects the probe transmittivity in the orthogonal polarization to that of the probe.

In this Chapter, we used the language of quantum optics and the formalism of the Liouville space to describe a third order light matter interaction. With the former, we defined a quantum state for the elastic field, interacting with a coherent light state for the pump and one for the probe, and conveniently depicted the evolution of the vibrational state in a phase space. The Liouville formalism, on the other hand, provided powerful tools to describe the interaction between a single light pulse and a two-level system, where the output beam is self-heterodyned. Developing these models allowed to formulate predictions for the outcome of experiments based on a single randomized pulse or a pump and a time delayed randomized probe. These two apparently distant frameworks describe the sample and its vibrational levels under close assumptions. A formal and conceptual connection must be found between these two worlds, in order to provide the Femtosecond Covariance Spectroscopy technique with the necessary analytical tools to describe a dynamical noise-based investigation.

3 ■ Experimental realization

In this chapter we present the experimental arrangements chosen and implemented to perform the measurements. To perform a femtosecond covariance measurement, the setup must allow the manipulation of ultrashort laser pulses. We need to split the beam into pump and probe, control their time overlap on the sample, randomize the probe, and finally route the beams of interest to the detectors. As will be explained with more details in the following, the pulses are produced with a fixed time distance (usually expressed as a frequency, the *repetition rate*) much larger (being 200 μs) than the characteristic scales of the dynamics (from tens of fs to tens of ps), and consequently of the pump probe time delays (typically submultiples of 50 fs) sampling such dynamics. In the following we will sometimes refer to the pulse *train* as light beam, a term representing the direction of propagation of the light fields.

The rationale behind the setup construction and usage is outlined in Section 3.1, while in the rest of the chapter we describe the main elements: the laser source, the pulse shaper, the detectors. We dedicate Sections 3.2 and 3.3 to a brief description of two nonlinear optics techniques, Optical Parametric Amplification (OPA) and Frequency Resolved Optical Gating (FROG), that were exploited to convert the pump frequency content and to measure the pulses time duration, respectively.

3.1 ■ Experimental geometries

In this section we present the logic of the different kinds of covariance measurement. The complete setup is sketched in Figure 3.1. When describing the different experiments, we will refer from time to time to different portions of

the such setup.

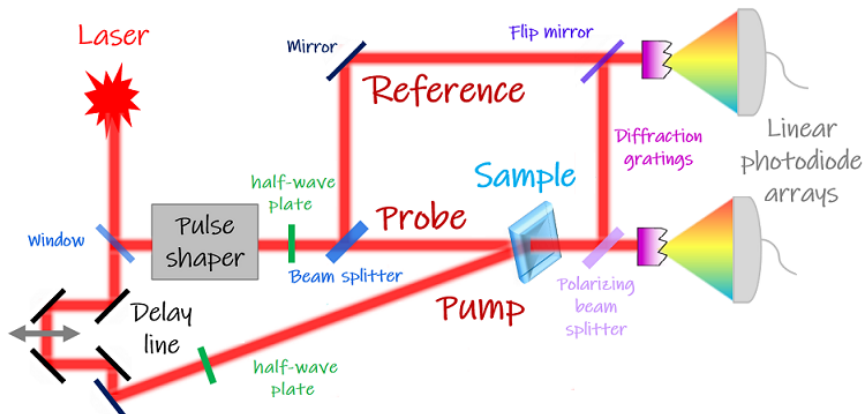


Figure 3.1: Setup implemented to perform single and double pulse experiments. The laser pulses are split in a pump and a probe beam. The first is routed through a delay stage and the second through a pulse shaper. Two beams are then measured: a reference (collected before the sample) and the probe, or two orthogonal probe polarizations. To be detected by the linear photodiode arrays, the pulses are dispersed by a diffraction grating and focused by plano convex lenses. The measured intensity values are sent to a computer for the analysis.

We start with the **transmission measurements**, whose theoretical interpretation is drawn in Section 2.1. To perform these experiments we lead the laser beam through the pulse shaper, that randomizes each pulse. Then the beam is split in two: a reference beam and a probe beam, the latter transmitted by the sample. Each beam is sent to one of a pair of twin detectors, consisting in a diffraction grating to disperse the spectral content, a plano convex lens to focus it, and a linear detector array to record the intensity shot by shot.

To perform **pump probe measurements**, we make use of a pump to excite the sample, and describe the dynamics from a theoretical point of view in Section 2.2. The pump is a portion of the laser beam which is collected before the pulses are sent through the pulse shaper, using a *window* that transmits the 96% of the radiation (pump) and reflects the 4% (sent to the pulse shaper). In order to synchronize each pump and probe pulse pair on the sample, we compare the optical paths of the radiation from the point where the beams are split to the sample, and modify the path length until their values match. We take into account the index of refraction of the transmissive elements in the paths, as it

is usually greater than one, thus effectively elongating the optical path. After optimizing the spatial overlap on the sample using a CCD camera or a pinhole, we find the time overlap by means of sum frequency generation in a β -barium borate (BBO) nonlinear optical crystal (more details about the crystal and its nonlinear response are reported in Sections 3.2 and 3.3). The pump must be routed through a software controlled electronic delay stage, which shortens its optical path to anticipate its arrival time, at the sample position, with respect to the probe. The latter travels through the remaining part of the setup, while the pump is blocked after the sample. A possible variation of this experiment is realized by using a polarizing beamsplitter to split the transmitted probe in two beams with orthogonal polarization, each measured by a detector. If this is the case, the reference beam is blocked and the beam to be measured is routed to the detector using, for example, a *flip mirror*.

3.1.1 ■ Laser

The laser system (manufactured by Coherent [44]) is composed by the elements sketched in Figure 3.2. We cannot describe properly such a system in the Thesis, thus we refer the reader to specialized publications [45, 46]. The system is based on a resonant cavity, allowing a finite number of longitudinal modes, and relies on *mode-locking*, determining a fixed phase relation between the spectral components. Therefore the output pulses are highly spectrally coherent.

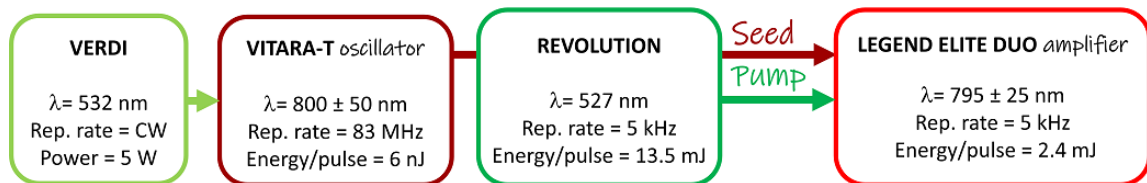


Figure 3.2: Scheme of the generation of the ultrashort pulses used in the experiment for both the single and the double pulse experiment.

The Vitara-T oscillator is a mode-locked laser able to produce ultrashort pulses with central wavelength 800 nm, carrying 6 nJ of energy, and ~ 83 MHz of repetition rate (as mentioned earlier, the inverse time between subsequent pulses, related to the laser cavity length). This regime is reached in the *Kerr Lens medium*, a Ti:Sapphire crystal, when it is pumped by the continuous wave (CW) laser Verdi. The oscillator output constitutes the *seed* beam for the Legend system to amplify using the *pump* produced by the Revolution system. The latter

is based on *Q-switching* to obtain mode-locking, and is an intracavity doubled Nd:YLF laser producing very high energy (16 mJ) pulses. The repetition rate of the Revolution laser is lower than the Vitara-T one, determining the output repetition rate. The Legend Elite Duo *amplifier* employs two thermoelectrically cooled Ti:Sapphire based cavities, a multiple pass and a single pass cavity. It relies on the chirped pulse amplification (CPA) scheme, based on the energy injection into the stretched pulse, which is then compressed [47]. The output of the laser system is a train of pulses with 5 kHz repetition rate, central wavelength 795 nm and duration of about 35 fs (their minimum duration given the bandwidth). Their energy per pulse is about 2.4 mJ, of which a small percentage ($< 10\%$) is effectively employed in our experiments.

3.1.2 ■ Pulse shaper

As the name suggests, a pulse shaper is a tool which enables the manipulation of the intensity figure of ultrashort pulses. As typical durations are few to hundreds of femtosecond, their time dependent electric field it is still not easily accessed. Therefore techniques have been proposed and implemented to manipulate the pulses in the frequency domain, exploiting the relationship between the time and spectral complex planes.

A number of approaches for ultrafast pulse shaping have been advanced [48]. We have adopted a method in which waveform synthesis is achieved by using a device that acts on the angularly dispersed optical frequency spectrum.

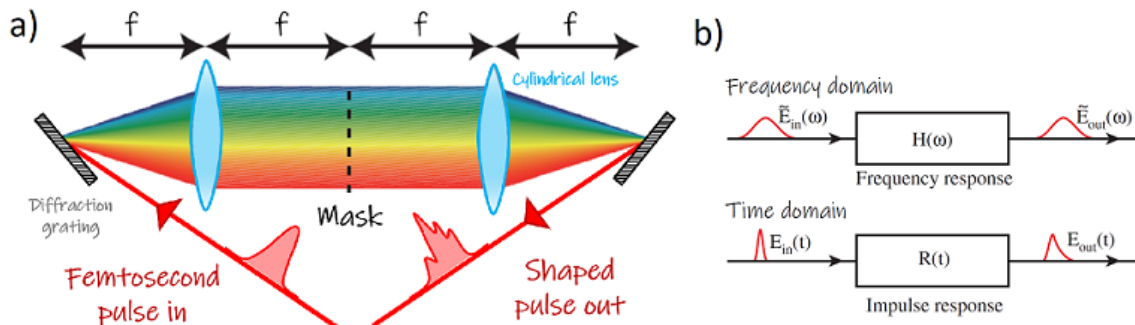


Figure 3.3: a) Pulse shaping using a spatial mask in a $4f$ line configuration. b) Linear filtering in frequency and time domain.

A basic apparatus consists of a pair of diffraction gratings and lenses, arranged in a configuration known as **4f line** (as each optical element in the setup is at distance f from the next, f being the focal length of the cylindrical lenses) or *zero dispersion pulse compressor*. As shown in Figure 3.3, the first diffraction grating angularly disperses the individual frequency components contained within the incident pulse, which are then focused to small diffraction limited spots at the back focal plane of the first lens. Therefore on this plane the frequency components are spatially separated along one dimension (x). If nothing is placed in the Fourier plane, the device is dispersion free, as a second lens and grating recombine all the frequencies into a single collimated beam. Instead if a spatially patterned amplitude or phase mask is placed in the Fourier plane, manipulation of the frequency components can be achieved. The spatial mask $M(x)$, behaves effectively as a complex frequency mask $H(\omega)$, completely describing the effect of the pulse shaper. We look for an explicit expression for the complex mask, starting from the expression of the field immediately after the mask, $\tilde{E}_m(x, \omega)$ [49]

$$\tilde{E}_m(x, \omega) \sim M(x)\tilde{E}_{in}(\omega)e^{-(x-\alpha\omega)^2/w_0^2} \quad (3.1)$$

where

$$\alpha = \frac{\lambda^2 f}{2\pi c d \cos(\theta_d)} \quad (3.2)$$

is the spatial dispersion with units $\text{cm}(\text{rad/s})^{-1}$ and

$$w_0 = \frac{\cos(\theta_{in})}{\cos(\theta_d)} \left(\frac{f \lambda}{\pi w_{in}} \right) \quad (3.3)$$

is the radius of the focused single frequency component at the masking plane. $\tilde{E}_{in}(\omega)$ is the input beam, w_{in} its radius before the first grating, c is the speed of light, d is the grating period, λ is the wavelength, and θ_{in} and θ_d are the input and diffracted angles from the first grating. Note that Equation 3.1 is in general a nonseparable function of space and frequency, because the spatial profiles of the focused spectral components can be altered by the mask (a component may impinge on abrupt amplitude or phase steps). This results in an output field which may be a coupled function of space and time. To obtain an output field which is a function of frequency or time only, an appropriate spatial filtering should be made. We take, in the expansion of $\tilde{E}_m(x, \omega)$ in Hermite-Gaussian

modes¹, the lowest coefficient $H(\omega)$ as filter function

$$H(\omega) = \left(\frac{2}{\pi w_0^2} \right)^{1/2} \int dx M(x) e^{-2(x-\alpha\omega)^2/w_0^2} \quad (3.4)$$

This Equation shows that the actual filter in the frequency domain $H(\omega)$ is the mask function $M(x)$ convolved with the intensity profile of the beam. This convolution effectively limits the spectral resolution $\delta\omega$ of the pulse shaper to $\delta\omega \cong (\ln 2)^{1/2} w_0/\alpha$, with the consequence that features on the mask smaller than $\sim w_0$ are smeared out by the convolution, and that wavelengths shorter than $\sim w_0$ are diffracted out of the main beam, leading to phase-to-amplitude conversion effects [49]. Through the Fourier Transform, this corresponds to a window T in the time domain $T = 4 \ln(2)/\delta\omega$ constituting an upper limit for the applicable time delay and stretching on the shaped pulse through the manipulation of the spectral phase. Finally, the pulse output by the pulse shaper will be

$$\tilde{E}^{OUT}(\omega) = H(\omega) \tilde{E}^{IN}(\omega) \quad (3.5)$$

thus the mask behaves like a linear filter for the input pulse. In the time domain, the filter is characterized by an impulse response function $R(t)$, the Fourier transform of the frequency domain filter. The output $E^{OUT}(t)$ of the filter in response to an input pulse $E^{IN}(t)$ is given by the convolution

$$E^{OUT}(t) = \int dt' E^{IN}(t') R(t-t') \quad (3.6)$$

thus the problem of generating a specific output pulse shape is equivalent to the task of fabricating a linear filter with the desired impulse response, clarifying why the frequency domain approach is favourable [48].

Diffraction based liquid crystal spatial light modulator

The first proposed masks were fixed, in the sense that for every experiment a single mask was lithographically fabricated and placed in the $4f$ -line. Nowadays versatile programmable masks are widely adopted. The optical properties of such devices are dynamically controlled by a software, and changed when

¹The Hermite-Gaussian modes (labelled as TEM_{nm}) are approximate solutions of the wave equation of an electromagnetic field, valid for weak focusing. They describe the spatial intensity profile of a propagating field in an homogeneous medium and are given by the product of a Gaussian function, a Hermite polynomial, and a phase term. The modes are constant distributions during the propagation.

needed, without physically removing the mask from the pulse shaper. The device we used in the experiments of this Thesis belongs to this category: it is a two-dimensional programmable **liquid crystal spatial light modulator** (LC-SLM) [49].

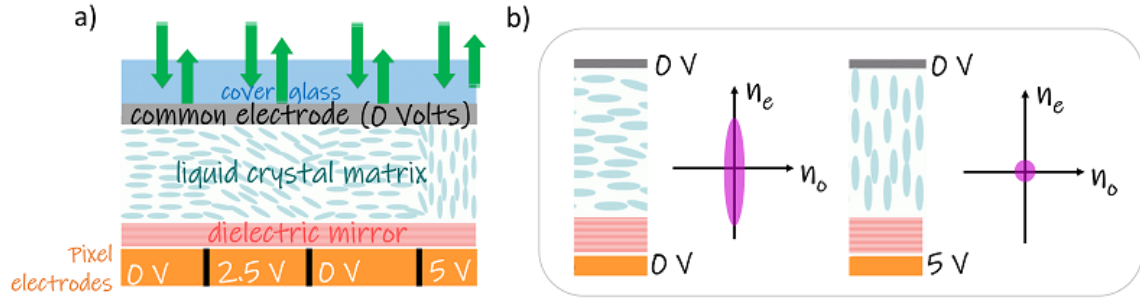


Figure 3.4: a) Transverse section of a LC-SLM. From left to right, the effect of the application of an increasing voltage results in a rotation of the liquid crystals. b) Ordinary (n_o) and extraordinary (n_e) refractive indexes of the liquid crystal layer for different applied voltages.

The structure of a LC-SLM is shown in Figure 3.4, where its transverse section is sketched. A thin layer of nematic liquid crystals (LCs) is sandwiched between two glass substrates. The LCs are long rod-like molecules oriented parallel to the substrate when no voltage is applied; instead, when a voltage is applied, they tend to align along the field. This situation is sketched in Figure 3.4. The voltage modifies the birefringence of the medium, leading to a modification of the optical path for light polarized along the anchorage direction (where the beam experiences a refractive index n_e , opposed to the ordinary refractive index n_o). The phase delay $\varphi(\omega, V)$ introduced by the changing voltage V is quantified as

$$\varphi(\omega, V) = \frac{\omega \Delta n(\omega, V) d_{LC}}{c} \quad (3.7)$$

where $\Delta n = n_e - n_o$ is the change in the refractive index and d_{LC} is the thickness of the liquid crystal layer. In order to apply the electric field that will induce such phase change, the inside surface of each glass layer is coated with a thin, transparent, electrically conducting film of indium tin oxide. One piece is patterned into a number of separate electrodes (or pixels) with the corresponding fan out for electrical connections. The modulator array is controlled by a special drive circuit which generates separate, variable amplitude signals to achieve inde-

pendent, gray-level phase control of all the elements.

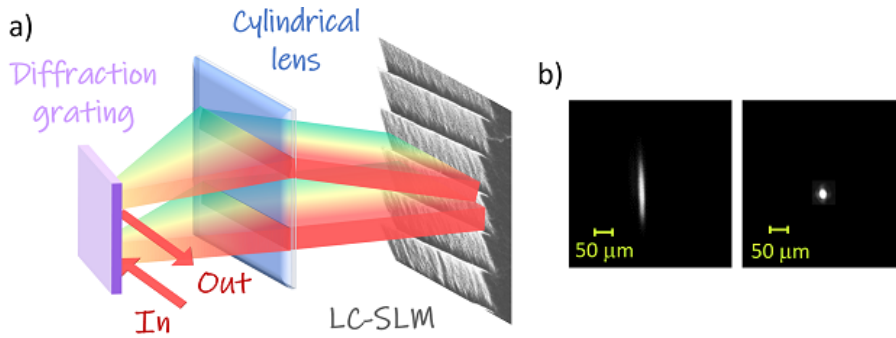


Figure 3.5: a) Diffraction based pulse shaping using a $4f$ line in reflection geometry. The mask, a liquid crystal spatial light modulator (LC-SLM), diffracts the radiation through the diffraction grating and cylindrical lens used to disperse and focus the beam. b) CCD camera image of the beam focus after the pulse shaper applying a blazed grating with constant period (left) and with a correction (right) accounting for the wavelength change.

To simultaneously shape both the phase and amplitude of femtosecond laser pulses, we used a **diffraction-based method** [50]. The $4f$ line is reproduced in a folded geometry, as shown in Figure 3.5. This means that the beam reaches the mask plane after the first lens-grating pair and is reflected back through the same optics, as the LC-SLM comprises a dielectric mirror (see Figure 3.4). More specifically, the beam is *diffracted* back. In fact, the beam is dispersed horizontally, and a sawtooth phase function, reproducing a blazed diffraction grating, is applied along each vertical direction [50]. For this reason a cylindrical lens is used instead of a spherical one, as the former focuses the spectral components only along one axis (in the present case the horizontal one).

The exit angle of the first-order diffracted light for a given wavelength is determined by the period of the sawtooth phase function, as can be seen from the blazed grating equation

$$d [\sin(\theta_m) - \sin(\theta_i)] = m\lambda \quad (3.8)$$

where d is the grating period, m is the order of diffraction, λ the wavelength of the spectral component, θ_i and θ_m the angles of incidence and diffraction of the beam. A sketch of the beam geometry when using a diffraction grating

is sketched in Figure 3.6 [39]. If the period is constant along the horizontal direction, being the spectral bandwidth large, each spectral component will experience a slightly different diffraction angle. This is taken into account, in our setup, by changing the diffraction period, along the horizontal direction, proportionally to the wavelength. The procedure adopted to find the coefficient at each point is phenomenological. We focus the beam after the pulse shaper and select with an iris the first order of diffraction. A CCD camera image of the beam focus is shown in Figure 3.5. We observe that, if the period is constant, the shape of the focus is elongated, reflecting the change in the diffraction angle. If a proper correction is applied, the spatial dispersion is corrected and all the components focus at the same point.

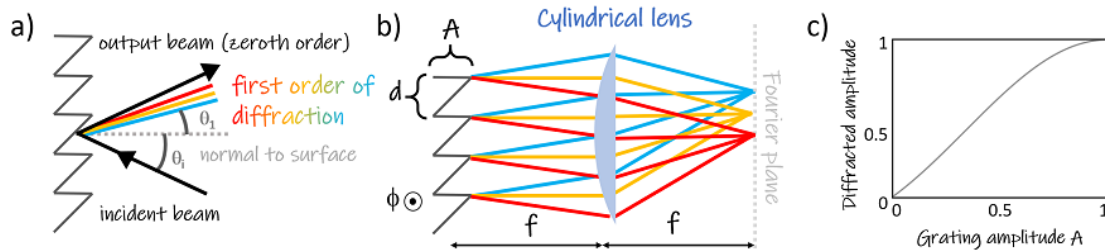


Figure 3.6: a) Reflective blazed diffraction grating, showing the angle dependence of the diffracted intensity on the wavelength. b) Scheme of the top view on a diffraction based pulse shaping: the incident beam is diffracted and recollimated. The parameters of Equation 3.10 are reported. The phase ϕ is varied along the direction orthogonal to the page plane. c) Amplitude of the diffracted field as a function of the sawtooth amplitude $A(\omega)$.

The amplitude of the sawtooth phase function determines the efficiency of the diffraction grating, thus ruling the amount of light that is sent to the first order of diffraction and the light that is reflected back to the zeroth-order. The phase of the light is instead determined by the relative vertical shift of the sawtooth, as two adjacent spectral components, at the same vertical position, will experience different phases. These expectations find a justification in the expression of the diffracted field at the Fourier plane of a lens (plotted in Figure 3.6), calculated in terms of Fraunhofer diffraction

$$E(\omega) \propto \exp[-i\phi(\omega)] \operatorname{sinc} \left[\pi - \frac{\alpha}{2} A(\omega) \right] \quad (3.9)$$

for a phase modulation of the form

$$\Phi(\omega, y) = \alpha \left\{ \frac{1}{2} + A(\omega)S_d[\phi(\omega), y] \right\} \quad (3.10)$$

where $S_d[\phi(\omega), y]$ is the sawtooth function, depending on the vertical dimension y and on the frequency along the horizontal axis via $\Phi(\omega, y)$, the phase of the grating. $A(\omega)$ is the amplitude of the sawtooth (ranging from 0 to 1), and α is the maximum phase shift achievable by the LC-SLM, in the present case $\alpha \approx 2\pi$. We note that, even when $\alpha < 2\pi$, a phase shift of 2π can still be obtained as ϕ in Equation 3.9 does not depend on α . On the other hand, there would be no benefit in using values $\alpha > 2\pi$ even if the LC-SLM allows them [50]. This is one of the reasons why we have limited the range of operation of our LC-SLM to $(0, 2\pi)$.

The diffraction based LC-SLM is a very versatile tool: being the pixels independent, the parameters of the sawtooth phase function can be controlled line by line, in other words frequency by frequency. Applying the proper voltage matrix on the liquid crystals, a *pattern*, we can control and manipulate the spectral phase of each pulse and shape the outcome at our needs, for example to compensate or introduce a functional dependence on frequency (a *chirp*), to split the pulses in time, to select a portion of their spectral content [48]. In any case, before employing the diffraction based LC-SLM, a few preliminary steps have to be taken to completely define the correspondence between the pattern and the mask. First, to establish a relation between the applied voltage and the actual applied phase on the light fields, we need to perform a *phase calibration* of the pulse shaper. Then we relate the sawtooth depth to the diffracted intensity by performing an *amplitude calibration*. Finally a *frequency calibration* must be performed to establish the frequency dependence of the horizontal coordinate of the liquid crystal matrix (and of the photodiode arrays). The details of the pulse shaper calibrations are reported in Appendix C.

Our aim is to apply a **random pattern** to the pulses in order to destroy their spectral phase coherence. As shown in Figure 3.7, we can pick, point by point, random values for $\phi(\omega)$ and $A(\omega)$, resulting in random shifts of the gratings or in a random modulation of their amplitude. Because of the continuity of the liquid crystal layer, anyway, adjacent pixels can be coupled resulting in a false phase distribution that differs from the input one. Therefore we use a software

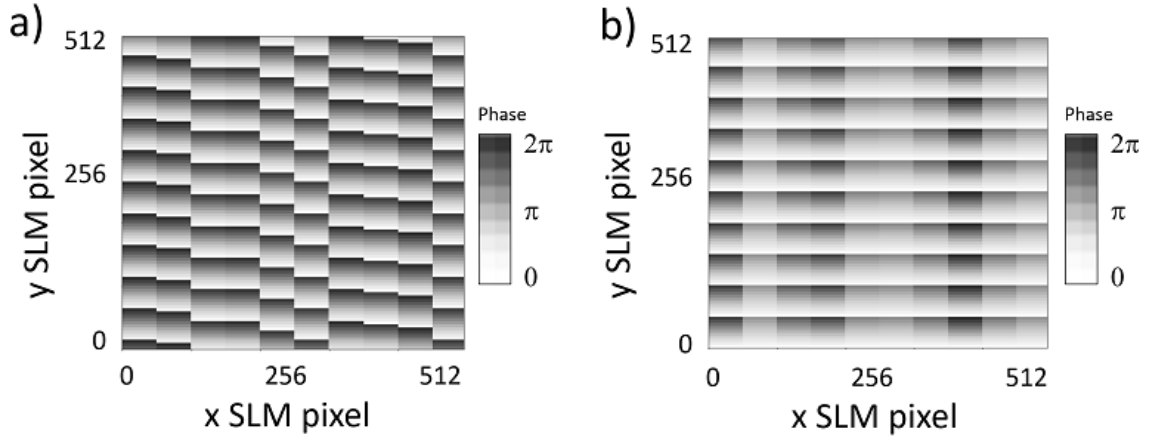


Figure 3.7: Front view of the spatial light modulator matrix when a diffraction grating is applied with randomized a) phase and b) amplitude.

to generate an array of uniformly distributed random phase values ϕ^U and then perform a gaussian smoothing of such array following the formula

$$\phi^S(i) \propto \sum_{j=-i}^{512-i} \phi^U(i+j) e^{-\frac{(i+j)^2}{\Delta_{corr}}} \quad (3.11)$$

where the smoothed phase value ϕ^S is calculated at the i^{th} pixel by summing over the neighboring phase values weighted by a gaussian coefficient.

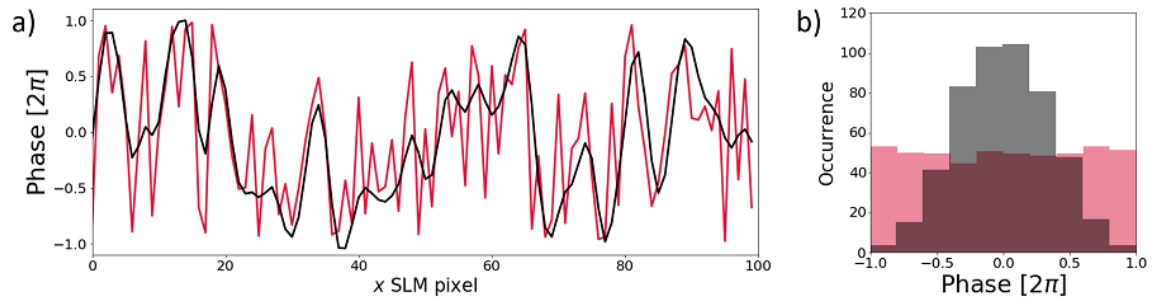


Figure 3.8: a) Uniformly distributed phase noise (red curve) and gaussian smoothed phase noise (black curve). b) Histogram of the uniformly (red) and gaussian smoothed (black) phase noise.

In Figure 3.8 we show the phase values for a selected number of SLM pixels when generated with a uniform distribution and after the gaussian smoothing, along with the histogram of the distributions. The variance of the gaussian weight Δ_{corr} is the experimental counterpart of Equation 2.41, as it represents the frequency resolution. Below its value, the frequency components are statistically correlated. Taking into account the width of the focus of a single

frequency component on the LC-SLM matrix, and setting $\Delta_{corr} = 2$ pixels, we get $\Delta_{corr} \approx 0.2$ THz. This value is obtained by convolving Δ_{corr} with the resolving power of the linear photodiode arrays, as it necessarily impacts the frequency resolution of the method.

Finally, we mention the speed of the LC-SLM in updating the pattern. Some programmable devices have a high (\approx kHz) refresh rate that is comparable to laser repetition rates [48]; our LC-SLM's speed is in practice limited by the liquid crystals rotation time, thus about 500 Hz. This means that, even if the LPDAs can acquire every spectrum, there are chunks of about 10 spectra with the same random pattern, which are therefore completely spectrally correlated. We average over this subset of spectra and obtain a single spectrum for each applied pattern. When analyzing the data, therefore, we use this as single shot spectrum.

3.1.3 ■ Detection

The detection apparatus is able of measuring shot by shot the pulse spectrum. It is made of two identical spectrometers, one for the reference beam and one for the probe beam (they can also be used to detect two orthogonal polarizations of the probe). Each spectrometer is composed by a diffraction grating to disperse the beam, a spherical lens to focus the components and a linear photodiode array (PDA). The PDAs are arrays of 256 silicon square pixels, 5 μm wide, manufactured by Hamamatsu. They are part of a in-house made readout system. The signal from the PDAs is digitized by an analog to digital converter (ADC) and manipulated in a LabView environment.

Before the acquisition, the software updates the pattern on the LC-SLM. The two 256-long arrays of voltage data are displayed and stored, and the acquisition is repeated many times with a different random pattern on the SLM. While the measured values are input to the covariance to calculate the experimental correlation coefficients, we must establish a relation between the pixel index and the frequency of the intensity it measures. To do so we use the pulse shaper, in a procedure that will be explained in detail in Appendix C.

3.2 ■ Double stage optical parametric amplification

In this section we describe the device used to frequency convert the pump beam with the aim of performing non degenerate double pulse experiments. Specifically, we change the energy of the pump from the visible to the near infrared. To achieve this we exploit nonlinear processes in a double stage optical parametric amplifier (DS-OPA), which allows the output spectrum central wavelength to be tuned.

The conversion is based on a process taking place in BBO crystals. This crystal lacks inversion symmetry ($\chi^{(2)} \neq 0$), therefore supports second order nonlinear effects, such as difference frequency generation (DFG) [51]. By historical convention, of the three beams taking part in DFG, the beam with the highest frequency ω_p is called **pump**, the beam at frequency $\omega_s < \omega_p$ is called **signal** and the beam with difference frequency $\omega_i = \omega_p - \omega_s$ is called **idler**. In the present case, the pump is represented by the laser pulse, and the signal we aim to produce is the near infrared beam. Therefore the idler is an infrared beam that will be emitted to conserve the total energy, and that we will discard. A sufficiently intense pump will produce in a BBO very weak signal and idler beams, and in this case the process is called spontaneous fluorescence. If a signal field is instead input in the BBO, overlapped in time and space with the pump beam, the conversion is stimulated and can reach higher efficiency. In this case the process is called *parametric downconversion* (PDC), and the input signal to be amplified is named **seed**.

To generate a seed beam we separate a small intensity portion from the pump beam and broaden its spectrum up to the infrared. This is achieved through *self-phase modulation*. If a material allows third order effects, its index of refraction acquires a term proportional to the time dependent intensity I of the beam $n(I) = n(t) = n_0 + n_2 I(\mathbf{r}, t)$, where n_0 is the equilibrium refractive index. As the transverse intensity profile of a laser beam is usually Gaussian, the index of refraction acquires a spatial dependence that produces an effective lens, causing the beam to collapse, an effect called *self-focusing*. Simultaneously the beam acquires a time dependent phase and is stretched in time, while its spectrum broadens, in a *supercontinuum* (SC). We produce it in an yttrium

aluminum garnet (YAG), as the output of such crystal is known to be characterized by more energy density in the near-infrared as compared to the commonly used sapphire [52].

We built a double stage optical parametric amplifier, each stage being based on a BBO crystal to generate infrared radiation. There are two main advantages in using two separate stages. First, they are optimized separately, which leads to an improved output stability. Moreover, the stages are dedicated to different tasks: the first to the selection of the output wavelength, the second to its amplification. BBO crystals can accomplish both tasks, because of their birefringence. In fact, for nonlinear effects to take place efficiently in a medium the *phase matching condition* $\Delta k = 0$ must be satisfied, representing the momentum conservation between the input and output beams. It is not generally fulfilled in a medium, where the refractive index is a monotonically growing function of frequency (far from atomic resonances). In a birefringent medium, combining the choice of its internal cut angle with the input beams direction and polarization, phase matching can be achieved and the time overlap of the three fields maintained through the crystal. As we are dealing with broadband pulses, the description of the process is more complicated. The group velocity mismatch (GVM) between the pump and the amplified pulse limits the interaction length over which parametric amplification takes place, while GVM between the signal and the idler beams limits the phase matching bandwidth.

We show in Figure 3.9 a simplified scheme of our DS-OPA, whose layout is described in the Figure caption.

The wavelength ranges attainable at the NOPA output range from roughly $1.1 \mu\text{m}$ to $1.5 \mu\text{m}$. The reason for this is that the BBO absorbs radiation below $\sim 1 \mu\text{m}$, and the upper limit is instead given by the very few photons produced by the YAG in that region. Typical output spectra at $1.21 \mu\text{m}$ and $1.3 \mu\text{m}$ are shown in Figure 3.10, compared to the corresponding NOPA signal prior to the amplification. The bandwidth is largely reduced, and the energy per pulse is 20 times higher, as the NOPA signal has roughly $1 \mu\text{J}$ per pulse. The OPA output's duration is close to the transform limit (it was measured using the FROG technique, topic of Section 3.3). We note that the NOPA spectra show a dip at ~ 1.25

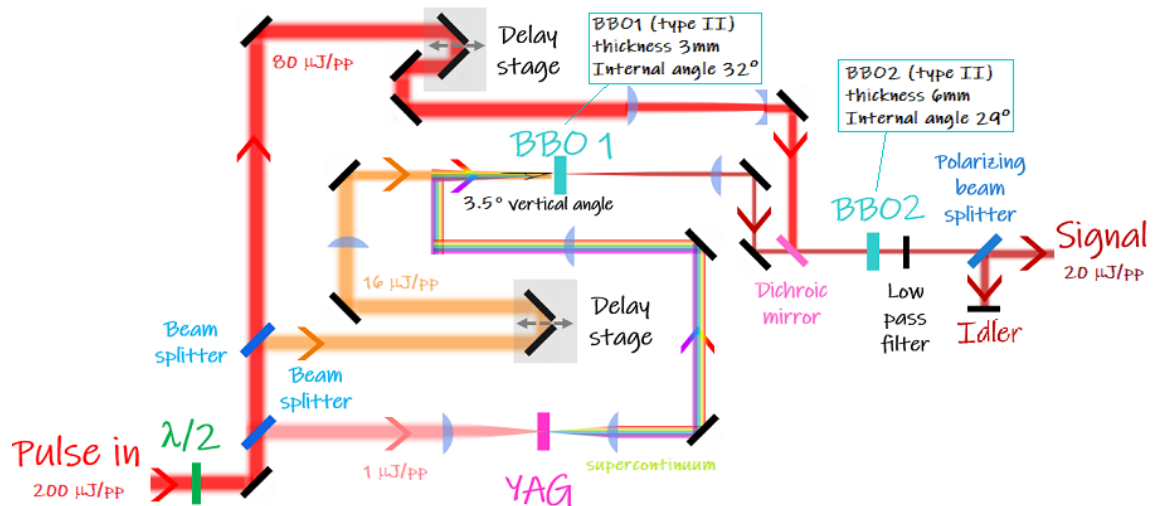


Figure 3.9: Scheme of a double stage optical parametric amplification setup. The laser beam is input in the optical board. About 1% of it, is focused into the YAG crystal to drive the supercontinuum generation. The latter is collimated and sent to seed the first BBO (BBO1). The transmitted laser beam is split in two portions, to act as pump respectively in the first noncollinear stage (NOPA) and second collinear stage (OPA). The spectral portion of the seed to be amplified is selected by fine tuning the angle of BBO1 mount. In the present configuration as much as the 25% of the pump intensity is transferred to the near infrared beam in the second stage. Finally, a filter eliminates the pump, and a polarizing beamsplitter selects the signal.

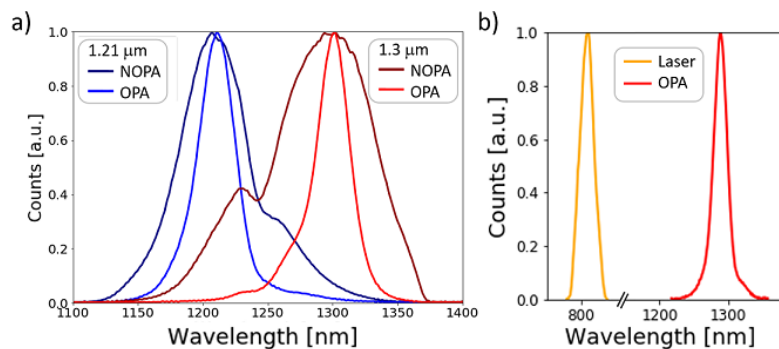


Figure 3.10: a) Output spectrum at 1.21 μm and 1.3 μm (blue and red curves) after the first (dark hues) and second (light hues) amplification stage. b) Measured pump spectrum input (orange) and output (red) by the DS-OPA.

μm, and that the intensity drops at ~1.37 μm: both effects are due to absorption by water vapour deposited on BBO1 surface, impacting the SC spectrum [51].

The near infrared pulses were used as pump in a double pulse configuration.

To do so, the beam was routed into the DS-OPA and, after the frequency conversion, focused on the sample in a nearly collinear configuration with the aid of a dichroic mirror. The optical path of the probe was consequently increased to compensate for the optical path difference.

3.3 ■ Measurement of the pulse duration

This final section is dedicated to the method used to estimate the duration of an ultrashort pulse. To retrieve the time dependent electric field of an ultrashort pulse, both the amplitude and the phase of each frequency component of an ultrashort pulse must be retrieved and input to a Fourier Transform. The Frequency Resolved Optical Gating (FROG) method is a way to retrieve the complete complex representation of a pulse, both in frequency and time. This method was devised to use a reference pulse as a *gate function* to scan the profile of a pulse to be measured. If a short reference pulse is available, this is used as gate; otherwise a replica of the unknown pulse acts as gate [53]. This is the method we adopted, and that will be described in the following.

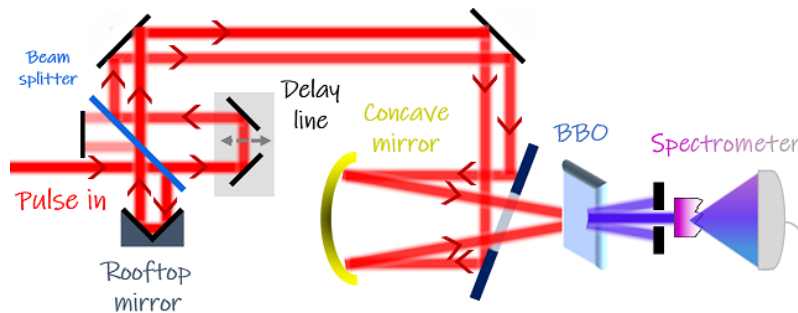


Figure 3.11: Scheme of a frequency resolved optical gating setup.

As shown in Figure 3.11, the pulse to be measured is split in two by a beam splitter. The reflected beam is sent back through the same beam splitter by a roof mirror (whose surface is inclined to form two faces sharing an edge at a 90° angle), while the transmitted beam is routed through an electronic delay stage which introduces an optical path difference. The two beams then travel in parallel up to a concave mirror, which focuses them on a BBO crystal, in which sum frequency generation and second harmonic generation take place [51]. The sum frequency beam intensity is then measured by a commercial spectrometer while the time delay τ between the two beams is scanned, generating a spec-

trogram

$$S^{FROG}(\omega, \tau) = \left| \int_{-\infty}^{+\infty} dt E(t) E(t - \tau) e^{i\omega t} \right|^2 \quad (3.12)$$

where the delayed electric field $E(t - \tau)$ acts as the gate, scanning the profile of the field to be measured, $E(t)$, belonging to the same pulse. A measure of $S^{FROG}(\omega, \tau)$ is enough to completely characterize $E(t)$. The field is obtained by means of an iterative phase retrieval algorithm that starts from a guess for $E(t)$ and uses as constraints the following relations on the frequency doubled field $E_{FD}(t)$: the squared modulus of its Fourier Transform must coincide with the measured FROG trace for every delay τ , and $E_{FD}(t)$ must result from $E(t)$ undergoing a known nonlinear process [53].

As mentioned above, the role of the BBO in the FROG is to generate the sum frequency beam to be measured. Let us start, for the sake of simplicity, by describing the case of monochromatic beams with wavelength $\lambda = 800$ nm. When one of the beams is focused on the BBO, the crystal doubles its the frequency content, in other words generating light with wavelength $\lambda = 400$ nm. If the beams overlap in space and time on the BBO, the crystal sums the two beams by generating an output with $1/\lambda_{OUT} = 1/\lambda_1 + 1/\lambda_2$, resulting in $\lambda_{OUT} = 400$ nm. The input beams hit the BBO crystal non collinearly, and the output wavevectors can be inferred by considering the conservation of the total momentum. Therefore each of the frequency doubled beams will propagate in the same direction of its parent beam, while the sum frequency beam will propagate in the middle, being its wavevector given by the sum of the parent beams momenta. This picture holds for every component in the bandwidth of a broadband pulse. Nonetheless, as mentioned in the Section 3.2, the BBO crystal has an efficiency bandwidth limiting the actual output spectrum for the sum generation. This necessarily impacts the result of a FROG reconstruction, as the measured spectrum might be underestimated, resulting is an overestimation of the duration of the pulse.

By means of the FROG technique, we measured the pulse duration of the laser pulse at its fundamental wavelength (800 nm) and output from the DS-OPA (tunable). In Figure 3.12 we show the reconstructed electric field as a function of time and its complex spectrum. A fit performed on the time de-

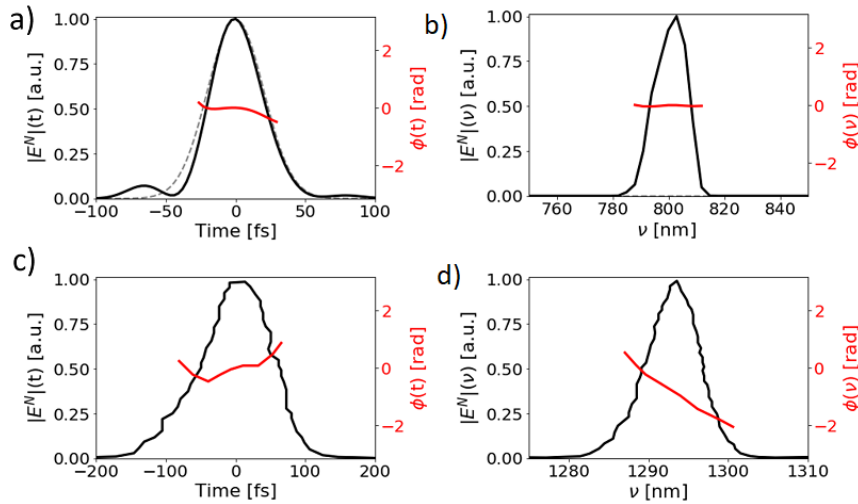


Figure 3.12: Reconstructed electric field in time (a,c) and frequency (b,d) of probe pulses when the central frequency is 800 nm (a,b) or 1290 nm (c,d). The blue dashed lines show the phase applied using the pulse shaper.

pendent electric field allows to estimate the pulse duration as the full width half maximum (FWHM) of the field envelope, resulting in 45 fs for the 800 nm pulse and 110 fs for the 1290 nm pulse. Both are very close to their transform limit.

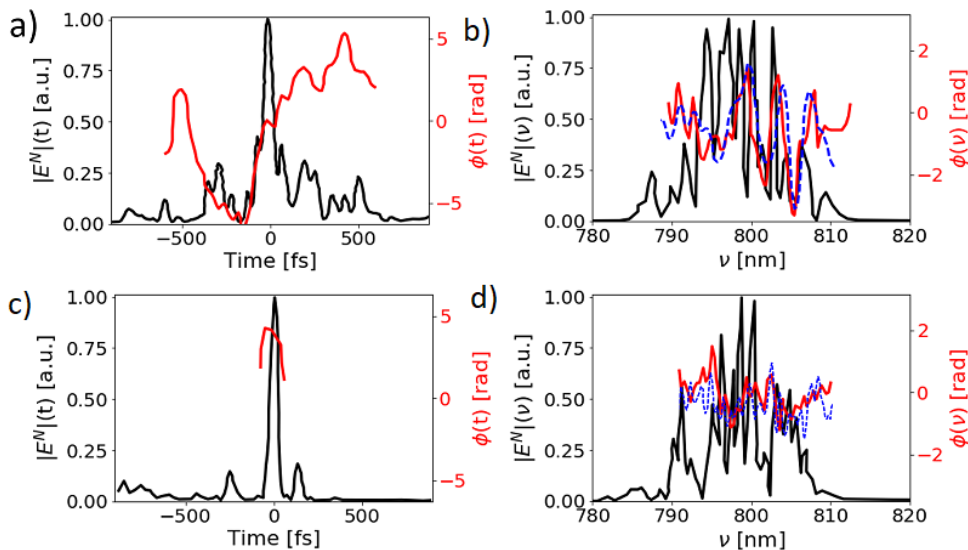


Figure 3.13: Reconstructed electric field in time (a,c) and frequency (b,d) of probe pulses when phase noise with $\Delta_{corr} = 4$ (a,b) or with $\Delta_{corr} = 2$ (c,d) is applied. The blue dashed lines show the phase applied using the pulse shaper.

In Figure 3.13 we show the result of a FROG reconstruction applied to a

shaped probe pulses with a stochastic spectral phase with spikes having average width $\Delta_{corr} = 4$ or $\Delta_{corr} = 2$. We start by noting that the reconstructed spectrum looks very noisy. A possible explanation for lies in the fact that a smooth spectrum with a randomized spectral phase undergoes a gating during the acquisition in the FROG setup, as the latter is performed through a discretized detector. The reconstructed spectral phase is compared (rightmost graphs) to the spectral phase as generated by the pulse shaper software (blue dashed line). The FROG technique does not allow for an accurate retrieval of the spectral phase. This might be due to the fact that the measured spectrum does not correspond to the actual one. The result of this computation is nonetheless very interesting, and can be confirmed by a simple simulation. In fact **the time profile shows a central intense and short spike**. This feature has a duration which is inversely proportional to the pulse bandwidth, and its amplitude is inversely proportional to the spectral phase correlation length. In fact, at the sides of such a peak, weaker spikes arise, whose amplitude relatively to the central spike, instead, increases proportionally to the correlation length. This is what we observe in the result of the FROG retrieval of pulses with $\Delta_{corr} = 2,4$ whose result is shown in Figure 3.13.

This peculiar temporal structure was shown to actually provide an advantage. To understand why, let us consider the fact that a pump probe trace has a resolution determined, roughly, by the intensity autocorrelation of the pump and probe pulses, convoluted with the detector response [2]. Therefore, to gain insight on the expected resolution of a pump probe measurement, we start by calculating the intensity autocorrelation for any combinations of coherent and noisy temporal profiles.

When both pump and probe pulses are spectrally coherent, their autocorrelation is proportional (with a constant factor depending on the functional shape of the pulses) to the temporal width of the pulses [54]. In this case, in fact, both the pulses are fully coherent within their temporal envelope. The time profile of a noisy pulse is, instead, made of narrow spikes enclosed within the envelope. When two noisy pulses overlap, the most intense superposition takes place when the central narrow coherent spikes overlap. Therefore the autocorrelation trace is itself given by a short central spike referred to, in the literature,

as "coherent artifact", whose width is proportional to the average width of the narrow noisy spikes in the time profile. The random nature of the spikes position and separation in time gives rise to a broad average background with few hundreds femtoseconds duration [53]. Because of the fact that the noisy spikes are much narrower than the envelope, the coherent artifact is itself very short and the time resolution of a spectroscopic experiment is improved with respect to the experiment carried out with pulses with the same envelope and a smooth intensity profile [26, 27, 55–59]. Clearly the autocorrelation of a pair of pulses sharing the envelope, one coherent and one noisy has intermediate width between the two limiting cases, therefore the temporal resolution is still improved with respect to the standard configuration. In the present case, the time resolved measurements are carried out with a coherent pump pulse and a noisy probe. Because of the fact that both share the same spectrum, their time durations are comparable (as confirmed by the FROG reconstruction). Therefore, the time resolution is only slightly better than in the standard pump probe configuration (it cannot be worse, though). The correlation length is therefore primarily chosen to ensure a good spectral resolution, and is minimized. This choice also ensures that the temporal profile of the probe pulses is structured as seen above, with a central spike over a low background.

4 ■ Transmission experiments

In this chapter we report and discuss the data acquired in a transmission geometry from a 1 mm thick sample of α -quartz, in the framework described by the quantum model of Section 2.1. The chapter starts with the description of the main measurement categories enabled by the pulse shaper. In Section 4.1 we report the results obtained randomizing the whole spectral phase of the pulses, while in Section 4.2 we discuss the outcome of a partial randomization. Correlation data from this two sections was published in [14]. A set of spectra measured within all of the possible noise configurations is shown in Figure 4.1. The second part of the Chapter, divided in Sections 4.4 and 4.5 respectively, is devoted to a set of measurements performed modulating selected narrow peaks in the spectrum and to a systematic study on the probe pulse energy. Unless otherwise stated, the experiments performed in this chapter were carried out using pulses with 1.25 mJ/cm^2 incident fluence.

4.1 ■ Full modulation

We discuss the results of measurements obtained randomizing the spectral amplitude or phase of the pulses along their whole bandwidth. The applied phase values range between $-\pi$ and π . We can use a portion of this range, therefore a narrower phase distribution, whose width is indicated by a percentage, to be intended as multiplied by the full range and around zero.

Before discussing the effect of the randomization on the covariance based detection, we report a test aimed at understanding the relationship between the software applied phase distribution and the measured intensity deviation. We

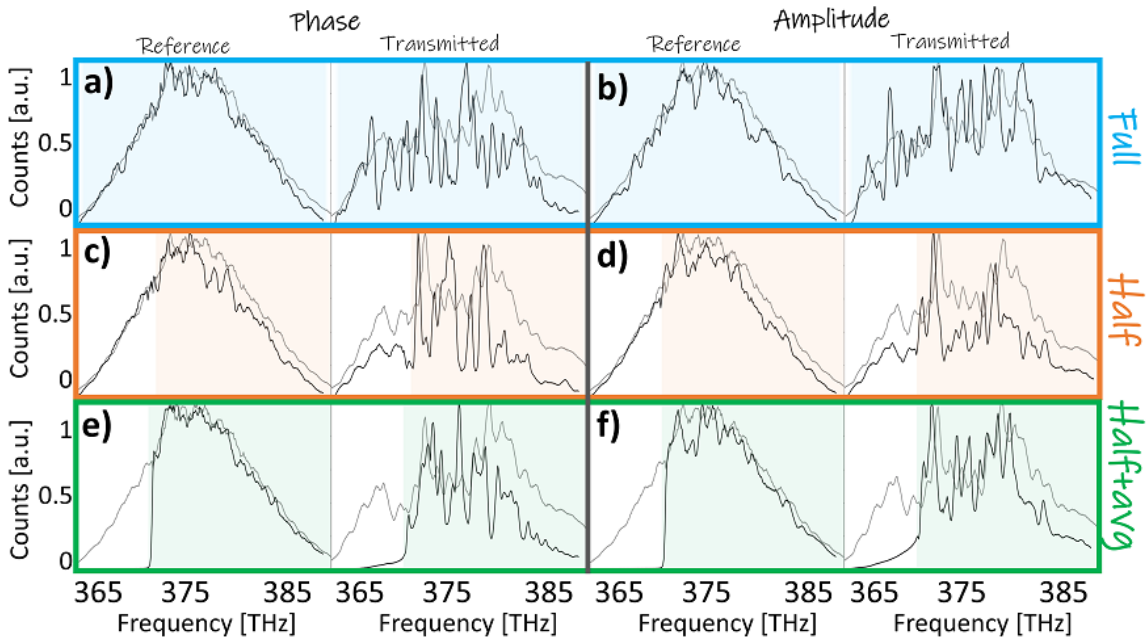


Figure 4.1: Possible types of randomization employed in the measurements shown in this Chapter. Modulation of the spectral phase and of the spectral amplitude along the whole bandwidth (a,b respectively) or of half of the spectrum (c,d). The average value of the spectrum can be modified for the whole set of pulses while randomizing the spectral phase (e) or amplitude (f). In all of the plots, the gray curve represents the non shaped pulse spectrum and the black the shaped one. We notice that the pulses illuminating the sample undergo self-phase modulation, visible as a broadening of the spectrum. This is a third order process as inelastic light scattering, thus the intensity regime we work with triggers both effects.

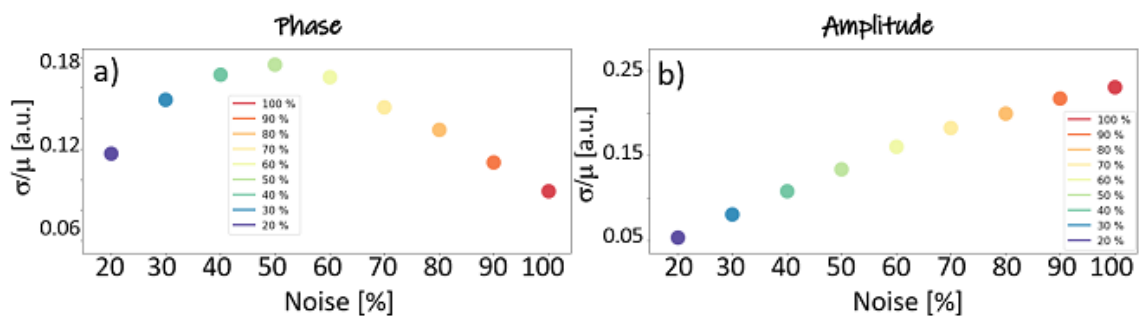


Figure 4.2: Dependence of actual noise range on the software applied phase. Ratio between standard deviation and average of the intensity (both averaged over the photodiode array pixels) plotted against the phase (a) or amplitude (b) noise percentage.

show in Figure 4.2 the standard deviation of the measured intensity (averaged over the photodiode array pixels) versus the applied noise percentage. The two

are linearly dependent when the amplitude is randomized. When phase noise is introduced, this is mapped proportionally into intensity fluctuations up to 50%, while for higher factors the standard deviation decreases. This is consistent with the picture given in Chapter 2, where we discuss how any phase modulation is imprinted in the spectral profile and is visible in the detected intensity. We deduce that the "background" correlation will be the lowest for a 50% phase noise, at which the visibility of any sample induced correlations will be the highest, but does not necessarily imply an enhancement on the magnitude of the signal. We will discuss again this point shortly (see Figure 4.4). In the following, we show measurements performed using a noise range of 50% on the spectral phase or on the spectral amplitude. The chosen correlation length is $\Delta_{corr} = 2 \text{ pixels} \simeq 0.22 \text{ THz}$.

We turn now to the covariance based transmission measurements performed on α -quartz. In Figure 4.3 we plot a few representative spectra obtained after the application of noise on the spectral phase or amplitude, and the correlation coefficients ρ calculated on the measured reference and transmitted beams. We notice that fluctuations in the transmitted spectra are far more pronounced than in the reference spectra, as the interaction process amplifies their magnitude (and self-modulation takes place in the sample). The reference correlation coefficient is zero outside of the diagonal, which is close to one and whose width is proportional to the correlation length. **The sample correlation coefficient shows clear off diagonal features.** A negative region around the diagonal is followed by a quasi-zero region and by a positive plateau. The position of the edges between these regions, evaluated by expressing the frequency axes as a frequency distance, is found to match the frequency of two vibrational modes of the α -quartz sample, at 6.2 THz and at 14 THz. At a closer inspection, in the negative region, particularly of the phase randomized correlation coefficient, a deeper blue area can be distinguished, whose edge falls at the lowest frequency α -quartz vibrational mode at 3.8 THz. Finally, inspecting the average value of the correlation coefficient along the diagonal direction, a weak positive feature can be seen, matching the frequency of the vibrational mode at 10.7 THz. Therefore the signal is, in this measurement, represented by dispersive peaks on top of a shifting background. As we will discuss in the following sections, this peculiar lineshape can be attributed to the coherent sum of the scattered

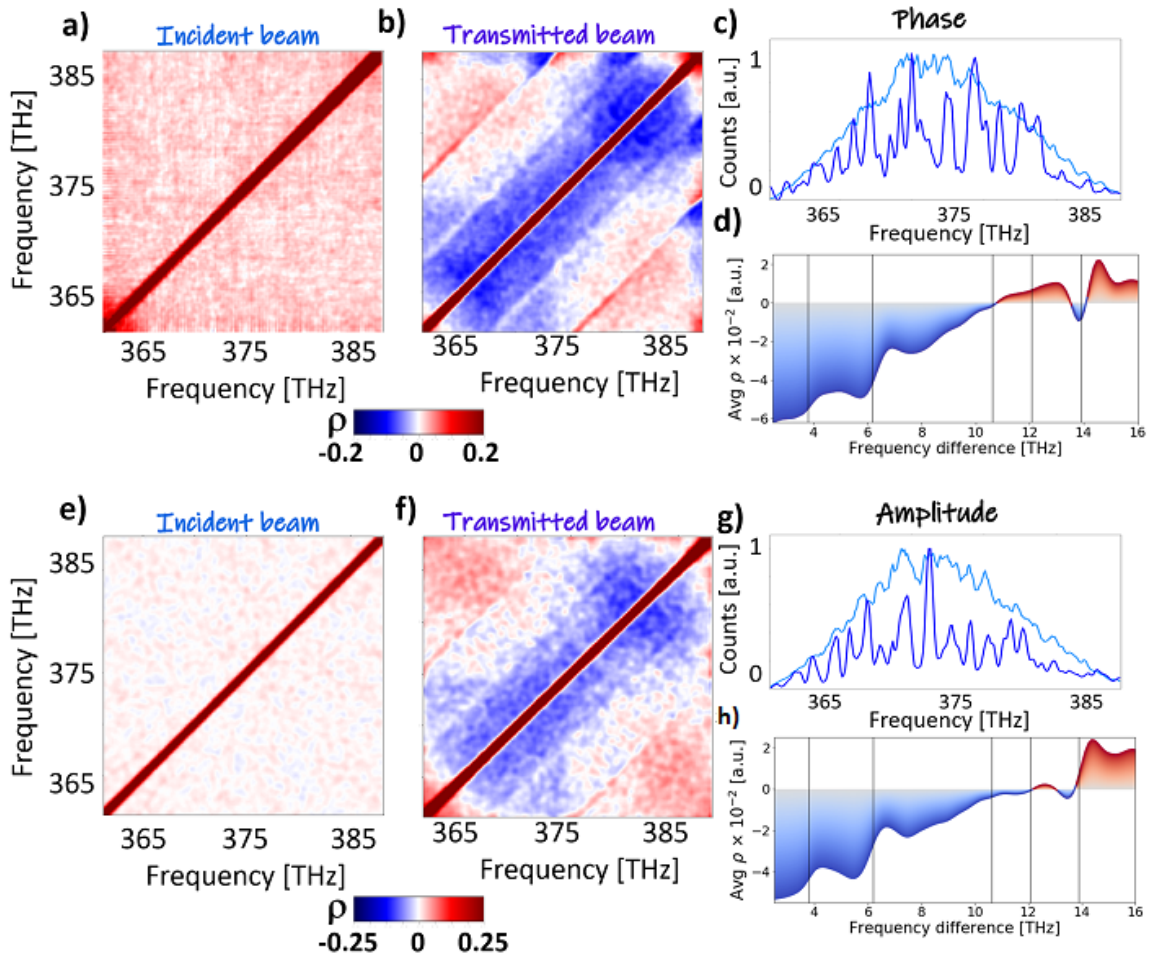


Figure 4.3: Measurements performed randomizing the spectral phase (a-d) or amplitude (e-h) along the whole bandwidth. Example of reference (light blue) and transmitted (dark blue) spectra when randomizing the c) phase or g) amplitude. The respective low energy vibrational spectrum, retrieved by integrating the signal along the diagonal, is shown in panels d) and h), where the vibrations of α -quartz are indicated by vertical lines for comparison [41].

classical field to the non interacting field. Nonetheless, results obtained within traditional nonlinear spectroscopic techniques suggest that a dispersive line-shape could result from contributions of different competing quantum pathways [60–62] or from a mixing of a resonant and a non resonant contribution [63]. The positions of the signal nodes are in very good agreement with the phonon frequency of quartz from the literature [41].

There is a striking similarity between the signal arising in the covariance map calculated randomizing the spectral phase or the spectral amplitude. A

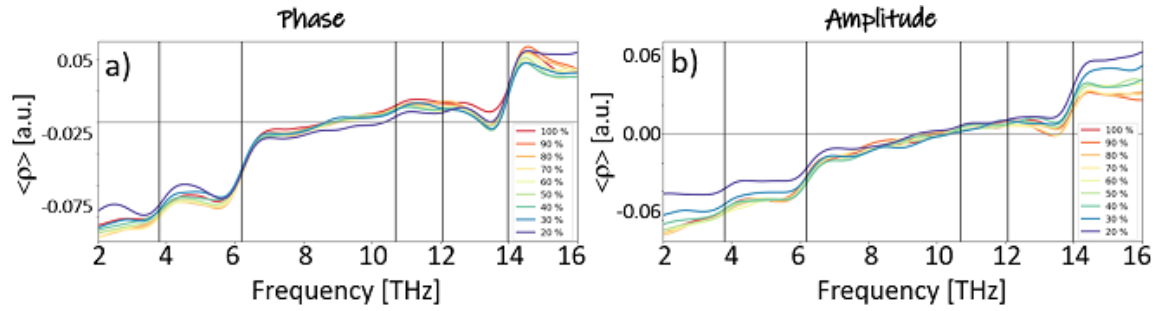


Figure 4.4: Correlation coefficient from the transmitted beam as a function of the frequency difference, changing the value of the a) phase or b) amplitude noise percentage applied.

possible explanation for this behaviour is that the randomized pulses behave the same during the interaction with the sample. The inelastic scattering process takes place regardless of the shape of the pulses, as long as the intensity is high enough to trigger a nonlinear process. Therefore the pulse randomization has the great advantage of removing, from the correlation coefficient, the source spectral coherence. The gating performed by the detectors makes the actual statistical properties of the phase modulated pulses "visible" to the correlation coefficient. To confirm this hypothesis, we scanned the possible noise percentages and compared the signal. In Figure 4.4 we show the correlation coefficient value as a function of the frequency distance from the diagonal of the map. It can be noticed that the signal amplitude does not increase sensibly with the noise amplitude, for none of the two noise configurations.

We discuss in the following two more possible configurations for a stochastic probe, and compare the results obtained so far.

4.2 ■ Half modulation

During the scattering process under consideration, the scattered photons from any point ω_j in the spectrum overlap with the photons at the final frequency $\omega_j + \Omega$. To deepen our understanding of the self heterodyned nature of the signal on our covariance based technique, we performed measurements randomizing only half of the spectrum, and leaving the rest spectrally coherent.

The results are shown in Figure 4.5. All the correlation coefficients split in

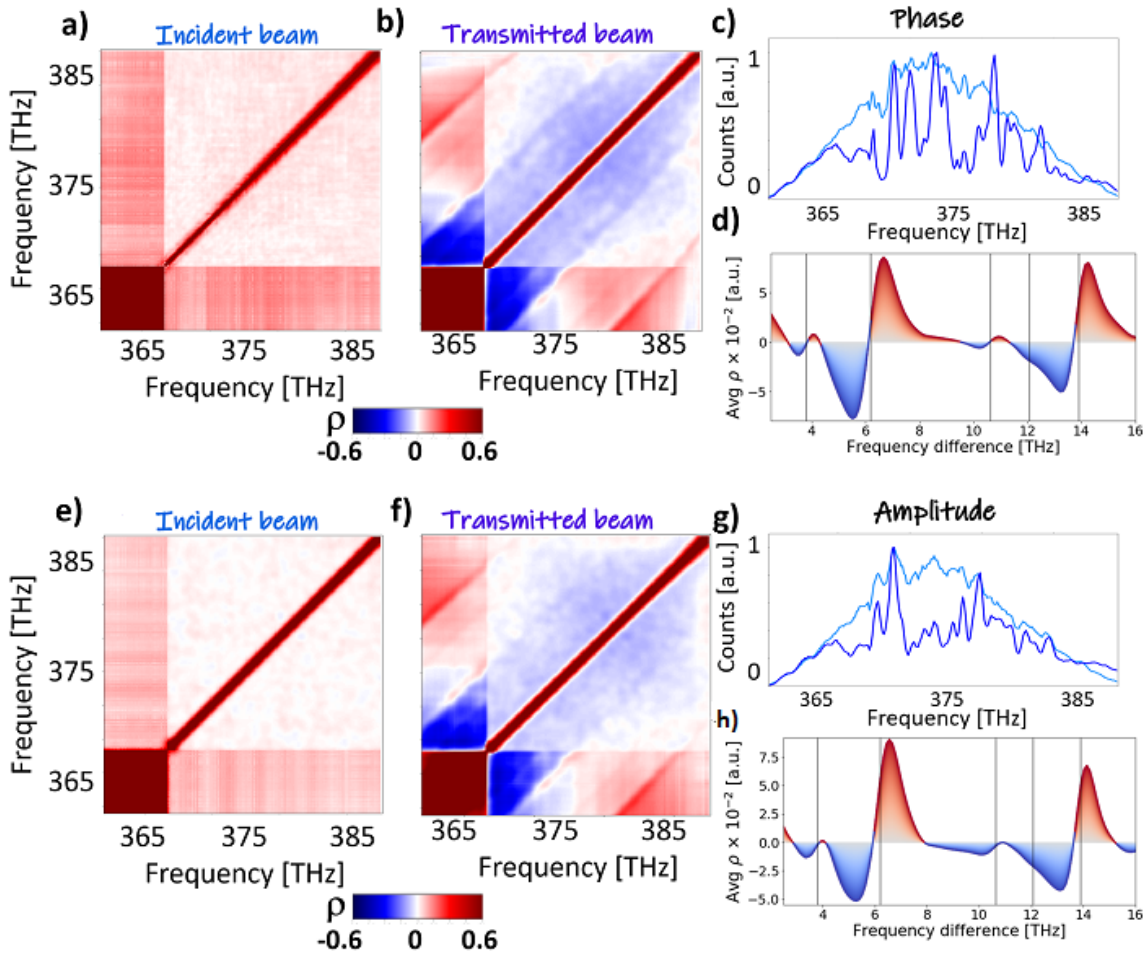


Figure 4.5: Measurements performed randomizing the spectral phase (a-d) or amplitude (e-h) along half of the bandwidth. Example of reference (light blue) and transmitted (dark blue) spectra when randomizing the c) phase or g) amplitude. The respective low energy vibrational spectrum, retrieved by integrating the signal along the diagonal, is shown in panels d) and h), where the vibrations of α -quartz are indicated by vertical lines for comparison [41].

blocks, representing the coupling between pairs of components belonging to different regions of the spectrum. They can both belong to the coherent side (low energy corner), both to the randomized side (high energy corner) or each to one side (lower right and upper left blocks). While the upper right block reproduces the results of the previous section, the clearest signal arises from the blocks coupling one component from the low frequency side and one from the high frequency side. The off-diagonal features reproduce neatly the low-energy vibrational spectrum of α -quartz. There is no clear distinction between the results obtained applying phase or amplitude modulation.

4.2.1 ■ Half modulation with mean value shaping

In a configuration where the high frequency side is modulated, we performed a set of measurements decreasing gradually the average amplitude of the coherent side down to zero, to study the signal dependence on this parameter. The energy per pulse was kept constant to work in a comparable fluence regime.

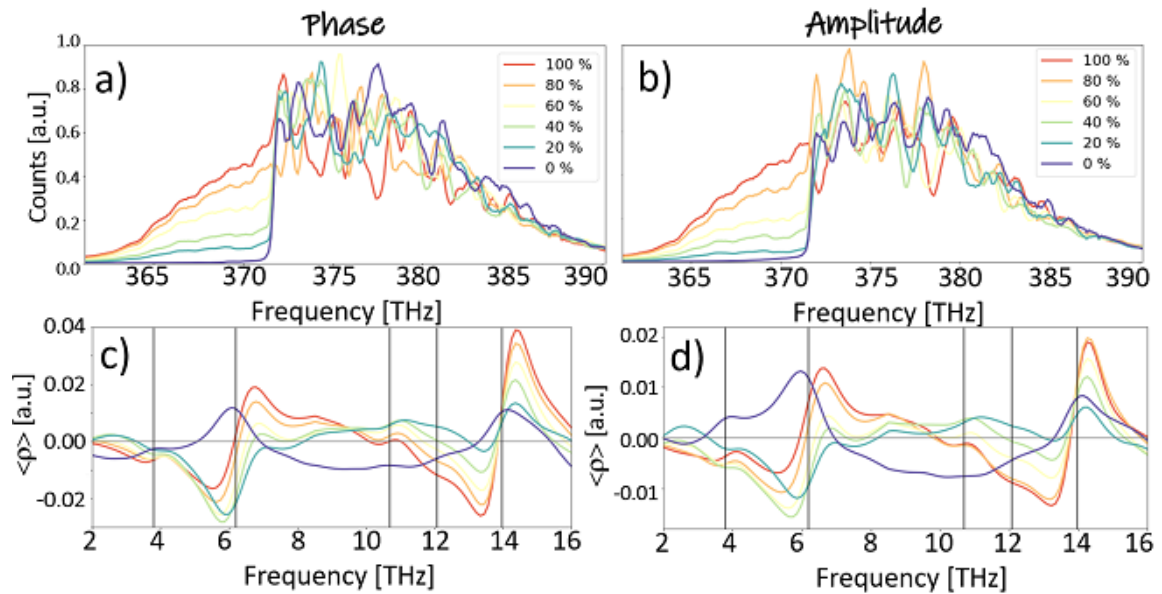


Figure 4.6: Measurements performed by gradually reducing the amplitude of the spectrally coherent side of the pulse spectrum. Spectra during the sweep applying a) phase or b) amplitude modulation. c–d) Correlation coefficient, as a function of frequency difference, calculated at every configuration by integration over the region where the signal is strongest. We only report data from the sample beam.

In Figure 4.6 we show selected spectra representing the mean amplitude variation, and the resulting correlation coefficient. It emerges that the signal shape is essentially the same up to the point where a field, if weak, is present in the low frequency side. When the intensity is completely blocked, the behaviour of the signal is different, as the intensity background is essentially zero across the region, and the presence of vibrational modes is revealed by Gaussian positive peaks.

In the configuration where we completely delete the amplitude of the coher-

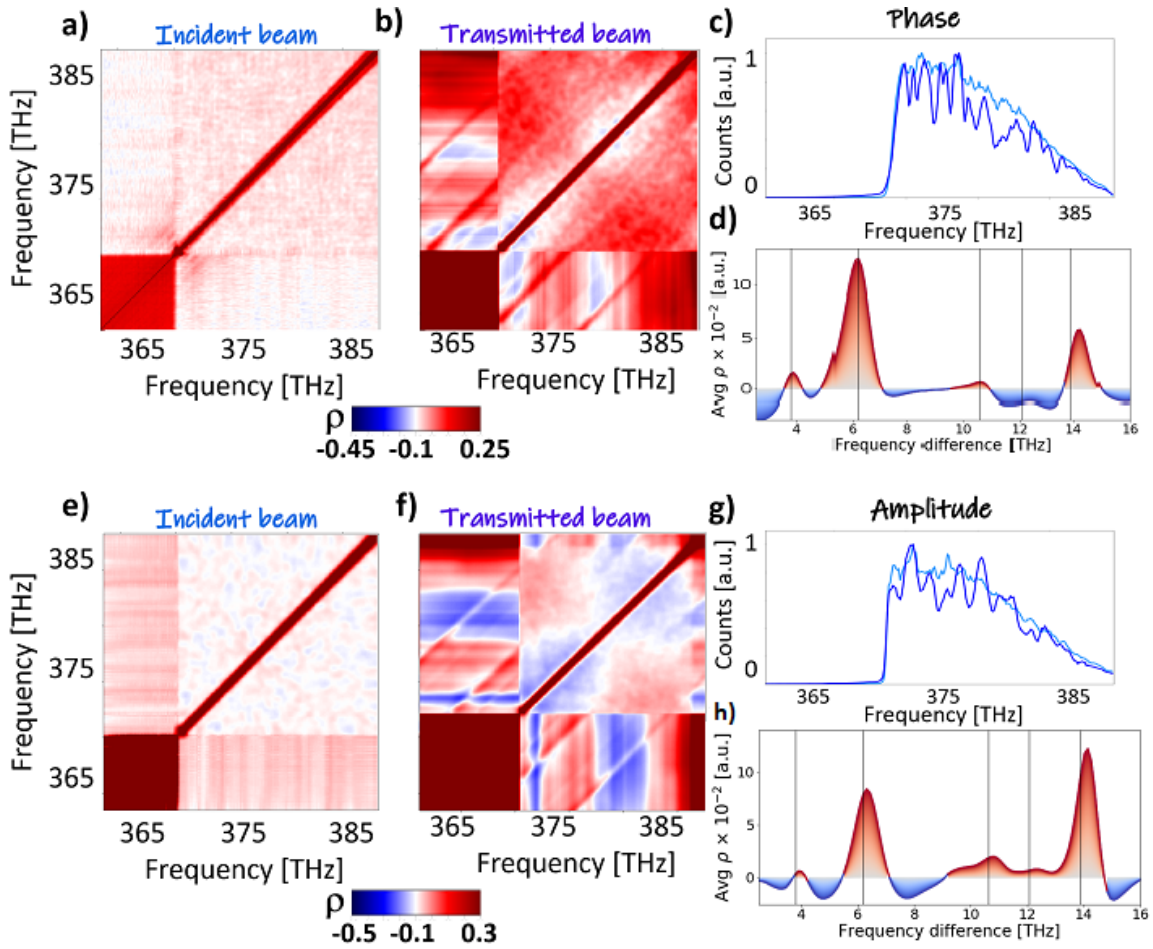


Figure 4.7: Measurements performed randomizing the spectral phase (a-d) or amplitude (e-h) along half of the bandwidth and deleting the other half of the spectrum. Example of reference (light blue) and transmitted (dark blue) spectra when randomizing the c) phase or g) amplitude. The respective low energy vibrational spectrum, retrieved by integrating the signal along the diagonal, is shown in panels d) and h), where the vibrations of α -quartz are indicated by vertical lines for comparison [41].

ent low frequency side and randomize the high frequency side of the spectrum, we explored the system's response. The result, together with a few selected spectra, is shown in Figure 4.7. We observe that the correlation coefficient has a similar behaviour, globally, than if we were retaining the whole spectrum, as the Pearson coefficient is not sensitive to the average value of the variables. The strongest signal is found in the blocks correlating a non randomized intensity to a randomized one. Moreover, the measurement with phase modulation delivers the same result as the one performed with amplitude modulation. Nonetheless, we notice that the asymmetry in the peak shape disappears within this con-

figuration, unlike when retaining the whole spectrum. We will discuss in more detail this difference in the next section. Finally we comment on the shape of the transmitted spectrum shown in Figure 4.7, which shows a "tail" of intensity where the average Raman amplitude should be zero (the expected behaviour is shown by the reference pulses). This is not only caused by a nonlinear broadening of the spectrum, it is also a sign of the presence of scattered intensity from the modulated spectrum.

4.2.2 ■ Lineshape analysis

The results obtained so far reveal how solid the Femtosecond Covariance Spectroscopy technique is: whatever modulation is applied on the pulses, the results are very consistent and the vibrational spectrum of the sample shows as offset diagonal correlation features in the statistical coefficient.

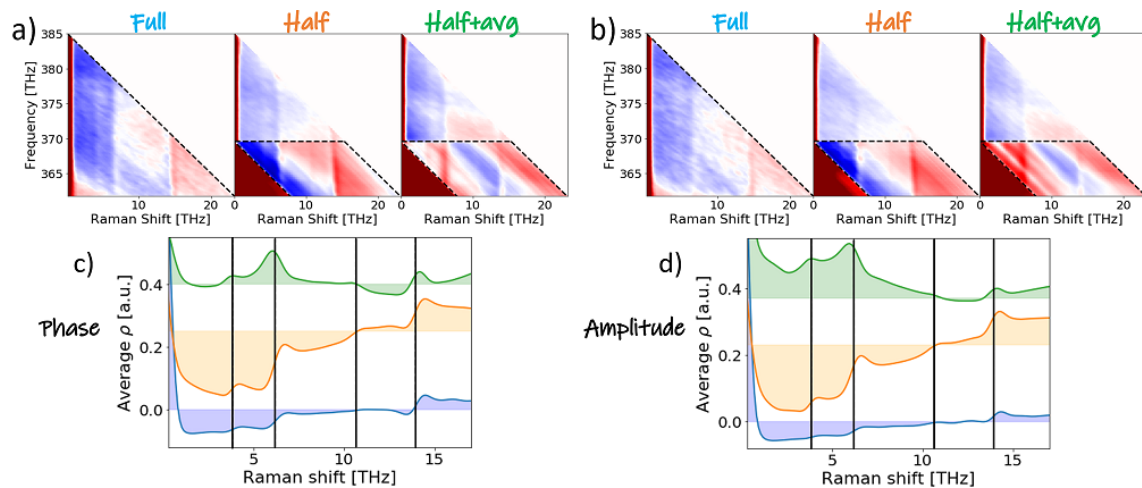


Figure 4.8: Rotated quadrants of the correlation coefficient maps of the sample beam calculated applying a) phase or b) amplitude modulation. The dashed lines delimit the region over which the integration is performed. The results of the integral are the curves shown in plots c) and d), stacked for the three types of measurements (the colour code is used to distinguish them), as a function of the phase difference. The vibrational modes of α -quartz are represented by black vertical lines [41].

The main difference we observed so far, among the measurements performed with the pulse shaper settings discussed above, is a changing signal lineshape. When the sample is probed by the whole spectrum, whether totally or half modulated, the signal is dispersive. When probing with half of the spec-

trum, the signal has a purely Gaussian peak shape. We compare the resulting correlation coefficients in Figure 4.8. We attribute this difference to the presence, in the first two cases, and absence in the latter, of a heterodyning field for the scattered radiation [14]. **These results prompted the description of the interaction as a self-heterodyned scattering process. In this, the covariance based approach finds a strength, as the signal beam does not need to be separate, geometrically, from the parent beams to be measured,** as the interaction is revealed through the statistical correlation imprinted in the spectrum by the interaction.

4.2.3 Average phase dependence

We tested the sample response by introducing with the pulse shaper a sharp edge at the centre of the average spectral phase. A noisy modulation was applied to the spectral amplitude in order to reveal the correlation signal.

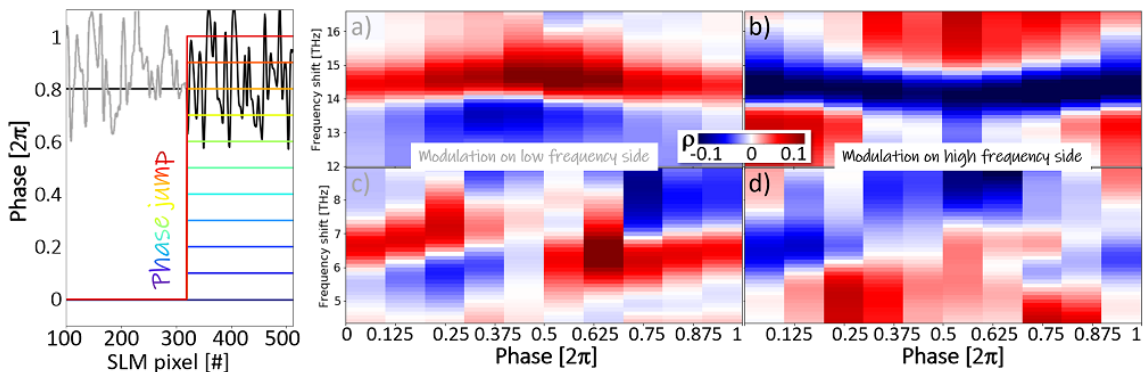


Figure 4.9: Correlation signal of the 14 THz phonon (a,b) and of the 6.2 THz phonon (c,d) as a function of the average spectral phase jump (x axis of the colour maps and colour lines in the left plot), when imparting an amplitude randomization on a-c) the low frequency side or on b-d) the high frequency side of the spectrum.

In Figure 4.9 we show the correlation signal for the 14 THz and the 6.2 THz phonons obtained varying the amplitude of the phase jump. The 14 THz phonons obtained varying the amplitude of the phase jump. The 14 THz phonon signal has a dispersive peak shape. The amplitude of its maxima and minima increases as the phase step reaches π , reverting to its initial shape when the phase jump reaches 2π . The phonon at 6.2 THz seems to follow a similar dynamics up to π , when the signal vanishes to reappear out of phase in the second half of the map.

4.3 ■ Cross correlation

Before discussing the few tests designed to investigate the dependence of the correlation signal on experimental parameters, we show the cross correlation ρ_c calculated on measurements using the whole spectrum, with a total or partial modulation. The result is shown in Figure 4.10.

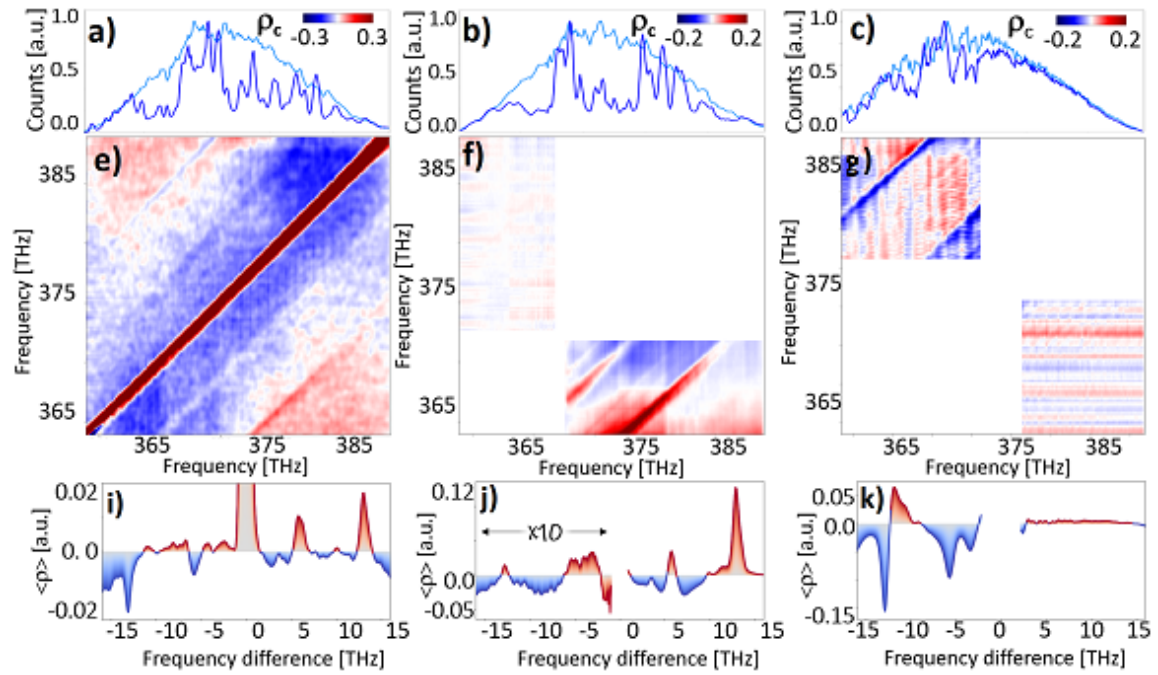


Figure 4.10: Cross correlation coefficient ρ_c computed on the transmitted spectra of single pulse measurements. Example reference (light blue) and transmitted spectra (dark blue) obtained when modulating a) the whole bandwidth, b) the higher or c) lower half of it. The corresponding ρ_c is shown in e-g) respectively, along with its integral along the diagonal in i-k). In f) and g), and in i-k), the background was flattened for the sake of clarity.

As expected, the cross correlation is not symmetric on the two sides of the map. When the spectrum is fully modulated, the signal on the two sides of the map is comparably strong, and it changes sign. We notice that the same sign behaviour is retained when a portion of the spectrum is not modulated. Moreover, in this scenario, the signal from light scattered towards the spectrally coherent side seems to be enhanced. Let us turn to the measurements performed modulating the high frequency side. The signal is clearly visible in the bottom right panel, and is positive. The opposite block reveals a tiny signal.

When the modulation is applied on the low frequency side of the spectrum, the measurement results in a strong negative signal in the upper left block, with a negative sign as in the correlation coefficient of the fully modulated spectra. We notice, as well, that as a result of this calculation, the shape of the signal is not so clearly dispersive as from ρ .

4.4 Selected peaks randomization

In this Section we describe experiments conceived in order to understand the role of the stochasticity in the process taking place in the sample, and eventually if a proper combination of settings enables an amplification of the signal.

4.4.1 Randomization of a single peak

The first measurement of the set is performed by randomizing a **single spectral component at a fixed position** in the spectrum.

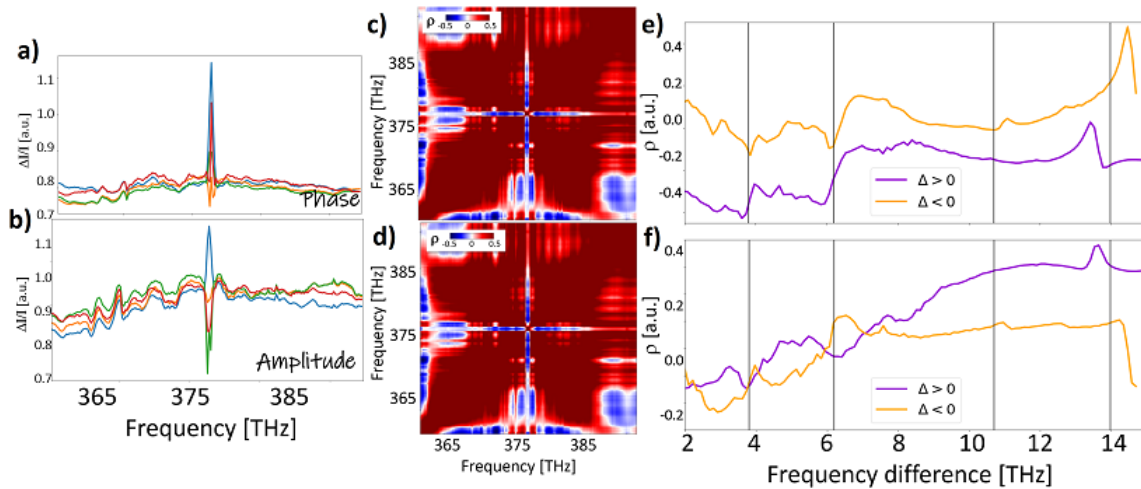


Figure 4.11: Measurements performed with a single peak randomized, at a fixed position in the spectrum (377 THz). Ratio between a few selected transmitted spectra and the corresponding reference spectrum, when applying a) phase or b) amplitude modulation. c-d) Correlation coefficients of the sample beam in the two aforementioned noise configurations. The vertical lines at 377 THz are shown in e) and f), as a function of the absolute value of the frequency difference (the actual sign of the difference Δ , related to the position of the curve in the correlation coefficient map, is indicated by the colour of the lines).

In Figure 4.11 we show the result of this measurement for a phase or amplitude randomization. The correlation coefficient is dominated by the coherence of the non modulated spectrum. Along lines at the position of the modulated component, the coherence has a different structure. Cuts of the map along this direction are shown in panel b) of the same Figure, as a function of frequency difference. We find that for both positive and negative frequency differences there are dispersive signal features at the vibrational modes position. These measurements seem to reproduce the results of Section 4.2, only on a single line.

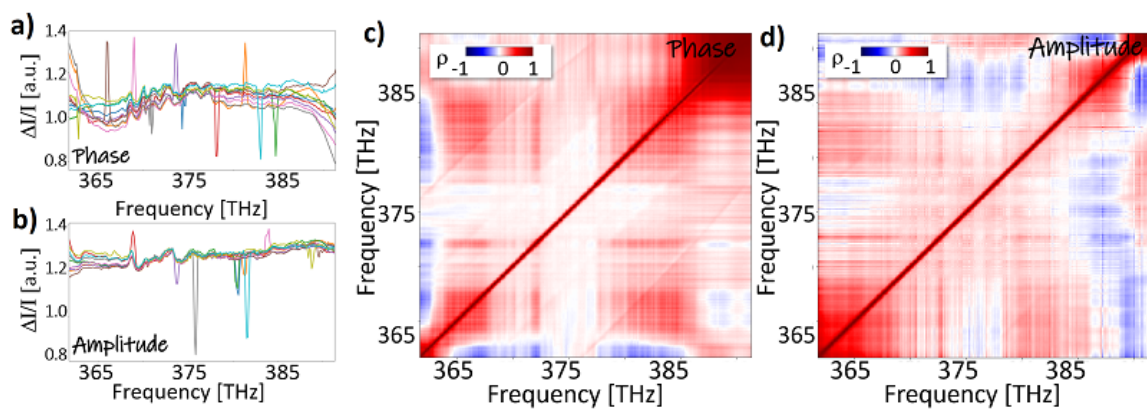


Figure 4.12: Measurement performed with a single modulated peak at a random position within the spectrum. a–b) Plots of the ratio between a few selected transmitted spectra and the corresponding reference spectrum. Correlation coefficient of the sample beam when applying c) phase or d) amplitude modulation.

We repeated this experiment by **changing the position** of the modulated peak within the spectrum, at each shot. The result is shown in Figure 4.12. The correlation map reveals faint lines at frequency distance from the diagonal 3.8 THz and 14 THz, on top of a background from which they are almost indistinguishable. We conclude that this measurement reproduces with lower efficiency the result obtained by modulating half of the spectrum at once (see Section 4.2).

4.4.2 ■ Randomization of a pair of peaks

On the basis of the previous tests, we performed an experiment **fixing the position of a modulated peak** and **changing the position of the second peak** randomly at every shot.

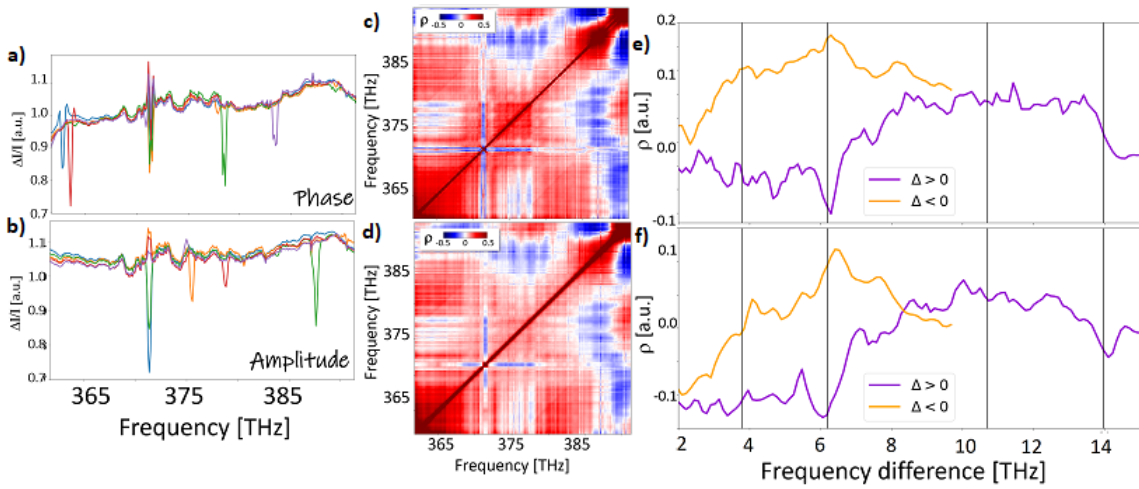


Figure 4.13: Measurement performed by modulating two peaks, one at a fixed position (372 THz) and one moving randomly across the spectrum. Ratio between a few selected transmitted spectra and the corresponding reference spectrum, when applying a) phase or b) amplitude modulation. Correlation coefficients of the sample beam in the two aforementioned noise configurations (c), d)). The vertical lines at 372 THz are shown in e) and f), as a function of the absolute value of the frequency difference (the actual sign of the difference Δ , related to the position of the curve in the correlation coefficient map, is indicated by the colour of the lines).

The result is shown in Figure 4.13. This map looks like a combination of the maps of Figure 4.11 and Figure 4.12. Along the profile of the fixed modulated peak we recognize the signal from the 3.8 THz, 6.2 THz and 14 THz phonons. At a closer inspection, these peaks are visible throughout the map.

Finally we tested the technique by **modulating two peaks** in the spectrum, with a **fixed distance** for all repetitions in a single measurement, scanning such a distance. To show the full set of measurements, an example of which is shown in panel a) of Figure 4.14, we stack the correlation profile extracted along the moving peak as a function of the frequency distance between the peaks. The resulting image, shown in panel b) of Figure 4.14, is a colour map whose axes represent a frequency difference (on the x axis the distance within the probe spectrum, on the y axis the distance between the modulated peaks) and the colour scale the value of the correlation. We find correlation features at the position of the vibrational modes, and a diagonal line, whose value is close to

zero, representing the vanishing correlation between the randomized peaks. The plot in panel b) seems to reproduce the sample correlation coefficient of panels b) and f) of Figure 5.9.

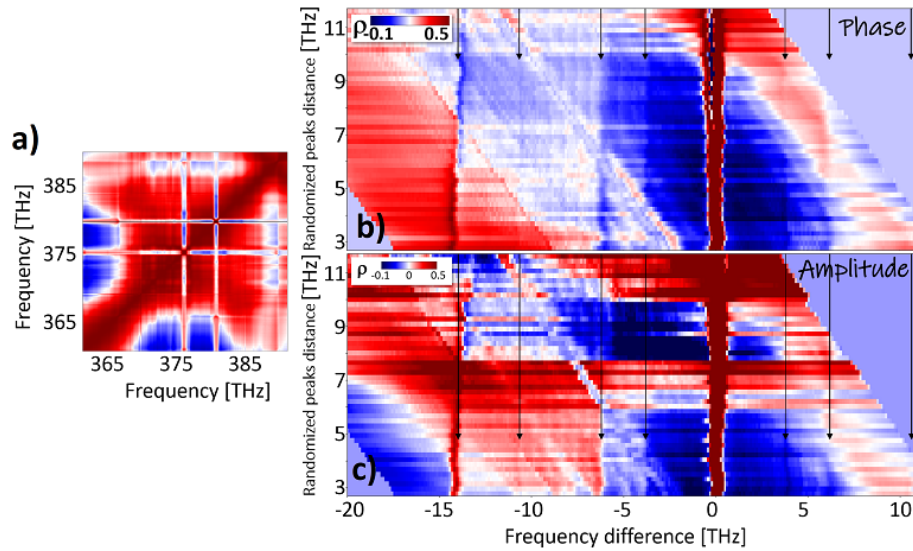


Figure 4.14: Set of measurements performed modulating two peaks within the spectrum of each pulse, with fixed distance. a) Correlation coefficient for a peak distance of 5 THz. b–c) Profiles extracted at the fixed peak position (377 THz), which coincides with the profile at the moving peak position, as a function of the peak distance and the frequency difference within the spectrum.

We conclude that there is no enhancement of the vibrational signal when the distance between the moving peaks is close or equal to the frequency of a vibrational mode. Moreover, the results of this Section show that the correlation coefficient is only sensitive to the statistical properties of the intensity pairs which is fed, therefore there is no sensitivity to the global properties of the pulse. This scenario is compatible with the interpretation of the experiment given above: the process takes place no matter what the stochastic properties of the pulses are, and the randomization of the latter only serves to enable the detection of the sample induced correlation.

4.5 ■ Fluence dependence

This final Section of the Chapter dedicated to single pulse measurement deals with a set of measurements performed increasing gradually the energy per

pulse, in order to understand to which extent the FCS technique is able to recover the order of nonlinearity of the interaction process. The usual approach is to detect the changes in a nonlinear signal as a function of the intensity of the incident fields. Given that the correlation coefficient under consideration is adimensional and normalized, and taking into account the self-heterodyned nature of the experiment, it is not straightforward to extract a dependence of the Pearson coefficient values on the intensity of the incident pulses.

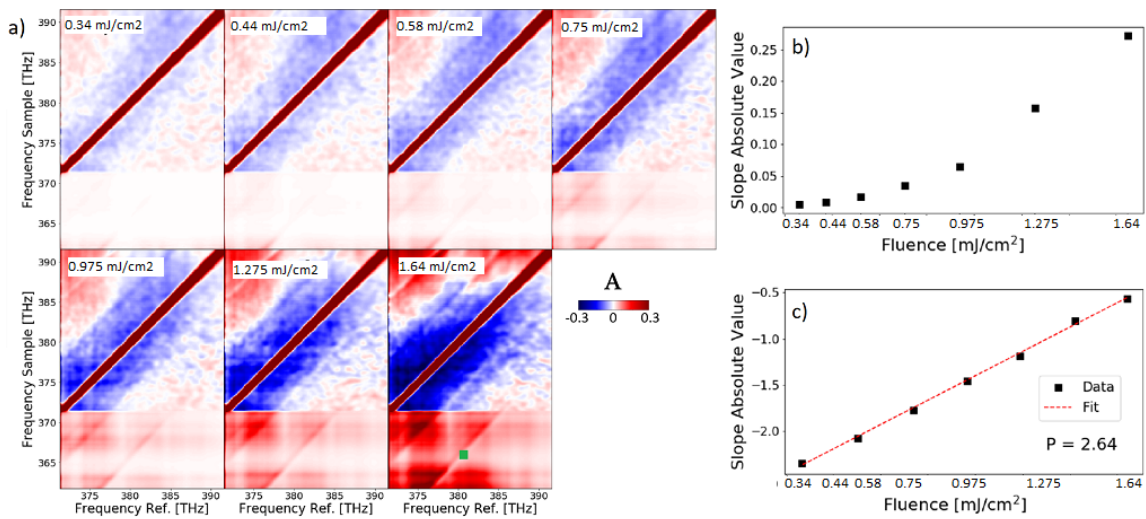


Figure 4.15: a) Slope map for each input fluence. Slope value (at frequency coordinates indicated by the green square) as a function of the fluence, in b) linear and c) logarithmic scale (the red line is a linear fit).

We therefore envisioned a different method to study the interaction non-linearity, which makes use of the measured reference intensity, as the latter serves as a benchmark of the beam properties before the interaction. Therefore we will study the cross correlation between the transmitted intensity I^T and the incident intensity I^R . We focus on the proportionality factor A existing between the variables when they are correlated, that is to say when a relationship holds in the form $I^T = A(I^R - I_0^R)$. As both I^R and I^T are measured intensities, the order of the process m is enclosed in A . Being the interaction under consideration of the third order, we expect A to be quadratically dependent on the intensity of the input beam, which we vary in the experiment by appropriately filtering the laser beam. We compute A applying a fitting procedure to all the data pairs, and end up with a map of the proportionality coefficient A for each input fluence (see Figure 4.15). We model the behaviour of A for each intensity

pair as

$$A = C(I^R - I_0^R)^P \quad (4.1)$$

where I^R is the input intensity. We expect I_0^R to be zero as the process is stimulated, and $P = m - 1$ (as one intensity factor is the dependent variable of the relation for I^T).

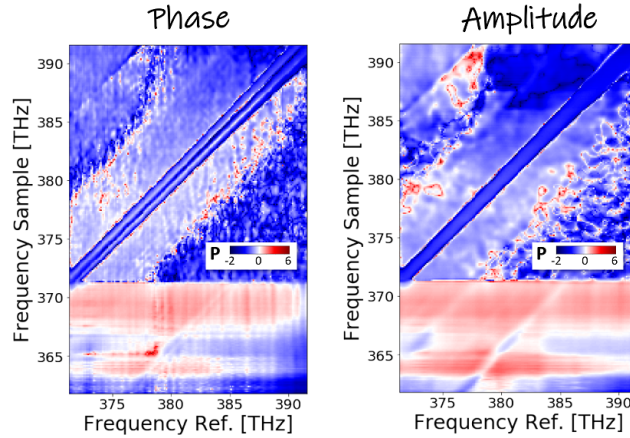


Figure 4.16: Maps of the exponent extracted by fitting each slope values as a function of the fluence with Equation 4.1.

By taking the logarithm of Equation 4.1 and performing a linear fit of each point of the A maps, we extract the value of P . The results for both spectral phase and amplitude modulations are shown in Figure 4.16. $P \approx 2$ where the intensity values are correlated by the interaction, while $P \neq 2$ elsewhere.

In this chapter we appreciated how straightforward it is to extract information on the vibrational modes of α -quartz within the FCS technique. Applying a stochastic modulation along the whole spectral bandwidth, on the phase or amplitude of a pulse, we extracted, from the correlation coefficient of the transmitted beam, the sample low energy vibrational spectrum. Moreover, applying a modulation along half of the spectrum, we found a sharper correlation signal. As a matter of fact the signal, in such an experiment, is self-heterodyned, which means that the scattered field adds to the non interacting field, from which is indistinguishable, as the two spectrally and spatially overlap. The signal retrieved with the specific correlation coefficient ρ , therefore, depends on the modulation of a single component of the two fed to ρ itself, consistently

with what we obtained modulating one peak or a pair of peaks within the spectrum. This was further confirmed by the signal shape in the cross correlation coefficient ρ_c . This suggests to investigate what information can be extracted using tailored correlation coefficients based upon, for instance, multiple body correlations.

To further assess the capabilities of the covariance based acquisition, we applied it to a sample prepared in a coherent state whose population evolution can be tracked in time. To excite the sample an intense pump pulse must be employed, which imparts a defined phase to the excitations. An experiment performed with two pulses allows, moreover, to combine their polarizations and select the response of phonons with different symmetry, which could not be distinguished in the experiments discussed so far because both polarizations belong to the same pulse and are randomized simultaneously. The femtosecond covariance technique used to probe a coherently excited sample is the subject of the next Chapter.

5 ■ Time resolved experiments

We introduce in this Chapter double pulse experiments which constitute the straightforward extension to the femtosecond covariance transmission measurements in the framework of ultrafast spectroscopy. First, we study with spectrally coherent probe pulses the vibrations of the sample, excited in phase by the pump. These results were published, together with the quantum model described in Section 2.2, in [15]. Then, we move on to double pulse experiments with a coherent and a randomized probe, performed applying the setup variations described in Chapter 3.

The experiments employing spectrally coherent pulses at the laser wavelength are described in Section 5.1. They employ pump pulses with fluence 2 mJ/cm^2 and probe with fluence 0.3 mJ/cm^2 (exception made for the measurements of Section 5.1.2, where this parameter was systematically changed). These values were chosen in order to ensure the absence of nonlinear effects induced by the probe. We fully characterize the signal dependence on the experimental parameters and validate the quantum model of Chapter 2 for Impulsive Stimulated Raman Scattering (ISRS). The following Section 5.2 is dedicated to a femtosecond covariance based detection applied to the pump excited sample. This set of measurements was performed using a frequency converted pump (by means of the double stage optical parametric amplifier described in Section 3.2) at $1.29 \text{ }\mu\text{m}$ and a randomized probe at the laser wavelength (800 nm). The measurements were carried out using a pump fluence of roughly 2 mJ/cm^2 and a probe fluence of 0.03 mJ/cm^2 (unless otherwise stated).

5.1 ■ Pump probe experiments

The double pulse experiments on α -quartz using coherent pulses are displayed as colour maps. The maps show the relative normalized transmitted intensity $\Delta I/I$ calculated using both the sample channel I^S and the reference one I^R as

$$\begin{aligned} \frac{\langle \Delta I \rangle}{\langle I \rangle}(\omega, \Delta t) &= \left(\langle \frac{I^S}{I^R} \rangle(\omega, \Delta t) - \langle \frac{I^S}{I^R} \rangle(\omega)_{\Delta t < 0} \right) / \langle \frac{I^S}{I^R} \rangle(\omega)_{\Delta t < 0} = \\ &\approx \langle \frac{I^S}{I^R} \rangle(\omega, \Delta t) - \langle \frac{I^S}{I^R} \rangle(\omega)_{\Delta t < 0} \end{aligned} \quad (5.1)$$

as the denominator in the first line of Equation 5.1 is $\langle I^S/I^R \rangle(\omega)_{\Delta t < 0} \approx 1$.

In practice, we divide every transmitted single shot spectrum by the corresponding reference single shot spectrum, to account for instantaneous fluctuations of the source, and average such ratio over the repetitions acquired at a fixed time delay. To this quantity, we subtract the ratio averaged over a finite interval of negative time delays, representing the thermal equilibrium value of the signal, to account for slower source intensity fluctuations. The evolution of the function $\langle \Delta I \rangle / \langle I \rangle(\omega, \Delta t)$, therefore, represents the dynamical percent variation of the sample transmittivity. In the following we will indicate $\langle \Delta I \rangle / \langle I \rangle(\omega, \Delta t)$ by $\Delta I/I$.

In Figure 5.1 we show a time and frequency resolved experiment on α -quartz. The vertical axis indicates the probe spectral content, the horizontal axis the time delay Δt , while the colour plot the values of $\Delta I/I$. The spectrum is centered at 377 THz (795 nm), and regions below ≈ 355 THz and above ≈ 395 THz are zero as there is no spectral intensity at the corresponding areas of the detector. At negative time delays the ratio $\Delta I/I$ is zero both outside and within the probe bandwidth, while at the pump probe overlap it arises sharply and starts oscillating. This behaviour is expected for a transparent sample in which coherent vibrational modes have been excited. As calculated within the ISRS quantum model described in Section 2.2, and displayed in Figure 2.6, the probe spectrum undergoes shifts towards the low or high frequency side, alternatively, because of the energy exchange of the probe pulse with the pump excited coherent phonons of the sample. Within an intuitive picture, that sketches the interaction between the probe and the material as a coupling between the electric field of the former and the instantaneous polarization of the latter, we find that the effective energy exchange depends on the relative direction of the

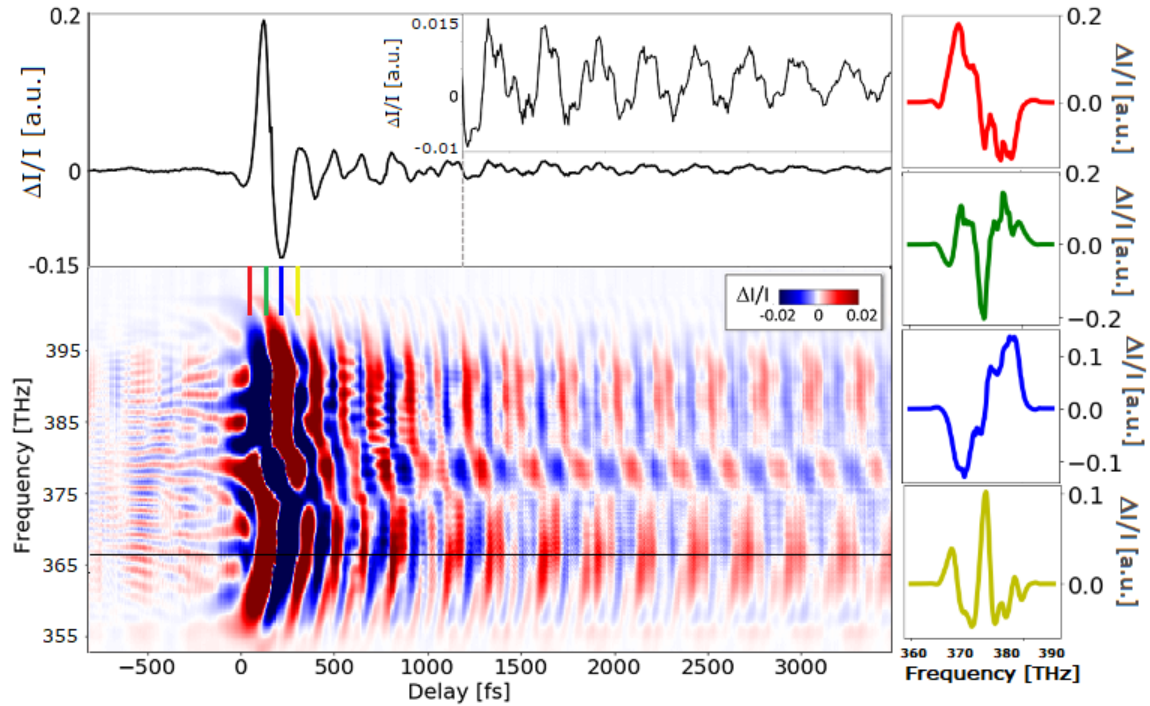


Figure 5.1: Pump probe experiment on α -quartz using spectrally coherent pump and probe pulses. The colour map shows the frequency and time resolved $\Delta I/I$ signal. The cut on top is the time dependent signal at a probe frequency 367 THz (the inset represents a zoom on the last portion of the curve). The right panel represents cuts of the map along the probe spectrum, at time delays indicated by the accordingly colored lines on top of the colour plot. a) and c) are points of maximum inelastic light scattering shift towards the low and high frequency side of the spectrum, respectively. b) and d) are points of maximum nonlinear refractive index modulation, resulting in a minimum and maximum of the dynamical transmittivity, respectively.

probe electric field and the phonon momentum, which oscillates in time with the phonon frequency. The time oscillations of the experimental response can actually be understood by noting that, at a fixed time delay, the response is structured along the probe frequency axis. To view this response, slices of the $\Delta I/I$ map along the frequency axis and at subsequent time delays are shown on the right. In a) and c) we recognize the inelastic light scattering (ILS) frequency shifts, towards the low and high frequency side, respectively.

In addition to ILS, prevailing on the sides of the spectrum, we notice the presence of a modulation at its centre, where the net frequency shift is zero. The dynamics of such a modulation is in agreement with the ILS shifts, with a $\pi/2$

phase difference. We recall that, within the quantum model, we calculated the effect of the coherent phonon excitation on the material's refractive index, whose outcome on the evolution of $\Delta I/I$ is shown in Figure 2.5. As a consequence of this nonlinear refractive index modulation (NRM), $\Delta I/I$ is expected to be proportional to the coherent vibrational amplitude. Moreover, this effect does not result in any energy exchanges between the sample and the probe pulses, consequently it is uniform along the probe spectrum. The slices of the colour map b) and d), shown on the right of Figure 5.1, taken at the nodes of the inelastic light shift, show peaks at the centre of the spectrum, in agreement with the effect of NRM. To summarize, if we follow the evolution of the differential signal in time, we find a red shift, a negative peak, a blue shift, a positive peak, and the cycle repeats (cf. Figure 2.7). Switching back to the time delay axis, at each frequency component along the probe bandwidth we expect to witness oscillations of the signal with the same Fourier components, but a different phase.

By looking at the time decay of the signal, we note the presence of many vibrational modes: a slow vibrational mode dominating the signal at large time delays, and a faster signal prevailing closer to the overlap. A very fast modulation is present all along and is clearly visible at large delays. We expect these to be the three strongest low energy vibrational modes of α -quartz at 3.8 THz, 6.2 THz and 14 THz, respectively. To extract quantitative informations on the amplitude of these modes, their relative phase and their lifetime, a **Fourier analysis** in the frequency domain is necessary.

We start by performing the Fast Fourier Transform (FFT) [64] of $\Delta I/I$ along the time delay axis. The absolute value of the FFT is shown in Figure 5.2 as a function of the Fourier component frequency and of the probe frequency, calculated on the measurement shown in Figure 5.1. We identify three regions along the probe bandwidth which give rise to a higher FFT absolute value. The external regions represent the points where the spectral shift due to the inelastic light scattering is maximum, and the central region is where the nonlinear refractive index modulation is strongest. The frequency content in these regions of the probe spectrum is the same, but peaks due to ILS have a relative π shift, and each of them is $\pi/2$ shifted from the NRM peaks. We plot, in the

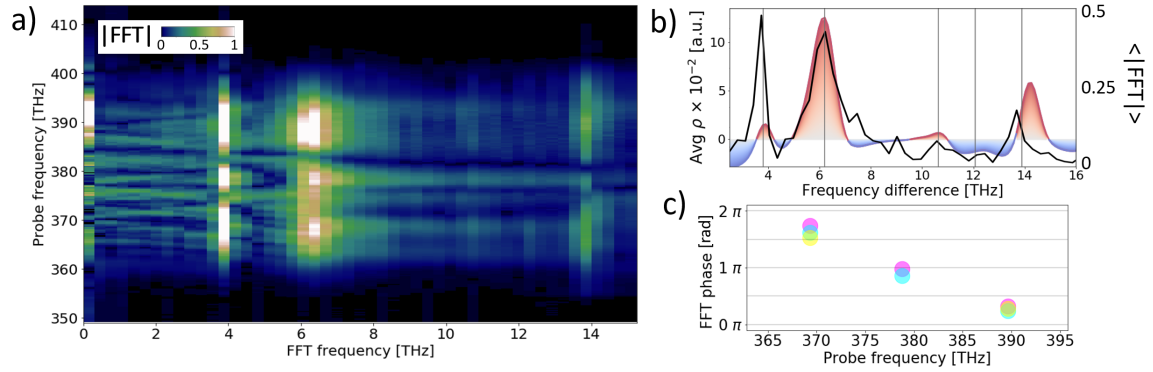


Figure 5.2: a) Absolute value of the Fast Fourier Transform (FFT) along the delay axis of the average signal shown in Figure 5.1. b) Absolute value of the FFT averaged along the probe spectrum (black curve), compared to the vibrational spectrum obtained from the correlation coefficient of Figure 4.7. c) Value of the FFT phase at the maxima of the three strongest Fourier components, as a function of the probe spectrum.

same Figure, the FFT amplitude averaged along the probe spectrum, together with the central frequency of the vibrational modes as reported in the literature (grey vertical lines). Moreover, we compare these data to the spectrum retrieved with the FCS technique when modulating half of the spectrum and deleting its low energy portion (reported in Figure 4.7). There is good agreement between the two spectra. We notice a difference in the position of the 14 THz peak from the correlation, possibly due to its dispersive lineshape, and an apparent difference in the amplitude of the peak at 3.8 THz.

It is worth to comment on the **high frequency modulation** visible along the spectrum of the measurement of Figure 5.1, which is particularly visible close to the overlap at negative time delays. If we follow this modulation further from the overlap, both at positive and negative time delays, we notice that its frequency along the spectrum increases. Because of the proportionality of the frequency of this effect to the time delay, we believe their appearance is intimately related to the coherent sum of the probe field with a residual scattered field of the pump along the probe propagation direction. Their appearance could be related to cross-phase modulation (XPM) [65–67], a nonlinear modification of the material refractive index due to the high intensity of the pump beam, which can affect the temporal, spectral, and even spatial properties of a co-propagating pulse.

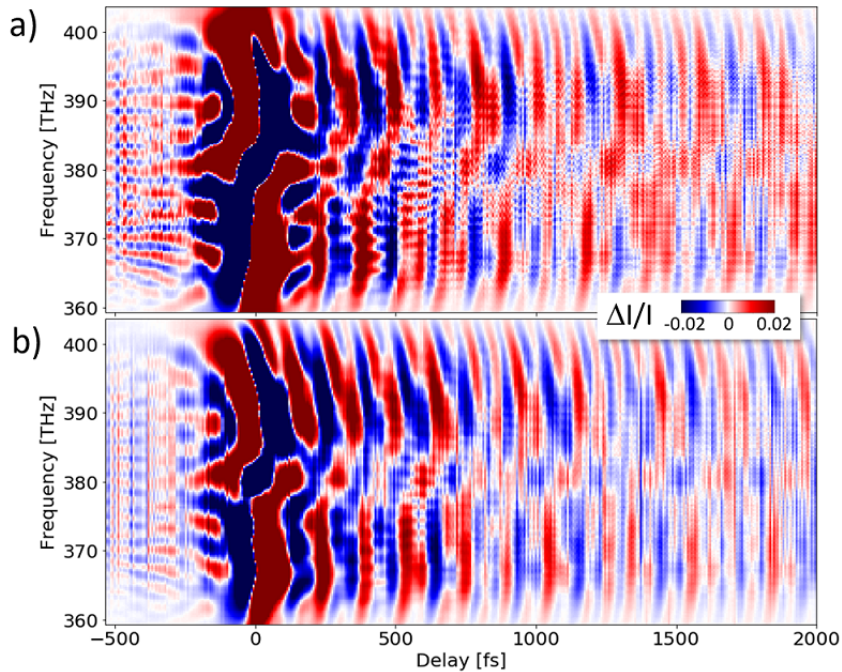


Figure 5.3: Double pulse experiment on α -quartz using spectrally coherent pump and probe pulses, with a) parallel polarization or b) orthogonal polarization.

In Figure 5.3 we show two measurements on α -quartz performed in the same fluence conditions, with parallel or orthogonal relative pump probe polarization. The high frequency modulation is more pronounced when the polarizations are parallel. They do not disappear when a pump output from the DS-OPA is used, therefore when pump and probe do not have the same spectral content, consistently with a nonlinear phenomenon dependent on the pump intensity [68, 69].

5.1.1 ■ Polarization dependence

A further possibility provided by the double pulse experiment is the separation of the signal arising from A - and E -symmetry vibrational modes. As described in Section 2.2.3, the matrix representations of the modes combine to form the electric susceptibility of the material, determining which polarization components are involved in the interaction. From the experimental perspective, properly combining the field polarizations allows to disentangle the different contributions to the susceptibility, in other words the response related to phonons with a specific symmetry. In the case of α -quartz, we describe the

frequency ω_j , time t and pump-probe angle θ dependent response in Equations 2.113 and 2.114. The expected signal at $\theta = 0, \pi/8, \pi/4, 3\pi/8, \pi/2$ is calculated in Equations 2.115 and 2.117, which are reported here for the sake of clarity. When the analyzer is parallel to the probe, the signal reads

$$\begin{aligned} \left\langle \Delta I_{xj}^{PR} \left(\tau, \theta = 0, \frac{\pi}{2} \right) \right\rangle_t &\propto \left[K \alpha^2 \Delta \alpha_{j, \Omega_A}^{PR} \cos(\Omega_A t) \pm c^2 \Delta \alpha_{j, \Omega_E}^{PR} \cos(\Omega_E t) \right] \\ \left\langle \Delta I_{xj}^{PR} \left(\tau, \theta = \frac{\pi}{8}, \frac{3\pi}{8} \right) \right\rangle_t &\propto \left[K \alpha^2 \Delta \alpha_{j, \Omega_A}^{PR} \cos(\Omega_A t) \pm \frac{\sqrt{2}}{2} c^2 \Delta \alpha_{j, \Omega_E}^{PR} \cos(\Omega_E t) \right] \\ \left\langle \Delta I_{xj}^{PR} \left(\tau, \theta = \frac{\pi}{4} \right) \right\rangle_t &\propto \left[\alpha^2 \Delta \alpha_{j, \Omega_A}^{PR} \cos(\Omega_A t) \right] \end{aligned} \quad (5.2)$$

while when the analyzer is orthogonal to the probe

$$\begin{aligned} \left\langle \Delta I_{yj}^{PR} \left(\tau, \theta = 0, \frac{\pi}{2} \right) \right\rangle_t &= 0 \\ \left\langle \Delta I_{yj}^{PR} \left(\tau, \theta = \frac{\pi}{8}, \frac{3\pi}{8} \right) \right\rangle_t &\propto \frac{\sqrt{2}}{2} c^2 \Sigma \alpha_{j, \Omega_E}^{PR} \sin(\Omega_E t) \\ \left\langle \Delta I_{yj}^{PR} \left(\tau, \theta = \frac{\pi}{4} \right) \right\rangle_t &\propto c^2 \Sigma \alpha_{j, \Omega_E}^{PR} \sin(\Omega_E t) \end{aligned} \quad (5.3)$$

The coefficients $\Delta \alpha_{j, \Omega}^{PR}$ and $\Sigma \alpha_{j, \Omega}^{PR}$ are reported in Equations 2.116 and 2.118, respectively.

The set of time and frequency resolved measurements performed by varying the angle θ is shown in Figure 5.4. The left (right) column shows the measurements obtained by selecting with an analyzer E^{POL} the polarization parallel (orthogonal) to the probe field E^{PR} . In Figure 5.5, we show the FFT amplitude calculated at 367 THz and 377 THz, respectively, on points of the probe spectrum where the ILS and NRM effects are more pronounced, for both parallel and orthogonal polarization to the probe.

When $E^{POL} \parallel E^{PR}$, the main vibrational components are present in the response, and their amplitude is non zero where the spectral shift is maximum, as can be seen in panel a) of Figure 5.5. By changing θ towards $\pi/4$, the contribution to the response associated to the E phonons gradually disappears. Within this geometry we should observe only contributions to the signal arising from the inelastic light scattering, therefore there should be no oscillations at the peak of the probe spectrum (see panel b) of Figure 5.5). When $E^{POL} \perp E^{PR}$ the signal is given, as expected, by the nonlinear refractive index modulation, and oscillates with the E mode frequency, as confirmed by the FFT shown in panel c) of Figure 5.5. As θ varies, the amplitude of the FFT associated to such mode increases, reaching a maximum at $\pi/4$. We notice that an imperfect experi-

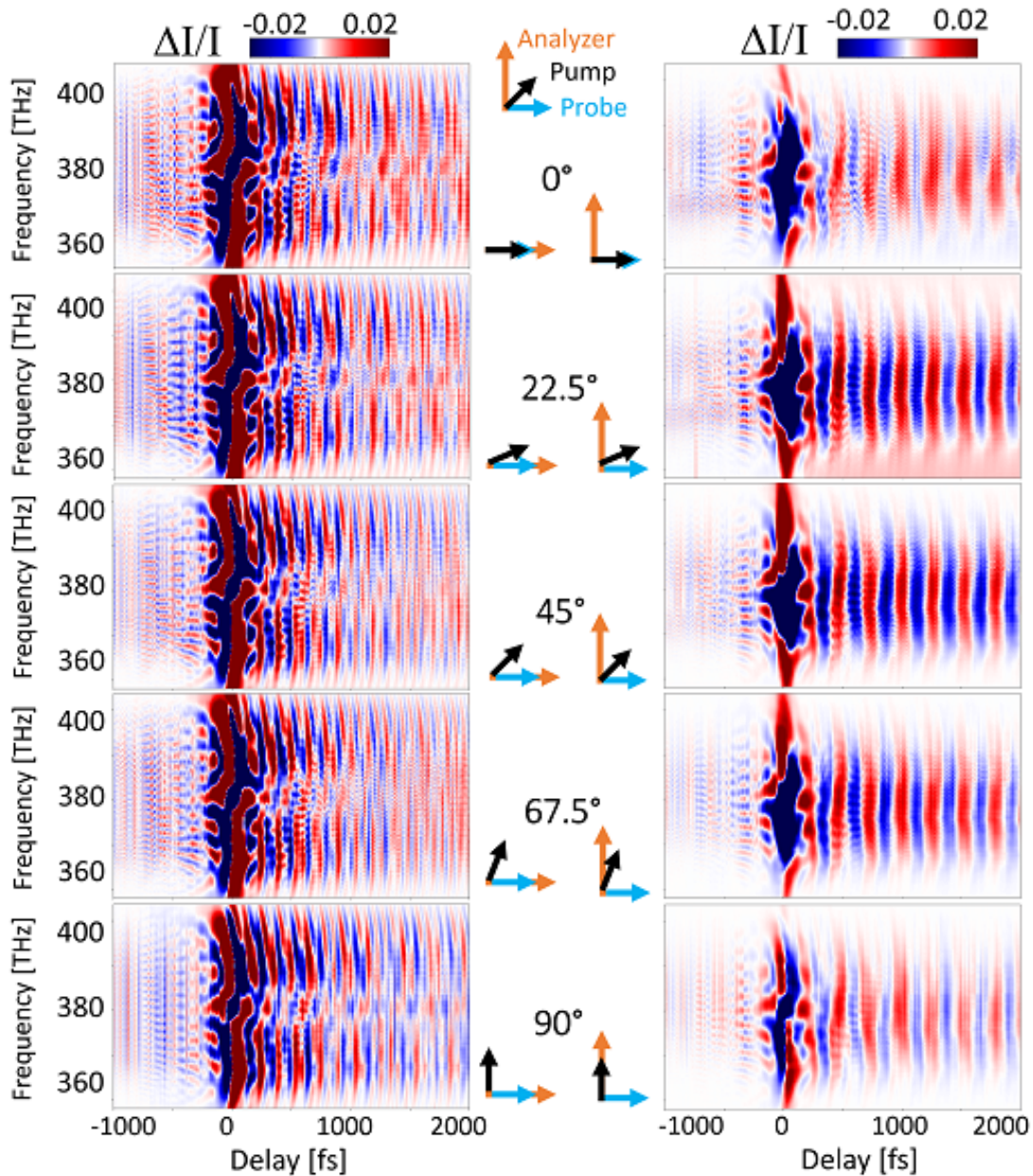


Figure 5.4: Double pulse measurements performed using linearly polarized pulses, changing the pump-probe polarization angle and measuring the parallel (left column) or orthogonal (right column) component of the transmitted probe. The polarization configurations are reported in the insets.

mental alignment determines the presence of faint frequency components on the sides of the probe spectrum, at frequencies of the A modes. Moreover, the signal is not perfectly extinguished as it should be for $\theta = 0, \pi/2$. The reason for these discrepancies with the theoretical model lies in the fact that the crystal equilibrium optical activity¹ was not taken into account in the measurements.

¹The optical activity is the ability of a crystal to rotate the linear polarization of a transmitted

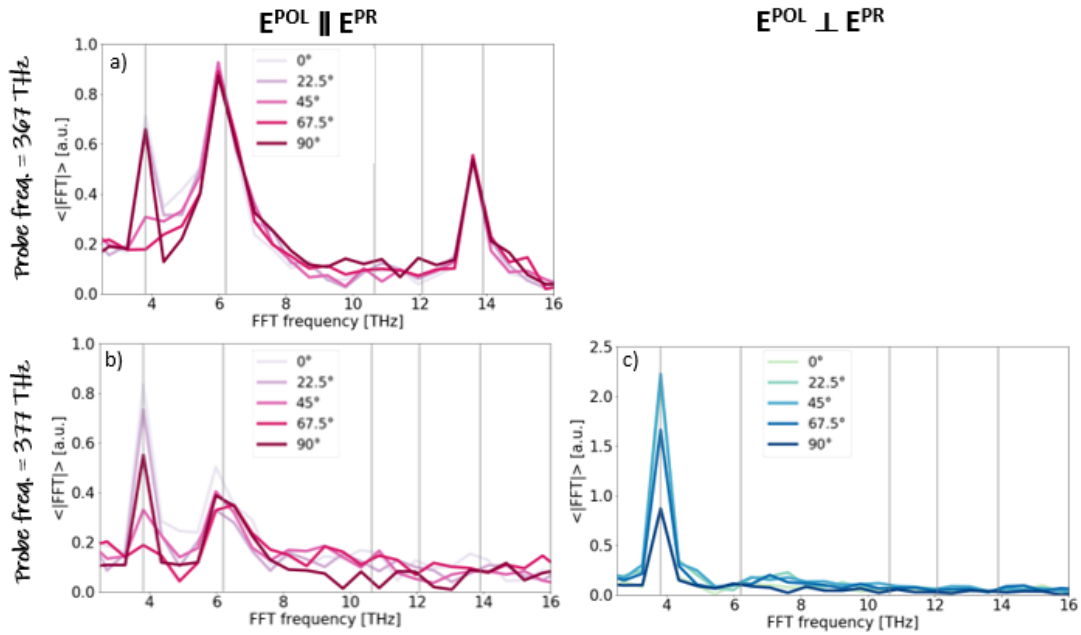


Figure 5.5: Absolute value of the Fast Fourier Transform (FFT) for parallel (a,b) and orthogonal (c) probe-analyzer angles, changing the pump-probe polarization angle. The FFT is calculated at probe frequency a) 367 THz and b,c) 377 THz.

Therefore the pump and analyzer rotations should have been adjusted to this offset, in the present case roughly 8° (calculated for a crystal thickness of 1 mm).

5.1.2 Pulse fluence dependence

The nonlinear order of the interaction was tested by changing the pump energy and measuring the transmitted intensity. The probe fluence was 0.7 mJ/cm^2 .

In Figure 5.6 we plot the pump probe traces obtained by changing the pump pulse energy, as a function of the time delay and at a fixed probe frequency 367 THz and 377 THz, respectively on the maximum of the ILS and of the NRM effect. The signal is in both cases directly proportional to the fluence. The maxima of the 367 THz signal and minima of the 377 THz signal are shown on the right as a function of the fluence. A linear dependence of the ILS maxima and the NRM minima is observed, as expected (see Equation 2.112). In fact the fluence is proportional to the intensity, which is in turn proportional to the squared absolute value of the electric field involved in the process.

light beam, with a magnitude proportional to the crystal thickness.

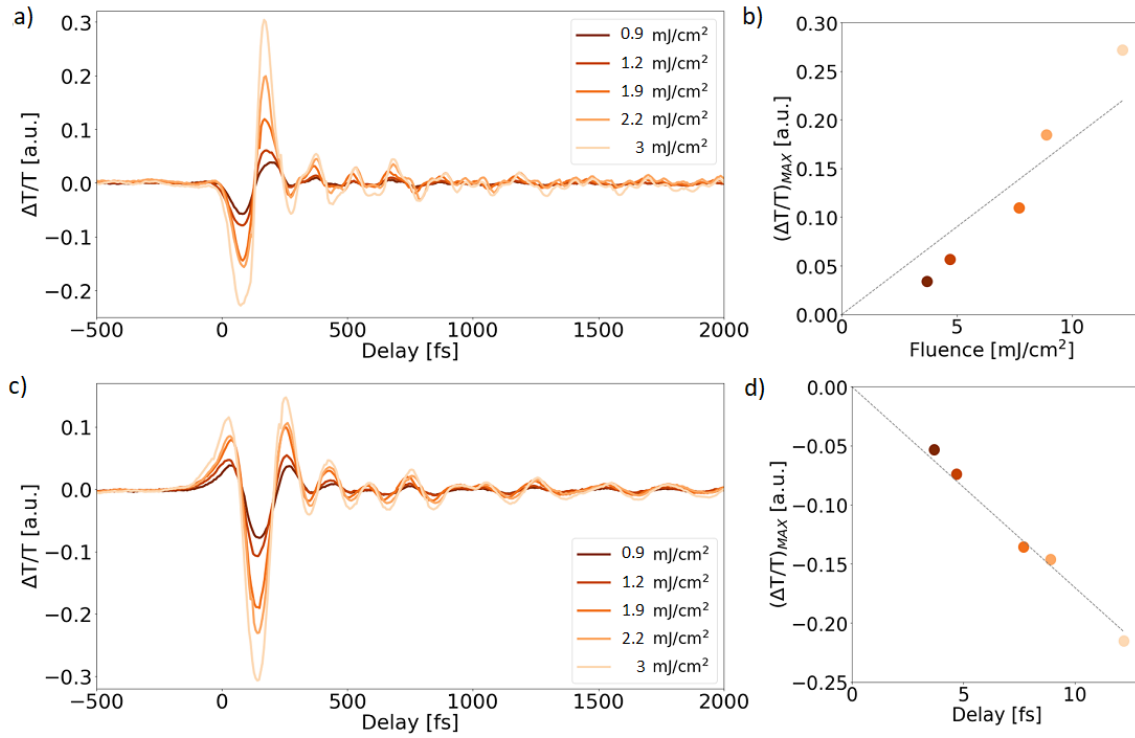


Figure 5.6: $\Delta I/I$ traces at probe frequency a) 367 THz and c) 377 THz, plotted as a function of the pump probe time delay. The colour indicates a particular pump fluence. The b) maximum and d) minimum amplitude of $\Delta I/I$, at 367 THz and 377 THz respectively, is plotted against the pump fluence. The grey dashed lines in b) and d) guide the eye.

We tested the dependence of the signal on the probe energy as well, with a pump fluence of 2 mJ/cm². We recall Equations 2.105 and 2.106, where the dependence of $\Delta I/I$ on the probe field amplitude is shown. The presence of a product of the amplitude of two frequency components in the spectrum makes the signal linearly dependent on the probe fluence.

In Figure 5.7 we plot the time dependent signal at 367 THz and 377 THz in the probe spectrum. The maxima and minima of such signals, respectively, are found to be linearly dependent on the probe fluence.

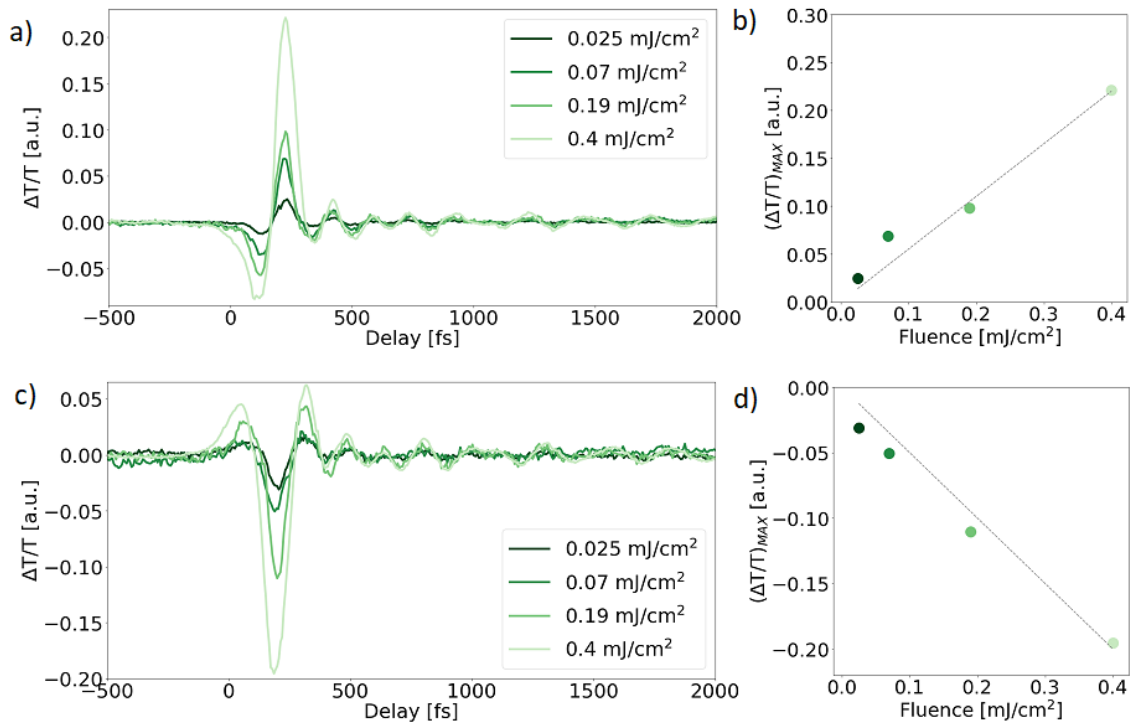


Figure 5.7: $\Delta I/I$ traces at probe frequency a) 367 THz and c) 377 THz, plotted as a function of the pump probe time delay. The colour indicates a particular probe fluence. The b) maximum and d) minimum amplitude of $\Delta I/I$, at 367 THz and 377 THz respectively, is plotted against the probe fluence. The grey dashed lines in b) and d) guide the eye.

5.2 ■ Coherent pump and randomized probe

This section is dedicated to the experiments enabled by the combination of Femtosecond Covariance Spectroscopy to the standard time resolved approach. In practice, we apply a spectral randomization on the probe pulses, which are delayed in time with respect to the spectrally coherent pump ones. A measurement performed within this framework outputs a correlation map for each pump probe time delay. As the time delay steps are tens of femtoseconds wide (in order to properly sample the fastest oscillating response), the time dependent response is sampled by hundreds of points. To efficiently visualize the result of such a measurement, we do not show all the correlation maps. Instead, we exploit the symmetry of the correlation coefficient. In fact, by definition, the map contains the same information on the two sides of the diagonal. Moreover, the signal is the same along the diagonals, as there is no preferential point in the spectrum where the interaction takes place. As shown in Figure 5.8, we rotate each map and express the new horizontal axis as a frequency distance from

the diagonal. We then select one of the two equivalent blocks where the signal is the strongest, and average the correlation signal along the vertical direction (along the diagonal of correlation of a component with itself), ending up with a curve for each time delay. We then stack these curves and build a map, whose z coordinate represents the average (over the block) correlation coefficient, the x axis the time delay and the y axis the frequency difference. We notice that the frequency difference is only meaningful in its absolute value, again due to the symmetry under exchange of two components.

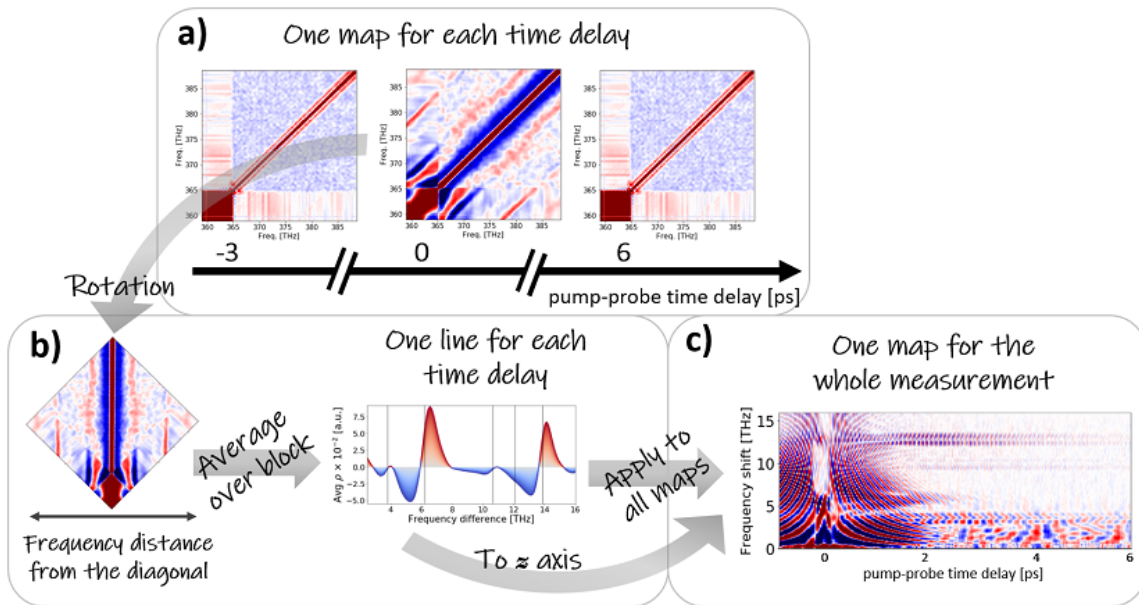


Figure 5.8: Scheme of the data analysis of a frequency and time resolved pump probe experiment performed with randomized probe. a) For each time delay, a correlation map is obtained on the measured transmitted probe spectra. b) Each map is rotated, then the signal is averaged along the diagonal. c) The correlation curves are used to build a correlation map, function of the time delay and the frequency shift from the diagonal.

We explored the possibility of mixing the measured intensities from the sample beam and the reference beam, using the cross correlation ρ_c (discussed in Appendix A). The symmetry of the correlation coefficient is lifted in ρ_c : the two sides of the map are not equivalent. As a consequence, the frequency difference between two frequency components has a well defined sign. ρ_c could be the right tool to investigate the scattering process directionality (in other words any peculiarities of a scattering towards the low or high frequency side).

5.3 ■ Full modulation

As done in the previous Chapter, we start by investigating the sample response when applying a stochastic phase modulation all along the probe spectrum. The measurement performed within this scheme results in the autocorrelation ρ and the cross correlation ρ_c shown in Figure 5.9 as colour maps, function of the time delay and of the probe frequency.

We notice the presence of a correlation signal at all the frequency differences equal to a vibrational mode frequency. Each of these signals oscillates in time with the phonon frequency, as can be observed in the amplitude of the FFT of the correlation maps, performed along the delay axis, where peaks appear along the frequency shift - FFT frequency diagonal. The oscillation could be related to the alternate redshift or blueshift of the probe spectrum, determining a π shift of the signal (recall Figure 4.10). The signal in ρ is a line with finite frequency width that seems to be "split" in two, while the signal in ρ_c is a single band. The most relevant feature of ρ_c is the difference in the amplitude and decay time of the signals belonging to the two sides. From the map we notice that the phonon correlation survives longer when $\Delta > 0$, that is to say when the correlation is evaluated between frequency components in the transmitted beam at a higher frequency ω_i^S than the input components ω_j^R from the reference beam, being therefore satisfied the relation $\omega_i^S > \omega_j^R$.

Around the pump probe overlap, stripes appear along the probe spectrum, with a period inversely proportional to the pump and probe pulses time distance. Their presence could be related to the interference fringes in the average intensity measurement (recall Figure 5.3) which could be caused by XPM [67]. XPM could have an effect on the vibrational signal itself [70], manifesting as the splitting visible in the 6.2 THz band in the ρ map. Another possibility is that such overlap signal could be enhanced by the phonon [71], causing it to oscillate.

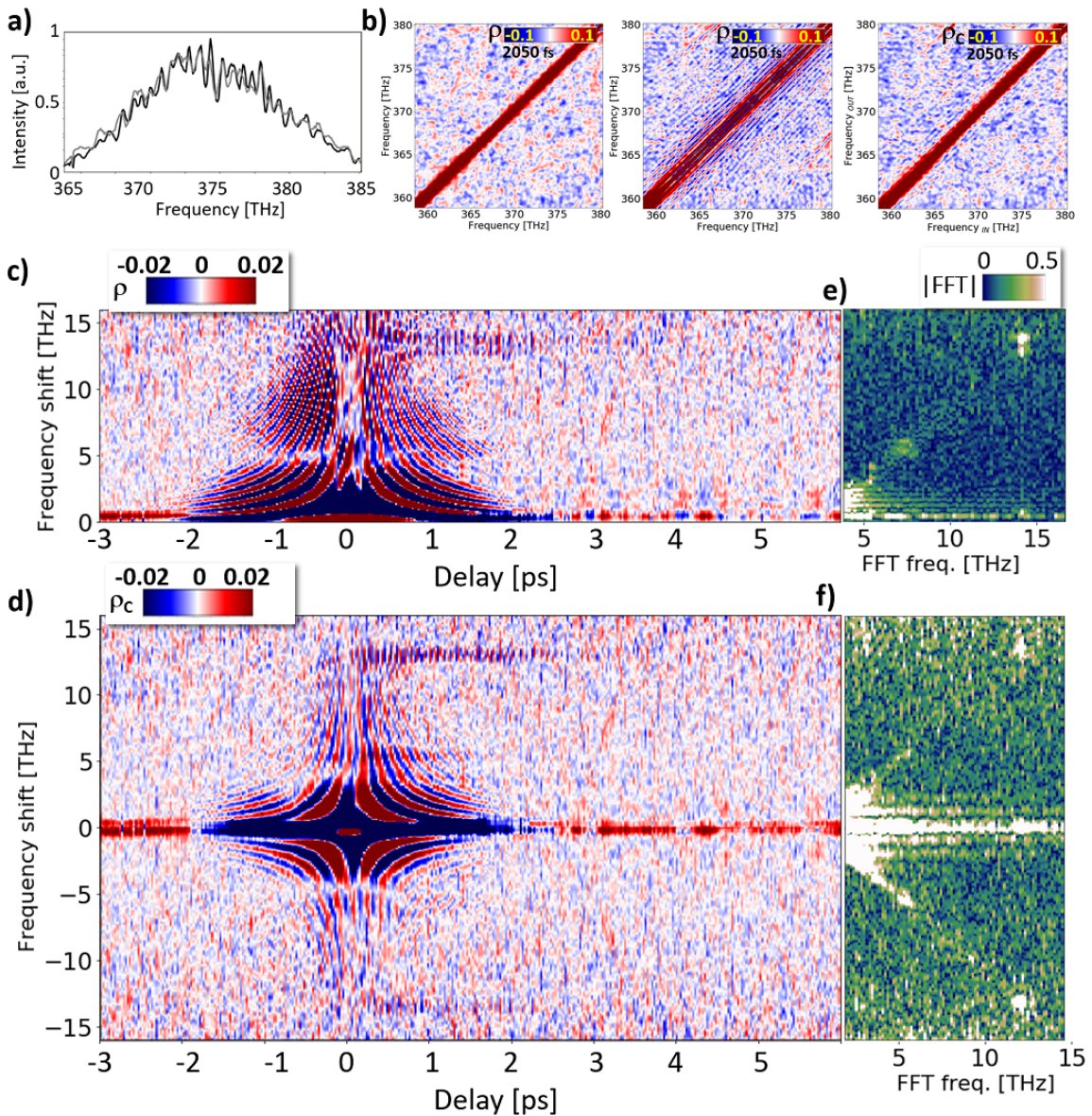


Figure 5.9: Correlation maps as a function of the pump probe time delay for a measurement performed applying phase noise along the whole probe bandwidth. a) Example randomized transmitted and reference spectra. b) Example of auto correlation from the reference beam, auto correlation from the transmitted beam, and cross correlation coefficient, at a time delay of 2050 fs. c) Auto correlation ρ as a function of the frequency shift and of the pump probe time delay. d) Cross correlation ρ_c as a function of the frequency shift and of the pump probe time delay. e) and f) Amplitude of the Fast Fourier Transform of c) and d).

5.4 ■ Half modulation

In this Section we show the results of an experiment carried out by applying a modulation along the upper half of the probe bandwidth. The correlation coefficient (ρ) and cross correlation (ρ_c) maps obtained with the data collected during this experiment are shown in Figure 5.10. As observed at the end of the previous Section, we notice the appearance of a correlation signal at frequency shifts equal to phonon frequencies. The 10.7 THz phonon signal is visible both in the auto correlation and in the cross correlation. The signal lines in the ρ map appear to be split in two, exception made for the 6.2 THz phonon, while the cross correlation shows as a single horizontal band. The FFT amplitude confirms that each of the retrieved correlation features evolves at the corresponding vibrational frequency.

A striking difference between this results and the ones of the previous Section lies the fact that the strongest phonon correlation bands appear for $\Delta < 0$. Moreover the difference in amplitude between the two halves of the ρ_c map is more evident. We believe this is due to an amplification of the signal in the heterodyning process. In fact the spectrally smooth portion of the spectrum might efficiently amplify the radiation scattered towards the low frequency side, which therefore is revealed clearly in the lower portion of the ρ_c map in Figure 5.10. The signal scattered towards the high frequency side, instead, might be partially cancelled by the randomization. According to this interpretation, we expect to see the signal to be enhanced for positive frequency differences when the modulation is put on the low frequency side of the spectrum. In Figure 5.11 we plot the cross correlation maps of two time resolved measurements performed randomizing the spectral phase of half of the spectrum, on the low or high frequency side, in a short range of positive time delays (2 ps to 2.6 ps). We notice that, while the result of an experiment modulating the low frequency side is in agreement with the result shown in Figure 5.10, the cross correlation signal is more evident for a negative frequency difference when the probe pulse modulation is on the high frequency side. This result corroborates the suggested hypothesis that the half modulation configuration enhances the signal originating in a directional scattering.

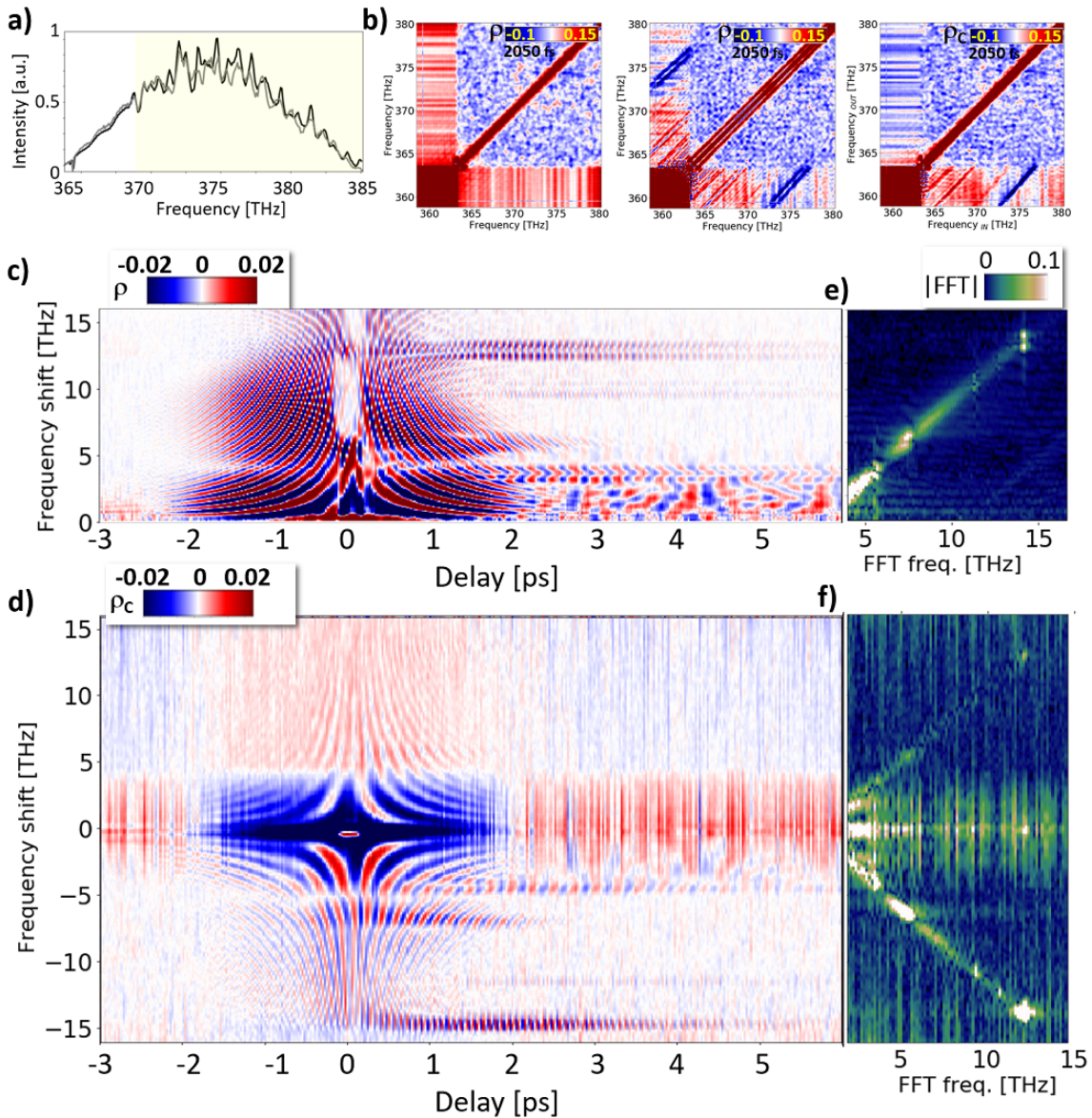


Figure 5.10: Correlation maps as a function of the pump probe time delay for a measurement performed applying phase noise along half of the probe bandwidth. a) Example randomized transmitted and reference spectra. b) Example of auto correlation from the reference beam, auto correlation from the transmitted beam, and cross correlation coefficient, at a time delay of 2050 fs. c) Auto correlation ρ as a function of the frequency shift and of the pump probe time delay. d) Cross correlation ρ_c as a function of the frequency shift and of the pump probe time delay. e) and f) Amplitude of the fast Fourier Transform of c) and d).

5.4.1 ■ Half modulation with mean value shaping

We repeated the experiment employing probe pulses with their upper half randomized, deleting the amplitude of the low frequency portion.

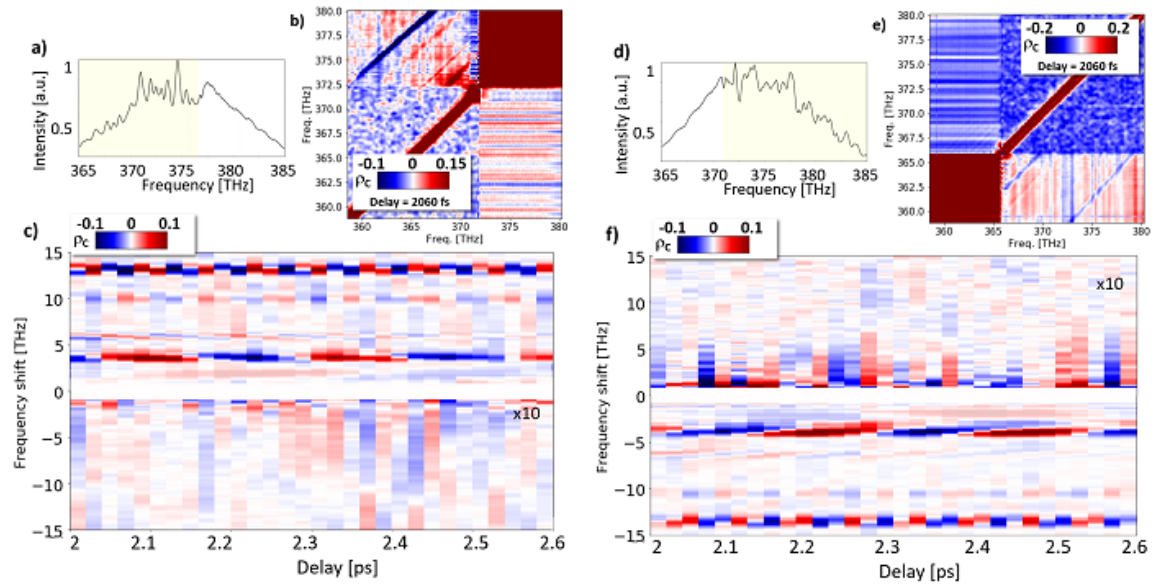


Figure 5.11: Time dependent cross correlation ρ_c on the transmitted spectra of a pump probe measurement with probe randomized on the c) low and f) high frequency side. Example of a modulated spectrum on the a) low and d) high frequency side. b,e) Correlation coefficient ρ_c for a specific time delay from maps c,f) respectively.

The result of this measurement is shown in Figure 5.12. The lines seem to be split in the auto correlation. As in the case of the experiment of Figure 5.10, we observe that the signal is stronger for $\Delta < 0$ than for $\Delta > 0$. Unlike those results though, the signal oscillations in time are somehow harder to interpret, as the 6.2 THz and 14 THz phonon result in more than one Fourier component.

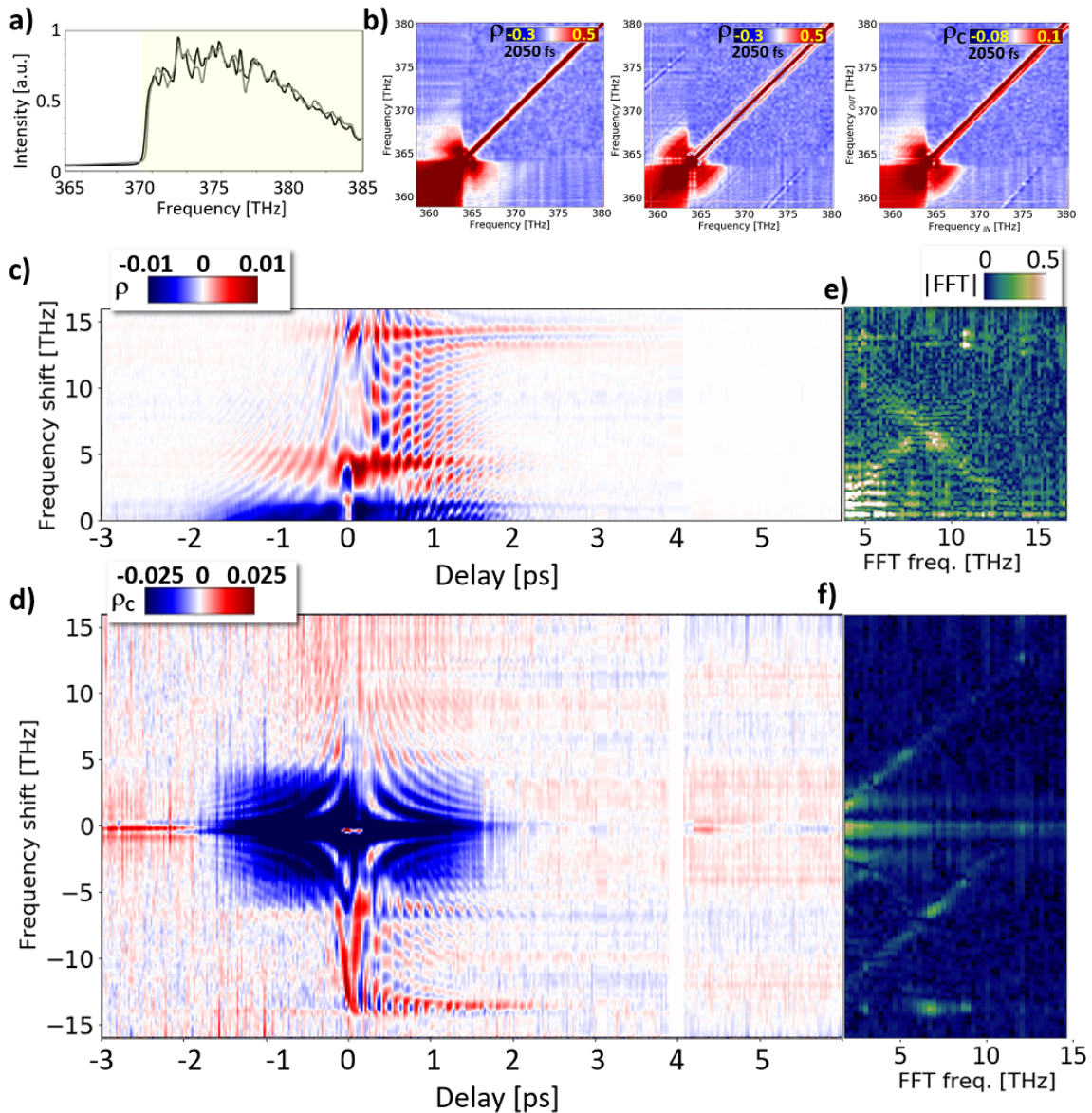


Figure 5.12: Correlation maps as a function of the pump probe time delay for a measurement performed applying phase noise along half the probe bandwidth, while deleting the amplitude of the coherent portion. a) Example randomized transmitted and reference spectra. b) Example of auto correlation from the reference beam, auto correlation from the transmitted beam, and cross correlation coefficient, at a time delay of 2050 fs. c) Auto correlation ρ as a function of the frequency shift and of the pump probe time delay. d) Cross correlation ρ_c as a function of the frequency shift and of the pump probe time delay. e) and f) Amplitude of the fast Fourier transform of c) and d).

5.4.2 ■ Polarization dependence

As anticipated at the end of the previous Chapter, in a single pulse experiment performed randomizing the linearly polarized probe, it is not possible to distinguish between signals originating from phonons of different symmetry. In this section we show the auto correlation and cross correlation maps obtained in a polarization resolved scheme. The spectrally coherent pump and the randomized probe are linearly polarized with a 45° angle, and a polarizing beam-splitter separates the parallel and orthogonal components of the transmitted probe, with respect to its orientation before the sample. Each beam is sent to a photodiode array, so that their detection takes place simultaneously. We performed these measurements randomizing half of the spectrum and deleting the amplitude of the coherent portion, in order to obtain the clearest possible peaks. Because of the fact that in such a configuration the phonon signals do not oscillate in time, only the zero time delay maps are analyzed.

The results are shown in Figure 5.13, at the time overlap of the two beams on the sample. As expected, when $E^{POL} \parallel E^{PR}$, the A phonons are selected, therefore we observe lines at 6.2 THz, 10.7 THz, and 14 THz. On the other hand, when $E^{POL} \perp E^{PR}$, we observe a strong E signal, at 3.8 THz, together with a weak E signal at 12.08 THz, showing opposite sign with respect to a residue of the A lines in the same map and the A lines in the previously discussed map. The rightmost map shows the cross correlation on intensities from orthogonal polarizations. When $\Delta < 0$ only the A_g lines show, when $\Delta > 0$ signals from both A and E phonons appear. The sign of all of the lines in this map is opposite with respect to the signal obtained calculating the auto correlation.

The dynamical properties of the correlation signal are different for each phonon, revealing the sensitivity of the technique to independent phonon populations. An in-depth analysis of the signal, along with its comparison to the results of a time domain analysis of the average transmitted intensity could disclose information on contributions to the nonequilibrium state of the system. For instance, we could distinguish mechanisms with different nature. The "proper" phonon lifetime (or "decoherence" or "dephasing" time) characterizes the decay of a single coherent lattice mode, and as such is affected, as an

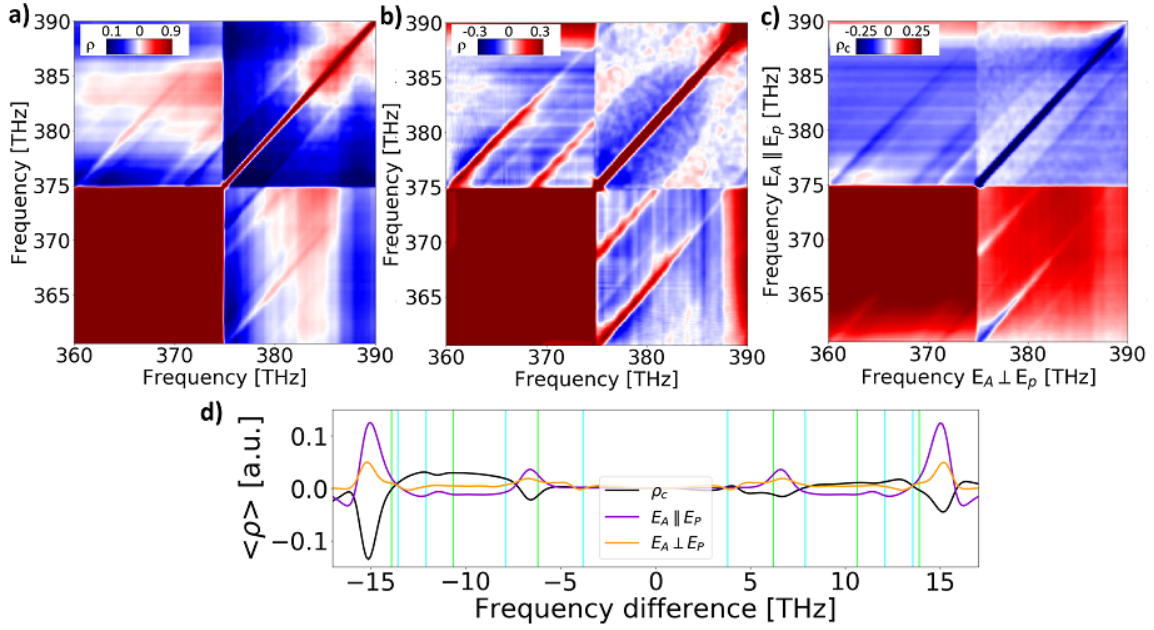


Figure 5.13: Correlation coefficient ρ and cross correlation ρ_c calculated on a measurement performed using pump and probe linearly polarized at 45° and measuring the a) parallel and b) orthogonal polarization to the probe. c) cross correlation calculated the intensity of the orthogonal polarizations from the transmitted beam. d) diagonal cuts on the three median subtracted maps in a) purple, b) orange, c) black. The blue and green vertical lines denote the position of the low frequency E and A α -quartz vibrational modes respectively.

example, by decay to levels of lower energy. It determines the linewidth of an inelastic peak in a spontaneous scattering experiment and the decay time of the signal in an average measurement [72]. On the other hand, the total phonon population relaxes with a time which can only be determined by time resolved techniques, being an incoherent contribution to the signal.

In order to investigate the time scales of the dynamics, we performed a Wavelet Transform (WT) [64] analysis of the signal along the time delay axis, independently for selected components within the probe bandwidth. We remind that the Wavelet Transform of a time dependent curve allows to detect the presence of any Fourier components as a function of time, because it is based on the calculation of the signal FFT on a limited time window, selected by a properly chosen gate function. Therefore the WT is represented by a two dimensional complex valued map, function of the Fourier component and of time. Cuts were extracted at the α -quartz phonon frequencies and fitted with

a sum of two functions defined as a convolution between the pump impulsive excitation and an exponential decay. The need of a two component decay in the correlation coefficient could be attributed to the presence, at zero delay, of the nonlinear interference between the pump and the probe.

$$\begin{aligned}
 (I * D)(\Delta t) &= \int_{-\infty}^{+\infty} ds I(s) D(\Delta t - s) = \int_0^{\infty} ds e^{-\frac{s}{\tau}} e^{-\frac{(\Delta t - s)^2}{2\sigma^2}} = \\
 &= e^{-\frac{\sigma^2}{2\tau^2}} e^{-\frac{\Delta t}{\tau}} \int_0^{\infty} ds e^{-\left(\frac{s}{\sqrt{2}\sigma} - \frac{1}{\sqrt{2}}\left(\frac{\Delta t}{\sigma} - \frac{\sigma}{\tau}\right)\right)^2} = \\
 &= \sigma \sqrt{\frac{\pi}{2}} e^{-\frac{\sigma^2}{2\tau^2}} e^{-\frac{\Delta t}{\tau}} \left[\operatorname{erf}\left(\frac{\Delta t}{\sqrt{2}\sigma} - \frac{\sigma}{\sqrt{2}\tau}\right) + 1 \right]
 \end{aligned} \tag{5.4}$$

where τ is the decay time, σ the width of the pump pulse, Δt the time delay and erf the error function. We perform this analysis on a reference time and frequency dependent average measurement and on the time and frequency dependent correlation coefficients obtained by modulating the whole bandwidth and half of it, to search for any differences in the slow decay time extracted within the two spectroscopic approaches.

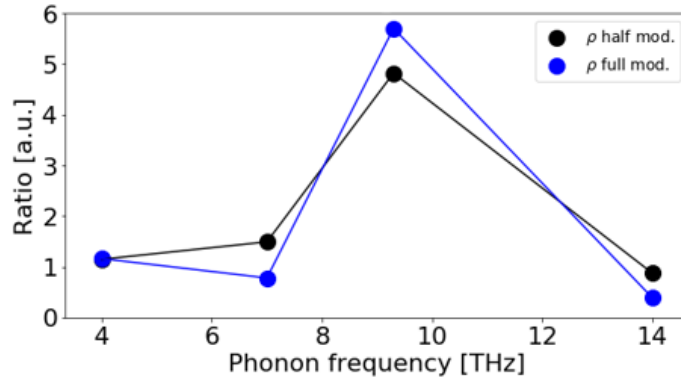


Figure 5.14: Ratio between the slow decay time obtained analyzing the correlation maps and the one obtained reference average measurement.

Figure 5.14 shows the ratio between the slowly decaying τ from the correlation maps over that obtained from the average pump probe measurement, for each phonon. The result of this preliminary analysis shows a remarkable difference in the phonon at 10.7 THz time, as it seems to survive much longer in the correlation maps. One possible reason for this improved visibility of the vibrational-induced correlation feature is that the low frequency spectrum is dispersed along the y axis of the correlation map, while in the average measurement all of the contributions overlap within the probe spectrum.

In this Chapter were reported the results of an **investigation on the dynamical response of a α -quartz sample**. We studied the response of the crystal's coherent vibrational modes in the average transmitted intensity. The latter is modulated in time by oscillations at the vibrational frequencies, and the phase of the oscillation is determined by the effect giving rise to it. We are able to separate the response due to phonons of different symmetry, properly polarizing the pump and probe pulses, and to retrieve the order of the interactions by scanning the pulse fluence, validating the calculations of the quantum model discussed in Chapter 2. Then, we studied the sample response after the pump excitation, obtaining a **dynamical covariance-mediated response**. We explored the full and partial modulation settings enabled by the pulse shaper, discussed in a static configurations in Chapter 4. Each coherent vibrational mode gives rise to a signal which manifests as a sideband in the correlation coefficient map, and oscillates in time, with a decaying amplitude. A preliminary analysis on the data shows that the visibility of the vibrational peaks is very good and, for a small amplitude vibrational mode, orders of magnitude better than in the average measurement. We are currently working in this direction to quantify the differences between the two approaches and complete the characterization of the time resolved covariance based acquisition.

6 ■ Applications

Throughout this Thesis the Femtosecond Covariance Spectroscopy technique was revealed as a powerful means to investigate a transparent sample, and reveal its vibrational modes. Nonetheless, the concepts lying at the foundations of the technique are general and not specific of the experimental apparatus employed nor of the nature of the energy levels considered. In this final Chapter we study the adaptability of the technique to different systems. First, we report the investigation of the vibrational modes in a non-transparent sample, carried out without changing the setup. Then, we focus on the response of the same material (and other samples) studied by applying the covariance based spectroscopy to a system producing X-ray light. Finally, we describe the simulation of a scattering process involving electronic levels, and the result we obtained within the covariance based investigation.

6.1 ■ Samples

Within the experimental scheme adopted to demonstrate the FCS technique and described in Section 3.1, we investigated the response of Copper Germanate (CuGeO_3), a compound widely studied for its peculiar properties, due to a delicate and not fully clarified interplay between the magnetic, orbital and structural degrees of freedom. The relevant units of this crystal are the Cu-O_6 octahedra, which are distorted because of structural symmetry reasons (Cristal Field splitting and Jahn-Teller effect). This causes the originally fivefold degenerate Cu $3d$ levels to split into the $3d_{x^2-y^2}$, $3d_{xy}$, $3d_{xz,yz}$, and $3d_{z^2}$ levels. The energy differences between the ground state and the three excited states are $\Delta_1 \simeq 1.55$ eV, $\Delta_2 \simeq 1.7$ eV, $\Delta_3 \simeq 1.9$ eV. Optical transitions between these levels should be electric-dipole forbidden because the involved orbitals have the same

parity, but normal vibrations in the system mix the d copper orbitals with the p oxygen levels, changing their parity. These dd transitions are therefore referred to as *phonon assisted* optical transitions [73].

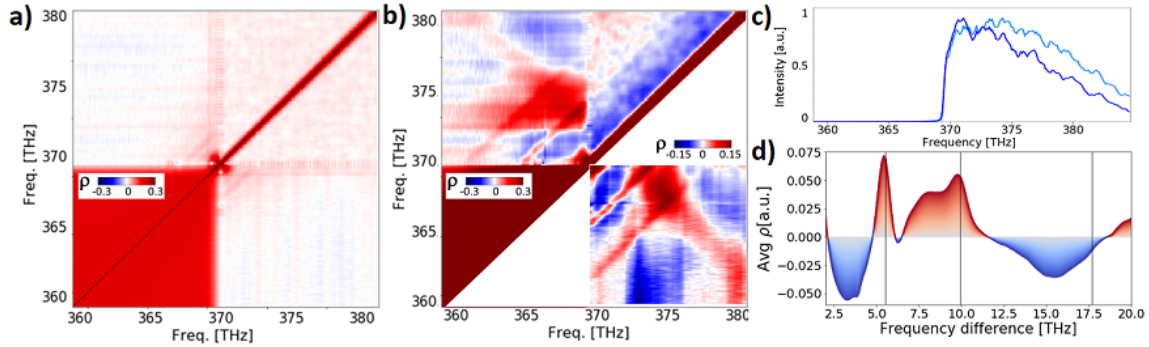


Figure 6.1: Result of a FCS experiment employing phase noise on copper germanate (CuGeO_3) at room temperature, with probe polarized parallel to the microscopic a axis. a) Reference auto correlation. b) Transmitted beam correlation. c) Example of a shaped reference (light blue) and transmitted (blue) spectrum. d) Integral of ρ along the diagonal of the median-subtracted auto correlation shown in the lower right half of b).

For the reasons reported above, CuGeO_3 is light absorbing within the bandwidth of the laser in use, as the central wavelength of the latter is $\lambda_0 = 800$ nm, corresponding to $E_0 = 1.55$ eV. We chose to shape the average value of the spectrum of our pulses in order to retain the portion where the sample absorption is higher. The experiment was performed employing 50% phase noise, with a pulse fluence of 1.8 mJ/cm², on a crystalline sample with in plane microscopic axes a and b . The probe was polarized parallel to the a axis, and the signal parallel to this same axis was detected, in a configuration that allows to select the A_g symmetry vibrational modes. The result is shown in Figure 6.1. Two clear lines appear along the diagonal, which we estimate to be respectively 5.56 THz and 9.95 THz far from the diagonal, therefore being originated by the two lowest energy A_g modes of CuGeO_3 [74]. We find that a highly absorbing sample is still a good candidate for FCS as this technique is sensitive to spectral weight scattering, therefore a low average transmittivity is not an obstacle to its successful application. On the other hand, changes in the transmitted intensity in this wavelength range are particularly meaningful for this sample, as they are related to the aforementioned dd transitions [73]. These changes could be tracked while working in the present nonlinear excitation regime, because the

pulse bandwidth contains the lowest energy excitations. Using the femtosecond covariance spectroscopy technique in combination with a time resolved approach could allow to study the dynamical interplay of the excited coherent vibrational modes and the dd transitions [75].

We therefore demonstrated the general applicability of the technique to samples probed by transmitted pulses. Whenever it should be more convenient to study the transient reflectivity during an ultrafast spectroscopy experiment, the FCS approach would not require any fundamental changes to be successfully employed. The technique is intrinsically insensitive to any linear effect which provide an unwanted background. This, together with the fact that the present scheme relies on a reference beam, makes FCS particularly attractive for experiments on biological samples, where often the sample vessel and solvent response need to be accounted for. We are confident, therefore, that the innovative scheme of FCS will find applications in diverse areas.

6.2 ■ Wavelength range

One of the advantages of the technique presented in this work is that the central wavelength of the light is not a crucial parameter. In a stimulated light scattering experiment, performed far from any electronic resonances and involving low energy modes, the pulse bandwidth is important as determines the maximum excitation energy that can be retrieved, as well as the frequency width of the spectral features (of the shaping and of the detection) that affects the sensitivity of the method. As a matter of fact, we found that when extracting information using the statistical correlation between two frequency components, their distance is the meaningful scale of the analysis.

We could, therefore, change the source wavelength and repeat the experiment. In order to adapt the setup to the new source, the greatest effort would go into adjusting the pulse shaper alignment and geometry. This step could be skipped if the source was able to produce stochastic radiation. This is the case for a **Self-Amplified Spontaneous Emission (SASE) Free Electron Laser (FEL)**. In such a machine, laser amplification and saturation is reached within a single pass of a relativistic electron bunch through a long undulator section.

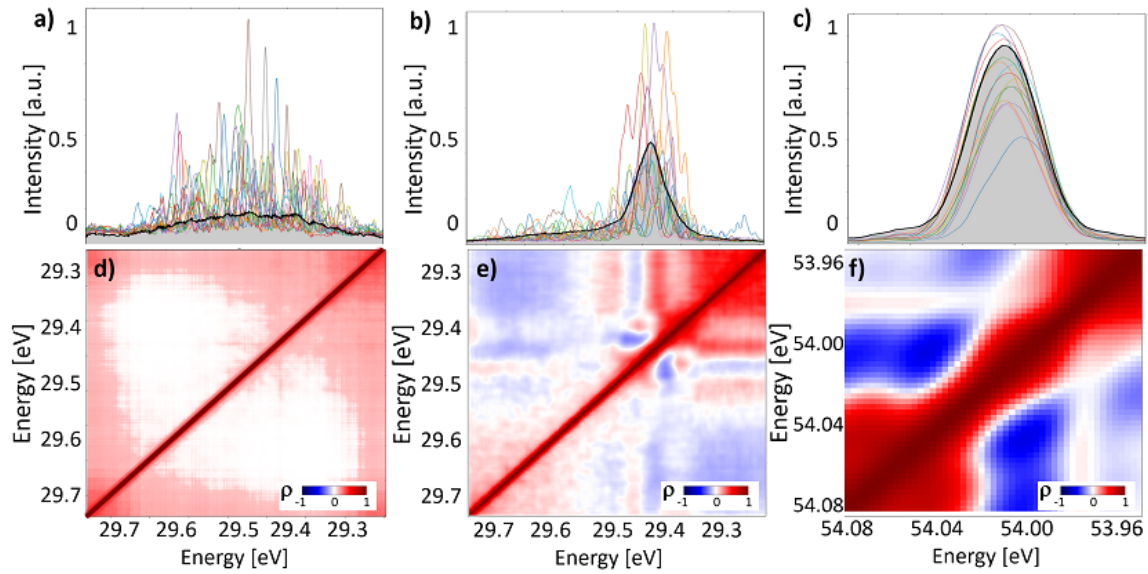


Figure 6.2: FERMI FEL spectra in a) SASE, b) partially seeded and c) seeded mode of operation, acquired during a test. The coloured lines are single shot spectra, while black filled curves represent the average spectrum over the set. The peak at 42.1 nm in b) represents the region of the spectrum overlapping with the seed. The correlation coefficient calculated on each set of spectra is shown below the corresponding plot (d-f).

The lasing process is initiated by spontaneous undulator radiation, which is a stochastic process. As a consequence, measured spectra of individual SASE pulses show several narrow peaks which fluctuate in size, position and height from shot to shot. This intrinsic stochasticity is an advantage to covariance based techniques. The central wavelength of the average spectrum ranges from the deep UV to the hard X-rays, depending on the parameters of the machine [76]. It can be inferred that the output of a SASE FEL is spectrally uncorrelated, and is an ideal candidate to test the validity of the FCS technique. At FERMI (Free Electron laser Radiation for Multidisciplinary Investigations), the FEL built in the site of the third-generation synchrotron radiation facility Elettra, in Trieste, a **seeding** scheme has been implemented, in order to imprint in the output the seed spectral phase coherence, and produce single shot gaussian spectra with very little fluctuations shot by shot (with prevailing central frequency fluctuations) [77]. As opposed to the SASE, this would produce a very high value of the statistical correlation coefficient. The two limiting cases are depicted in the first and third column of Figure 6.2.

We submitted, and obtained, a beamtime at FERMI in order to apply the co-

variance based method to transmitted FEL pulses. The choice of submitting a proposal at a seeded FEL was made because of the possibility of using FERMI in SASE mode (even if it is not meant to work in this configuration), and of detuning the seed from the undulator resonance to impart spectral coherence only on part of the spectrum (see middle panel of Figure 6.2).

Following the results obtained in the laboratory, several configurations of the FEL were explored, from the seeded to the SASE mode through several intermediate configurations. Other FEL parameters were changed to monitor the effects on the experiment. The spectrum central wavelength was chosen to coincide with a transparency region of the samples in order to favor inelastic scattering from vibrational levels over one photon absorption, or to coincide with an absorption edge to increase the cross section of inelastic scattering from electronic levels. Being the fundamental seed wavelength $\lambda_{\text{SEED}} = 255$ nm, we worked with its 7th harmonic, $\lambda_7 = 36.43$ nm, and its 6th harmonic, $\lambda_6 = 42.5$ nm, as a seed. Analyzing in real time the acquired data, we were able to grasp the evolution of the frequency correlation while changing the experimental parameters.

For the experiments, the FEL was set to operate at the seed 7th harmonic, thus with a central wavelength $\lambda_7 = 36.43$ nm. The investigated samples were crystalline films of Si (with thickness $\delta = 1$ μm), mounted in a vacuum chamber at the experimental station EIS-TIMEX [78].

The clearest results have been obtained on the silicon film, which shows a strong resonance. We observed a recurring signal at the frequency of a Raman resonance of carbon, of about 47 THz, which we attributed to carbon-coated optics in the beam transport. This means that the optical elements must be carefully chosen and characterized before performing this experiment, which can be challenging to accomplish at a user facility. On the other hand, this means that the FCS technique could be implemented to test the status of the beam optics themselves, and of course to test the beam spectral properties [79]. With the sample, one more broad but intense feature is visible, centred around 70 THz, shown in Figure 6.3. This was obtained with partially coherent pulses, when tuning the seed position in the low and high frequency side of the spec-

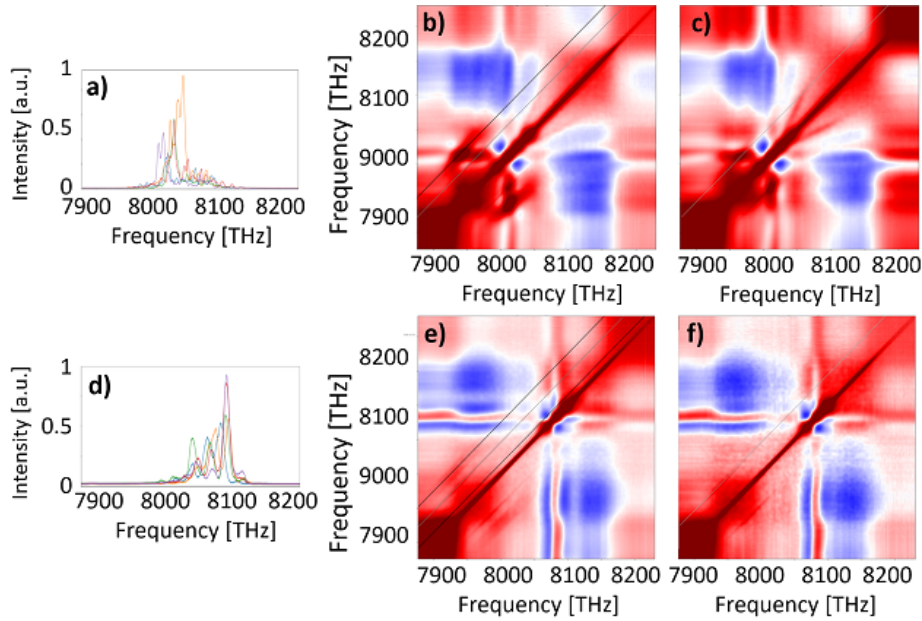


Figure 6.3: Results of the experiment performed at the Fermi FEL on a Si sample, using partially coherent pulses, with seed tuned on the low (a-c) or high (d-f) frequency side of the spectrum. Correlation coefficient with (b,e) and without (c,f) the sample. The gray line is located at 47 THz and present with and without the sample, the black line at 70 THz appears only when the sample is investigated.

trum. This feature could be representative of the scattering from an electronic state of a surface reconstruction of Si [80].

The possibility of working with the machine scientists allowed us to scan many machine parameters. We were able to observe unique patterns on the covariance maps related to the lasing process and to an enhancement of the Si signal. In a FEL like FERMI, the electrons can develop micro-bunching instabilities (μ BI) which are detrimental to the energy stability of the lasing process. The laser heater (LH) is a light beam that overlaps to the electrons to induce a uniform increase of the energy spread of the bunch, damping the μ BI. The LH pulse shaping is used to imprint an energy and/or density modulation onto the bunch, and therefore affects the lasing. This allows to control the properties of the output [81]. If two delayed and chirped copies of the LH pulse recombine onto the electron bunch, they interfere and generate a beating that modulates the bunch. This modification is preserved up to the interaction with the seed laser. The presence of two different wavelengths leads to a frequency mixing process that produces controlled sidebands, whose position with respect to the

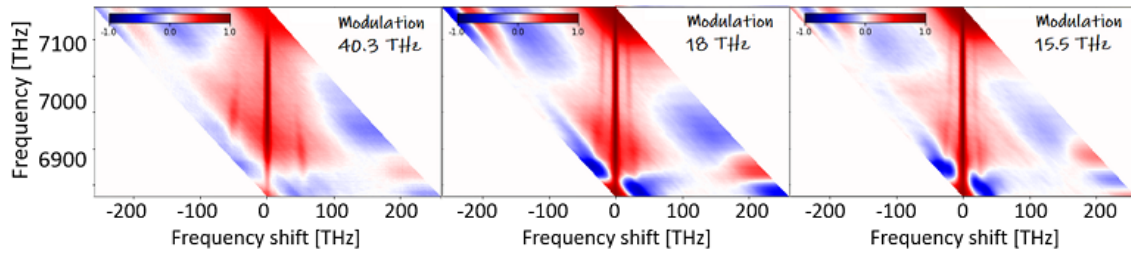


Figure 6.4: Measurements performed with SASE FEL pulses, produced introducing a modulation with the LH with wavelength $\lambda_{LH} = 7.44, 16.5, 19.3 \mu\text{m}$.

central seeded peak varies with the beating frequency (and that can be amplified separately by tuning the machine parameters). It was shown that when the FEL is operated in SASE mode, the current modulation produces a regular spike train [82].

We tested the covariance based acquisition applying a LH modulation with wavelength $\lambda_{LH} = 7.44, 16.5, 19.3 \mu\text{m}$. The results obtained in SASE configuration are shown in Figure 6.4. The correlation maps show a diagonal line whose position is proportional to the frequency of the modulation introduced by the LH. The correlation reveals a process taking place during the laser light generation, and involving frequency pairs along the whole spectrum, therefore it might be revealing of the frequency mixing process leading to the sidebands generation, which cannot be distinguished from the average spectrum.

We used this machine configuration by repeating the experiment on Silicon using partially seeded pulses produced with a low wavelength LH modulation. We used a wavelength of $\lambda_6 = 42.5 \text{ nm}$. In Figure 6.5 we report the correlation coefficient calculated on this set of measurements. First, we notice that the background of ρ is reminiscent of amplitude fluctuations, as intensity is removed from the central peak to be transferred to the sidebands. We also notice the presence of sidebands with a distance proportional to the modulation, present with as well without the sample. A value of $\lambda_{LH} = 19.3 \mu\text{m}$ was chosen as it matches the vibrational mode at $\nu_{Si} = 15.5 \text{ THz}$ of crystalline Si. As can be seen from the bottom plots of Figure 6.5, the signal from this mode seems to be enhanced at resonance.

We chose to fix $\lambda_{LH} = 19.3 \mu\text{m}$ and change the energy of the FEL pulses (values $E = 8, 6, 4, 2, 1 \mu\text{J}$), in a partially seeded configuration. The result is shown in Figure 6.6. The sidebands are visible on the maps calculated on the

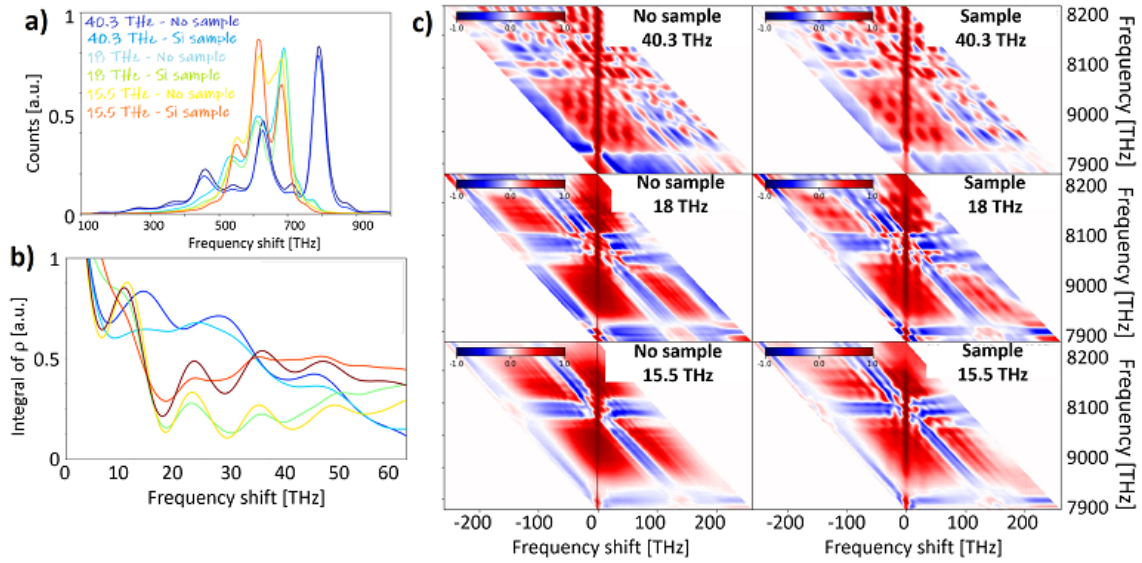


Figure 6.5: Measurements on crystalline Si performed with partially seeded FEL pulses, with a low wavelength laser heater modulation at $\lambda_{LH} = 7.44, 16.5, 19.3 \mu\text{m}$. a) Average spectra, c) correlation coefficient, and b) integral of the correlation coefficient, with or without the sample during the three measurements.

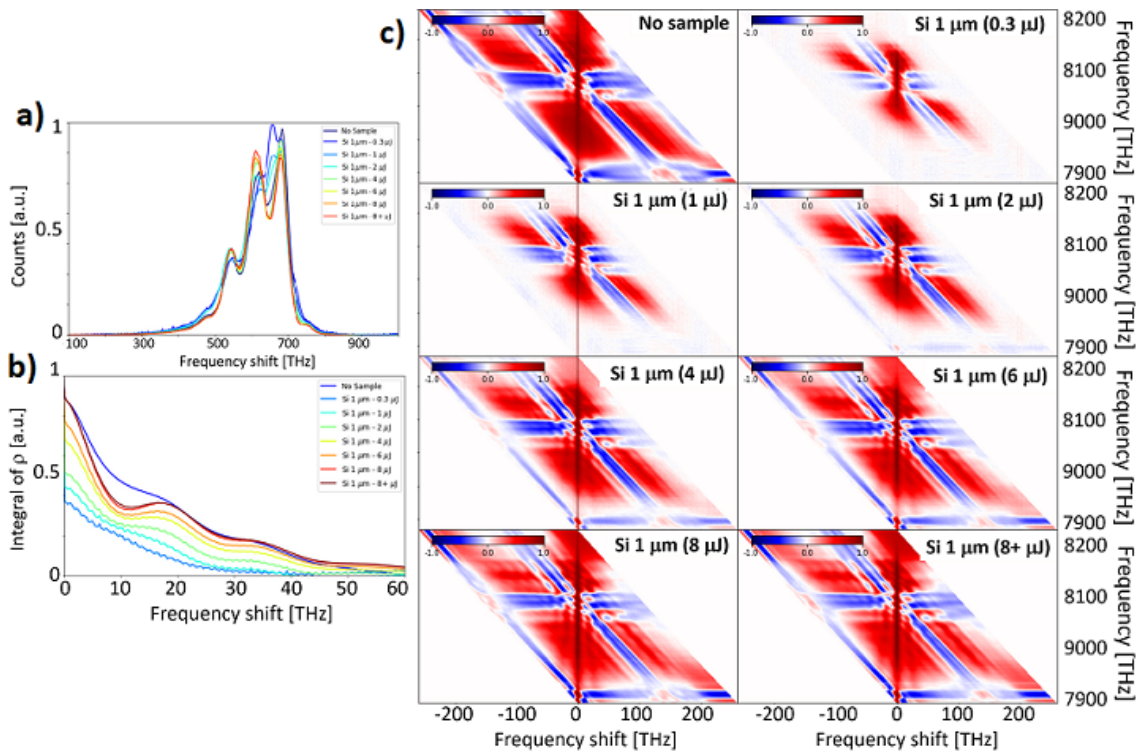


Figure 6.6: Measurements on crystalline Si performed with partially seeded FEL pulses, with a low wavelength laser heater modulation at $\lambda_{LH} = 19.3 \mu\text{m}$, scanning the pulse fluence.. a) Average spectra, c) correlation coefficient, and b) integral of the correlation coefficient, with or without the sample.

transmitted spectra, and seem to be enhanced by the increasing pulse energy, therefore confirming that they origin from scattering in the sample.

6.3 ■ Scattering process

Resonant Inelastic X-ray Scattering (RIXS) is a photon in - photon out technique capable of probing elementary excitations in complex materials by measuring their energy, momentum, and polarization dependence. The incoming photon energy is tuned to resonate with an atomic absorption edge. When the sample is illuminated, the incident photon promotes a different type of core electron into an empty valence shell. The presence of a hole in the electronic core implies a highly energetic and therefore unstable state for the system, that decays within few femtoseconds. RIXS is governed by fluorescent decay, in which the empty core-state is filled by an electron and at the same time a photon is emitted [83]. The emitted photons map a portion of the electronic excitations in between the two levels. Therefore a RIXS experiment needs a soft to hard X-ray tunable source, and is widely used at SASE FELs facilities. The necessity of measuring the RIXS response at different incoming photon energies, though, calls for a scan of the energy of the incident beam, which needs to be monochromatized, leading to huge energy fluctuations and the necessity to acquire a very large amount of scattered spectra. We performed a simulation to demonstrate that no energy filtering is needed if a covariance based detection is applied to the scattered spectrum [84-86].

The idea of a correlation based retrieval of the RIXS signal stems from the fact that the statistical distribution of the scattered photons is representative of the spectral content of the single SASE pulse even though on average a few photons will be counted on the inelastically scattered region. We performed a simulation of a RIXS experiment on CuGeO_3 , in resonance to the oxygen K-edge. The simulation starts from the wavelength dependent RIXS data measured in [87]. The RIXS process is simulated by means of realistic parameters for the lasing in SASE mode (bandwidth $\Delta E/E \approx 1\%$ and width of the correlation spike 5% of the full bandwidth). It is assumed that the scattering cross section is smaller than 10^{-6} , so that every single shot SASE pulse generates a very small number of counts on a detector acquiring the inelastically scattered light. It is

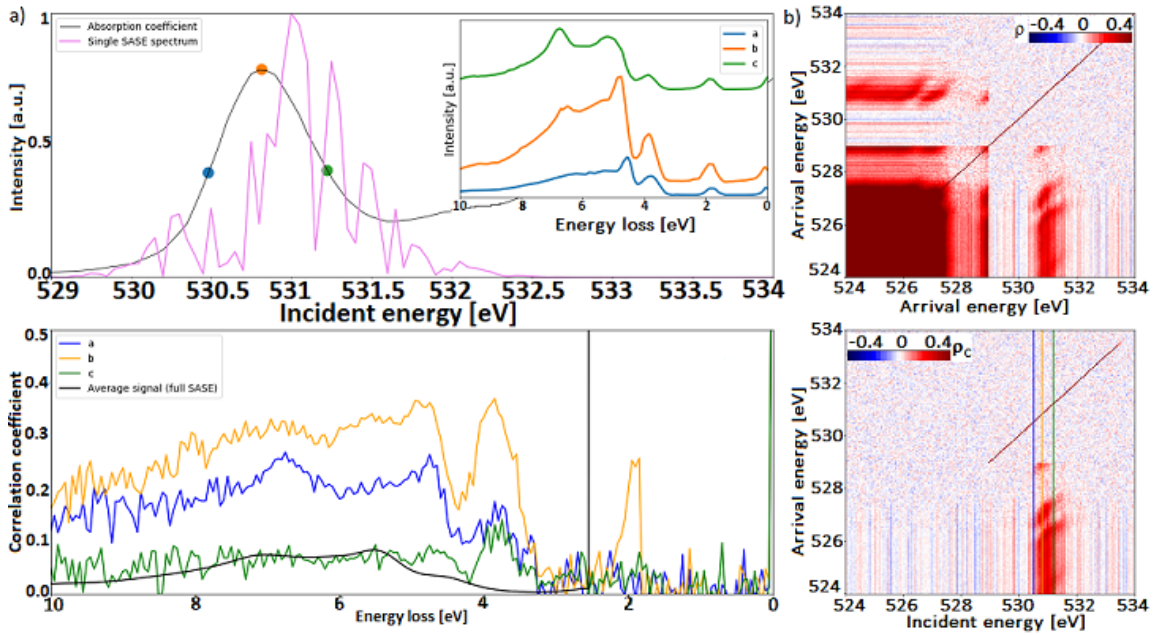


Figure 6.7: Simulation of the covariance based detection applied to a RIXS experiment on CuGeO_3 performed with SASE pulses. a) Data adapted from [87]: few selected RIXS spectra (coloured curves in inset) and absorption coefficient of the sample (gray curve). Example of SASE spectrum used in the simulation (pink curve). Auto (b) and cross (d) correlation calculated on the output spectra. c) Single scattered spectrum (gray line) and average scattered spectrum (black curve). Cuts of the cross correlation coefficient representing the RIXS response obtained at different input wavelengths.

important to note that the acquisition of the scattered light averaged over multiple pulses results in a spectrum where contributions scattered from different incoming energies cannot be distinguished.

In the same Figure we plot the frequency correlation of the scattered spectra. It is easy to identify the inelastically scattered features (which are highlighted by colored vertical lines and plotted to the left). If we compare the signal extracted from ρ with the measured RIXS spectra, we see that the spectral features are well reproduced. We stress that in a noise correlation based analysis the measurement is performed in full bandwidth mode and the inelastic scattering features at different incoming photon energies are acquired simultaneously. Therefore the full RIXS response across the absorption edge could be retrieved in an experiment lasting few minutes. Moreover, the elastic peak does not hide inelastic excitations. For this reason, the FCS method is particularly suited to

study the collective excitation dispersion in systems where the inelastic excitation has a small cross-section.

6.4 ■ Higher order correlation coefficients

The analysis conducted so far aims at revealing the coupling between spectral components, assuming no interactions between the excited states. In the specific case of a system in the electronic ground state, whose only excited states are due to the lattice, this could be interpreted as the absence of any vibrational anharmonicities. In a broader perspective, excited states of different nature could be coupled. As an example, competing collective phases of matter emerge in "complex" materials where various degrees of freedom (spin, charge, orbital, lattice) interact. The role of these excitations is often addressed by means of time resolved spectroscopy, which allows to disentangle their contributions based on their different dynamical time scales, which are determined by the origin of the excitation. Raman scattering is another popular technique used to extract the coupling constants and to selectively study low energy electrons (at the Fermi surface) from different regions of the Brillouine zone by changing the polarization of light [88].

To reveal the coupling between energy states determining the properties of a material, Femtosecond Covariance Spectroscopy could be a powerful asset, providing the excitation spectrum as well as a map of the correlation, therefore the coupling, among the levels. The technique should be extended to exploit the inelastic light signal scattered off of different low energy levels to directly estimate the entity of their mutual interaction. While this passage is conceptually straightforward, the appropriate analytical routine still needs to be addressed.

One possible direction is that of using multiple intensity points within the spectrum to define a n -body correlation coefficient, whose meaningful parameter would clearly be the product $\langle I(\omega_1)I(\omega_2)\dots I(\omega_n) \rangle$. The frequency variables $\omega_1, \omega_2, \dots, \omega_n$ can be redefined as differences $\Omega_1, \Omega_2, \dots, \Omega_{n-1}$ from a single independent variable ω . Upon integration over ω , the correlation coefficient becomes function of the frequency differences Ω_i , therefore of the excitation spectrum scale. This formulation could provide a direct insight on the inter-

action between the low energy levels. A preliminary analysis has been carried out using a three body correlation coefficient defined as

$$\rho^{(3)}(\Omega_i, \Omega_j) = \int d\omega \frac{\langle I(\omega + \Omega_i) I(\omega + \Omega_j) I(\omega) \rangle}{\langle I(\omega + \Omega_i) I(\omega + \Omega_j) \rangle \langle I(\omega) \rangle} \quad (6.1)$$

function of the variables Ω_i and Ω_j , representing in this case the vibrational spectrum of the sample.

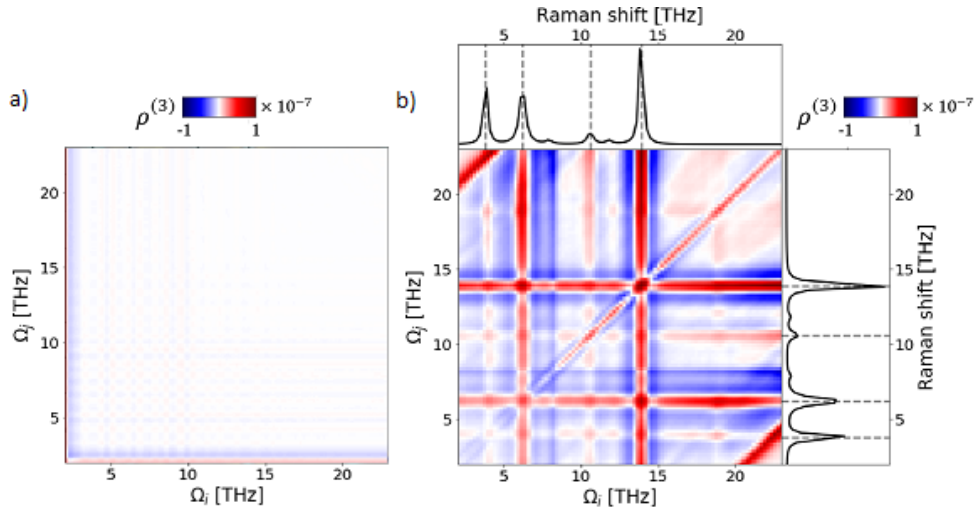


Figure 6.8: Three body correlation coefficient $\rho^{(3)}$ calculated on a) reference spectra and b) transmitted spectra by α -quartz (whose vibrational spectrum from [41] is plotted on top and on the left of the colour map).

The coefficient $\rho^{(3)}$ in Figure 6.8 is calculated on data measured in a transmission experiment on α -quartz with randomized pulses. It reveals vertical and horizontal structures at the vibrational frequencies of the sample. We interpret these structures as two body correlations originated by the vibrational resonances which show up regardless of a third intensity factor (hence the line).

Finally, a univocal connection must be established with the time first and second order correlation functions $g^{(1,2)}(t_1, t_2)$ of quantum optics [39, 89–92].

7 ■ Conclusions

In order to reveal a signal arising from a nonlinear interaction, several spectroscopic techniques are nowadays adopted. In spite of their practical and fundamental differences, they have in common to rely on pulse to pulse consistency to deliver information on a nonlinear process. With the work presented in this thesis we show, instead, that we can successfully leverage upon noise to retrieve a nonlinear signal. To achieve this goal, we exploited the fact that a weak signal introduces a strong spectral correlation, which can be revealed even when the output spectra fully spectrally and spatially overlap with the excitation pulse. Based on these principles, we propose a novel approach to a nonlinear spectroscopy experiment, called Femtosecond Covariance Spectroscopy.

To provide a solid basis for the validation of the technique, we focused on a third order nonlinear process, inelastic light scattering, which is prompted by the mixing of intense electric fields in a transparent material. The interaction implies that the measured intensity at some point in the transmitted spectrum is statistically related to the intensity at other points of the spectrum, whenever their energy distance coincides with an energy level of the sample involved in the scattering. We performed inelastic light scattering experiments from vibrational modes of a benchmark sample, α -quartz. We employed a near infrared laser with central wavelength in a transparency region of the sample, and bandwidth larger than its lowest energy vibrational modes. We found in the correlation coefficient sidebands that reproduce the vibrational spectrum of the sample. Their lineshape changes according to the presence or absence of a non modulated portion of the spectrum, heterodyning the scattered radiation. In fact we find that a partial spectral randomization is most efficient

in preparing a pulse with no pre-existent correlation, that, at the same time, provides a local oscillator for the sample-induced fluctuations to be amplified. In this scheme, the ultrashort pulse provides, at the same time, intense electric fields to stimulate a response, and noninteracting components to reveal it. The self-heterodyned nature of the acquisition is accounted for in a fully quantum model.

The technique can be adapted to a pump - probe scheme by exciting the sample with a separate, intense and spectrally coherent pump pulse. Our measurements of the average transmitted probe intensity performed using a pump to excite coherent vibrational states, reveal that oscillations in the response are initiated in-phase by the pump and evolve at the vibrational frequencies. Such a response is an ideal candidate to test a covariance based probe, as the spectrum undergoes a red-shift or a blue-shift alternatively in time, and the correlation coefficient is found to oscillate in time at the phonon frequency. The investigation we started with this Thesis aims at establishing the signatures in the correlation that resolve a thermal from a coherent vibrational state. In fact, if a quantum optics model describes accurately the results of a standard pump probe experiment on α -quartz, the theoretical framework must be completed in order to describe a pump probe approach employing randomized pulses and a covariance based retrieval.

The proposed method has proven to be a powerful probing scheme in an optical spectroscopy experiment, and can be successfully translated into different languages. To further motivate the interest in the investigation we initiated, and open a possible future direction, let us imagine a scenario where noise is unavoidable as it is intrinsic to the generation of light. One such stochastic source is the sun [2, 93], whose light sustains life on this planet. Clearly its statistical properties must be taken into account when studying systems absorbing light in a natural environment, as photosynthetic and photovoltaic systems. The absorption of sunlight in photosynthetic organisms results in the creation of electronic excitations, which are transferred to dedicated reaction centres, where ultimately chemical bonds are produced to store energy in the long term [94]. Because of the ultrafast scale of the energy transfer between the pigment and the reaction centre, ultrafast spectroscopy is employed to investigate

the mechanism of the transfer, which is not yet well understood. Nonetheless, in the natural environment, light harvesting complexes experience excitation through the incoherent light from the sun [95]. It has theoretically been shown that quantum beatings in the dynamical response, therefore coherent excitations exist under incoherent excitation [96]. Noisy light sources are exploited to reproduce the effect of sunlight, and have provided the experimental verification of the theoretical expectations [97–99]. A statistical approach to the light interaction with such a complex system could provide new insight on the dynamical coupling between the electronic levels.

The experiments have shown that consistent information is present in the correlation maps, but more incisive analytical and conceptual tools are needed to assess the different contributions. To fully characterize the FCS technique there are still steps to take. Nonetheless we believe that the present work sets the basis for the development of a technique that successfully conveys information beyond traditional schemes.

Appendix A

Correlation coefficient

Here we describe the correlation coefficient used in the Thesis to reveal the nonlinear signal and discuss its properties.

A.1 Auto correlation

We call *auto correlation* the Pearson correlation coefficient ρ when it is calculated on a set of frequency dependent intensity spectra from a single measurement channel. In other words an auto correlation is calculated on spectra which were all transmitted by the sample or measured from the reference beam. ρ is a normalized form of the covariance, therefore its values range from $\rho = 1$ to $\rho = -1$, representing a positive correlation or a negative correlation (anticorrelation), respectively, between the variables. It is defined as:

$$\rho = [\langle I(\omega_i)I(\omega_j) \rangle - \langle I(\omega_i) \rangle \langle I(\omega_j) \rangle] / \sigma_i \sigma_j \quad (\text{A.1})$$

where the indices i, j refer to the frequency component within the pulse spectrum.

The Pearson coefficient assumes a linear relationship between the variables. Its value is related to the goodness of a linear fit of the distribution. In Figure A.1 we show *scatter plots* of simulated data. They are produced plotting, for each repetition, $I(\omega_i)$ versus $I(\omega_j)$. The corresponding value of the Pearson correlation coefficient is reported on top of each scatter plot. On the top row we observe a transition from the maximum value $\rho = 1$, to the minimum, $\rho = -1$, through smaller absolute values. It can be inferred that higher values of ρ are

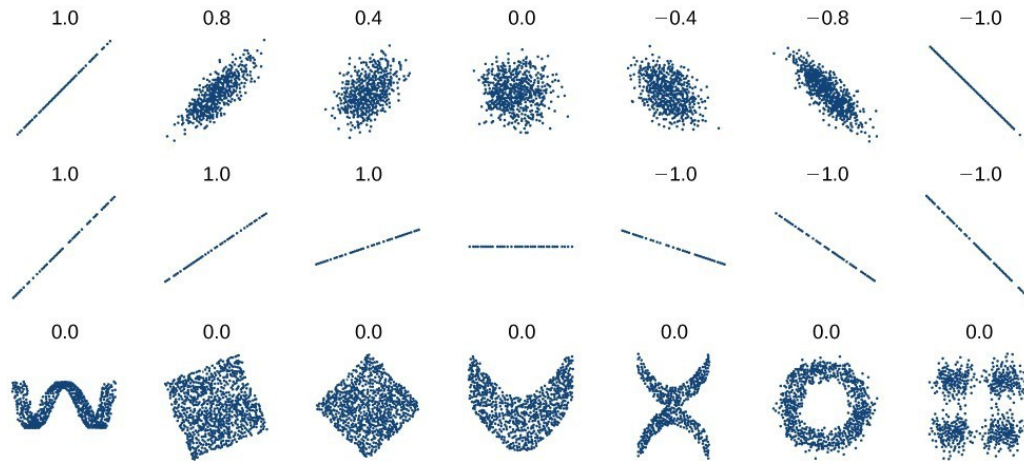


Figure A.1: Scatter plots of example data distributions and corresponding value of the Pearson correlation coefficient. On the top row we observe a transition from the maximum to the minimum value of ρ through smaller absolute values. In the middle and bottom row we report different cases that lead to the same value for ρ .

obtained when the data points are very close to a linear fit of the distribution. In other words, the closer the Pearson coefficient value is to ± 1 , the more the relationship between the variables is linear. The value of the correlation coefficient must be used carefully. In fact, stronger or weaker linear associations lead to the same value of the coefficient (see middle row of Figure A.1). Moreover, when $\rho \rightarrow 0$, it is not possible to draw any conclusions on the relationship between the variables. They could be uncorrelated, as in the middle plot of the top row, where randomly distributed points lie in the plane. The same value is obtained, however, when the distributions have a non monotonic association, as in the cases of the bottom row of the same Figure. We conclude that a scatter plot is a useful way to clarify the meaning of a value of ρ .

As mentioned above, ρ assumes a linear relationship between the variables, therefore it is not testing a hypothesis for the origin of the data, so does not distinguish dependent and independent variables. This could be inferred also by the symmetry of ρ upon exchange of the factors $I(\omega_i)$ and $I(\omega_j)$. ρ , moreover, does not properly weigh the data points, which would be needed when a subset of the data is measured with greater precision (not the present case).

A.2 Cross correlation

It is instructive to rewrite ρ as a function of the frequency difference $\delta = \omega_i - \omega_j$. Therefore, substituting $\omega_i = \omega$ and $\omega_j = \omega + \delta$:

$$\rho(\omega, \delta) = \frac{\langle I(\omega)I(\omega + \delta) \rangle - \langle I(\omega) \rangle \langle I(\omega + \delta) \rangle}{\sigma_\omega \sigma_{\omega+\delta}} \quad (\text{A.2})$$

which reveals that any meaningful information extracted from the analysis of the covariance is actually a function of the frequency distance between two components δ , whose sign is not defined.

We could also input ρ one intensity from the transmitted beam and one from the reference beam. We refer to this as a *cross correlation coefficient*, ρ_c . It reads:

$$\rho_c = \frac{\langle I^R(\omega_i)I^S(\omega_j) \rangle - \langle I^R(\omega_i) \rangle \langle I^S(\omega_j) \rangle}{\sigma_i^R \sigma_j^S} \quad (\text{A.3})$$

This coefficient has a normalized amplitude, but the result is clearly different when $I^R(\omega_i) > I^S(\omega_j)$ or $I^S(\omega_j) < I^R(\omega_i)$, therefore we cannot rewrite it explicitly as a function of δ . In this case, the degeneracy under exchange of the intensity factors is lifted. We will make use of ρ_c to investigate processes with a well defined directionality within the spectrum.

A.3 Simulated pulses

We simulated numerically a set of Gaussian spectra with fluctuating parameters representing a global instability of the intensity. A few limiting cases are sketched in Figure A.2, along with the Pearson correlation coefficient ρ calculated on each set.

We randomize shot to shot the simulated spectra, with fluctuations prevailing in the central frequency, amplitude or width. When the amplitude of the pulses is strongly fluctuating, everywhere $\rho \approx 1$, as the fluctuation involves the whole spectrum. When the spectra are oscillating rigidly around a average frequency position, the correlation coefficient shows areas of negative or positive correlation when considering pairs of components on the same side or on opposite sides of the spectrum, respectively. In fact, one component and

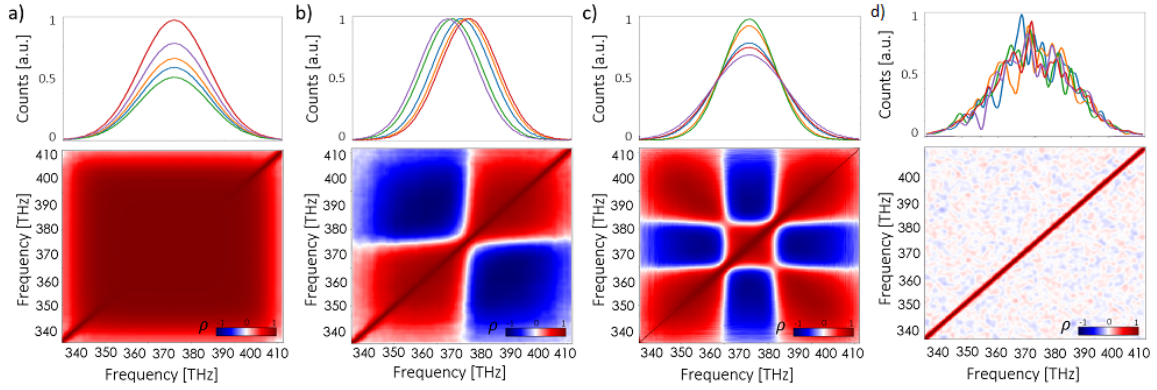


Figure A.2: Correlation coefficient calculated on sets of simulated spectra with prevailing a) amplitude, b) central frequency, c) envelope width noise, or d) narrow width noise. In a,b,c) large regions of the spectrum are correlated or anticorrelated when, shot by shot, the components within fluctuate in phase or out of phase. In d) all the components are uncorrelated.

its neighbours will behave similarly, but in opposition to components on the other side of the spectrum. Finally, when the spectrum is "breathing", spectral weight is distributed from the peak to both sides (or vice versa), therefore components belonging to these portions are negatively correlated to those in the middle. This basic simulation, even if representing an overly simplified system, allows to become familiar with the meaning of broad features in the correlation maps, which, when present, are related to global spectral weight shifts. In the opposite limiting case, the pulses can suffer from narrow spectral width noise that results in a vanishing correlation coefficient for all the pairs of components within the spectrum. The diagonal has still a value close to 1, as it represents the correlation of a component with itself, and its width is proportional to the average width of a spike (referred to, in the Thesis, as correlation width Δ_{corr}). This is the most favourable condition to reveal any correlations introduced by a nonlinear interaction.

Appendix B

Supplementary analytical tools

Here we present a few analytical tools necessary to integrate the theoretical and phenomenological models presented in Chapter 2 for the description of the single and double pulse experiments.

B.1 Notes on the Liouville representation

In Chapter 2 we adopted the formalism based on the density operator in the Liouville representation. We summarize here some of its properties, which will help clarifying its physical interpretation.

The state of the **material** is represented by molecular wavefunctions

$$\Psi_M(r, t) = \sum_n c_n \Psi_n(r, t) \quad (\text{B.1})$$

where Ψ_n constitute a basis of molecular eigenstates of the molecular unperturbed Hamiltonian \hat{H}_M , and c_n the projections of Ψ_M along the eigenstates. Given the difficulty in calculating Ψ_M in most practical cases, we adopt a new formalism based on the *density operator* [6]. Let us consider a statistical ensemble of equally prepared physical states and suppose that the probability P_k for the system to be in the k^{th} normalized state $|\Psi_k(t)\rangle$ is known. The statistical mixture of states is represented by the density operator, defined as the weighted average of the projectors on the states $|\Psi_k(t)\rangle$:

$$\hat{\rho}(t) \equiv \sum_k P_k |\Psi_k(t)\rangle \langle \Psi_k(t)| \quad (\text{B.2})$$

where P_k are non negative ($P_k \geq 0$) and normalized $\sum_k P_k = 1$. The density

operator allows to access the expected value of a generic operator $\hat{A}(t)$ as:

$$\begin{aligned}\langle \hat{A}(t) \rangle &= \sum_k P_k \langle \Psi_k(t) | \hat{A} | \Psi_k(t) \rangle = \sum_m \sum_k P_k \langle \Psi_k(t) | \hat{A} | m \rangle \langle m | \Psi_k(t) \rangle \\ &= \sum_m \langle m | \hat{\rho} \hat{A} | m \rangle = \text{Tr}(\hat{\rho} \hat{A})\end{aligned}\quad (\text{B.3})$$

where we have introduced the completeness condition $\sum_m |m\rangle\langle m|$ and denoted with $\text{Tr}(\hat{O})$ the *trace* of a generic operator \hat{O} , calculated summing its diagonal elements in any complete set of states.

Fixing a basis, the values $\rho_{nm} = \langle m | \hat{\rho} | n \rangle$, are elements of the so called *density matrix*. The diagonal elements ρ_{nn} give the probability that the system is in the eigenstate $|n\rangle$ and are called *populations*. The off-diagonal terms imply instead that the system is in a coherent superposition of the eigenstates $|n\rangle$ and $|m\rangle$ with $n \neq m$ and provide the amplitude of what is called the *coherence* of the two states.

Let describe the time evolution of the density operator using its equation of motion. Let us first consider a pure state and calculate the time derivative of its density operator:

$$\frac{\partial \hat{\rho}}{\partial t} = \left(\frac{\partial}{\partial t} | \Psi(t) \rangle \right) \langle \Psi(t) | + | \Psi(t) \rangle \left(\frac{\partial}{\partial t} \langle \Psi(t) | \right). \quad (\text{B.4})$$

Using now the time-dependent Schrödinger equation $i\hbar [d\Psi(t)/dt] = \hat{H}\Psi(t)$ with a generic Hamiltonian \hat{H} , we obtain:

$$\begin{aligned}\frac{\partial \hat{\rho}}{\partial t} &= -\frac{i}{\hbar} \hat{H} | \Psi(t) \rangle \langle \Psi(t) | + \frac{i}{\hbar} | \Psi(t) \rangle \langle \Psi(t) | \hat{H} \\ &= -\frac{i}{\hbar} (\hat{H} \hat{\rho} - \hat{\rho} \hat{H})\end{aligned}\quad (\text{B.5})$$

The last equality in the equation has been specifically worked out for pure states. However, since pure and mixed states are related by a linear transformation (the density operator describing a mixed state is a superposition of pure state density operators), Equation B.5 can be also extended to mixed states and has, therefore, general validity. In a more compact notation

$$\frac{\partial \hat{\rho}}{\partial t} = -\frac{i}{\hbar} [\hat{H}, \hat{\rho}] \quad (\text{B.6})$$

The previous relation is known as **Liouville-Von Neumann equation** and rules the time evolution of the density operator.

The Liouville–Von Neumann equation, as the Schrödinger equation in the standard quantum mechanical approach, constitutes the starting point for the development of the time–dependent perturbation theory. Nevertheless, the two equations are formally very different: the former describes the time evolution of a matrix through the action of a commutator, the latter the time evolution of a vector ruled by a Hilbert operator. In order to make the Liouville–Von Neumann equation formally equivalent to Schrödinger Equation, we redefine the notation on the basis of the following points, moving to the **Liouville representation**:

- the density matrix is represented by a column vector. For a N –level system, the $N \times N$ density matrix will become a column of N^2 elements.
- we introduce the Liouville space operator $\mathbb{O}(t)$, called *superoperator*. Its action on an ordinary Hilbert operator \hat{A} is defined through:

$$\mathbb{O}(t)\hat{A} \equiv [\hat{\mathcal{O}}(t), \hat{A}]. \quad (\text{B.7})$$

It follows that Liouville space operators $\mathbb{O}(t)$ are represented by $N^2 \times N^2$ matrices.

These rules allow the construction of the Liouville space, that is the result of the cartesian product of two Hilbert spaces.

Within the Liouville representation, the Liouville–Von Neumann equation can be recast into the form

$$\frac{d\hat{\rho}}{dt} = -\frac{i}{\hbar}\mathbb{H}\hat{\rho}. \quad (\text{B.8})$$

The results of quantum mechanics can be used to search for a solution to Equation B.8. Such a solution represents the time evolution of $\hat{\rho}(t)$, which reads:

$$\rho(t) = \mathbb{U}(t, t_0) \rho(t_0). \quad (\text{B.9})$$

We introduced the *Liouville space propagator* $\mathbb{U}(t, t_0)$. By substituting Equation B.9 in Equation B.8, we find that \mathbb{U} satisfies the Liouville–Von Neumann equation:

$$\frac{\partial \mathbb{U}(t, t_0)}{\partial t} = -\frac{i}{\hbar}\mathbb{H}\mathbb{U}(t, t_0) \quad (\text{B.10})$$

with the initial condition $\mathbb{U}(t_0, t_0) = 1$. By integrating Equation B.10 and solving iteratively, it is possible to get an explicit expression for the superoperator

$\mathbb{U}(t, t_0)$. When the Hamiltonian is time-dependent, the formal solution for the time evolution superoperator becomes:

$$\mathbb{U}(t, t_0) = \mathcal{T} e^{-\frac{i}{\hbar} \int_{t_0}^t d\tau \mathbb{H}(\tau)} \quad (\text{B.11})$$

where \mathcal{T} is the time ordered exponential in Liouville space, an abbreviated notation for

$$\begin{aligned} \mathbb{U}(t, t_0) = 1 + \sum_{n=1}^{\infty} \left(-\frac{i}{\hbar}\right)^n \int_{t_0}^t d\tau_n \int_{t_0}^{\tau_n} d\tau_{n-1} \dots \int_{t_0}^{\tau_2} d\tau_1 \times \\ \times \mathbb{H}(\tau_n) \mathbb{H}(\tau_{n-1}) \dots \mathbb{H}(\tau_1) \end{aligned} \quad (\text{B.12})$$

Making use of Equation B.11, we get an exact solution of the Liouville-Von Neumann equation (Equation B.8)

$$\rho(t) = \left\{ \mathcal{T} e^{-\frac{i}{\hbar} \int_{-\infty}^t d\tau \mathbb{H}_I(\tau)} \right\} \rho(-\infty). \quad (\text{B.13})$$

The action of the superoperator $\mathbb{U}(t, t_0)$ is therefore:

$$\begin{aligned} \mathbb{U}(t, t_0) \rho(t_0) = 1 + \sum_{n=1}^{\infty} \left(-\frac{i}{\hbar}\right)^n \int_{t_0}^t d\tau_n \int_{t_0}^{\tau_n} d\tau_{n-1} \dots \int_{t_0}^{\tau_2} d\tau_1 \times \\ \times [\hat{H}(\tau_n), \dots [\hat{H}(\tau_2), [\hat{H}(\tau_1), \rho(t_0)]]] \dots \end{aligned} \quad (\text{B.14})$$

where we have used the definition of superoperator in Equation B.7.

The expression obtained in Equation B.12 treats the total Hamiltonian (that cannot be considered weak in general) perturbatively. Such a perturbative expansion only holds for short times, while breaking down for longer times. An immediate solution to this problem is to derive another expansion for $\mathbb{U}(t, t_0)$ which treats the interaction Hamiltonian perturbatively and the free Hamiltonian \hat{H}_0 exactly. As in the Hilbert space, this can be accomplished by reformulating the time evolution superoperator in the **interaction picture**. Within the interaction picture the time-dependence of the states is partially moved to the observables. The interaction picture in the Hilbert space is defined as follows:

$$\begin{aligned} |\Psi_I(t)\rangle &= e^{\frac{i}{\hbar} \hat{H}_0 t} |\Psi_S(t)\rangle \\ \hat{O}_I(t) &= e^{\frac{i}{\hbar} \hat{H}_0 t} \hat{O}_S e^{-\frac{i}{\hbar} \hat{H}_0 t} \end{aligned} \quad (\text{B.15})$$

where the subscripts S and I denote the Schrödinger and the interaction picture, respectively. Similarly, we can introduce the interaction picture in the Liouville

space by splitting the superoperator \mathbb{H} in a free Hamiltonian and an interaction term, respectively

$$\mathbb{H} = \mathbb{H}_0 + \mathbb{V} \quad (\text{B.16})$$

So we can rewrite the time evolution superoperator as the following product:

$$\mathbb{U}(t, t_0) = \mathbb{U}_0(t, t_0) \mathbb{U}_{int}(t, t_0) \quad (\text{B.17})$$

with

$$\begin{cases} \mathbb{U}_0(t, t_0) = \mathcal{T} e^{-\frac{i}{\hbar} \int_{t_0}^t d\tau \mathbb{H}_0(\tau)} \\ \mathbb{U}_{int}(t, t_0) = \mathcal{T} e^{-\frac{i}{\hbar} \int_{t_0}^t d\tau \mathbb{V}_{int}(\tau)} \end{cases} \quad (\text{B.18})$$

where we have defined $\mathbb{V}_{int}(\tau) = \mathbb{U}_0^\dagger(\tau, t_0) \mathbb{V}(\tau) \mathbb{U}_0(\tau, t_0)$, the superoperator \mathbb{V} in the interaction picture. We express the superoperator in Equation B.17 in its time-ordered expanded form:

$$\begin{aligned} \mathbb{U}(t, t_0) &= \mathbb{U}_0(t, t_0) + \sum_{n=1}^{\infty} \left(-\frac{i}{\hbar}\right)^n \int_{t_0}^t d\tau_n \int_{t_0}^{\tau_n} d\tau_{n-1} \dots \int_{t_0}^{\tau_2} d\tau_1 \times \\ &\quad \times \mathbb{U}_0(t, \tau_n) \mathbb{V}(\tau_n) \mathbb{U}_0(\tau_n, \tau_{n-1}) \mathbb{V}(\tau_{n-1}) \dots \\ &\quad \dots \mathbb{U}_0(\tau_2, \tau_1) \mathbb{V}(\tau_1) \mathbb{U}_0(\tau_1, t_0) \end{aligned} \quad (\text{B.19})$$

which is equivalent, using the \mathcal{T} operator, to:

$$\mathbb{U}(t, t_0) = \mathbb{U}_0(t, t_0) \mathcal{T} e^{-\frac{i}{\hbar} \int_{t_0}^t d\tau \mathbb{V}_{int}(\tau)} \quad (\text{B.20})$$

We can use these tools to work on the perturbative expansion of $\rho(t)$,

$$\hat{\rho}(t) = \rho^{(0)}(t) + \rho^{(1)}(t) + \rho^{(2)}(t) + \rho^{(3)}(t) + \dots \quad (\text{B.21})$$

where $\rho^{(n)}(t)$ is the n^{th} -order contribution in the electric field and $\rho^{(0)}(t) = \rho(-\infty)$ is the unperturbed (at thermal equilibrium) density matrix. Through this expansion any observable can be computed.

B.2 General solution for a forced harmonic oscillator

In this paragraph we derive a solution for the differential equation describing the dynamics of a forced harmonic oscillator [17]. We want to solve the following equation

$$\frac{d^2 \mathbf{Q}(t')}{dt'^2} + \omega_R^2 \frac{d\mathbf{Q}(t')}{dt'} = F(t) \quad (\text{B.22})$$

where $Q(t)$ is the amplitude of the oscillator as a function of time, ω_R is the system proper frequency and $F(t)$ is the driving force. We set as initial conditions, at time t_i , the maximum elongation and minimum momentum

$$\begin{cases} Q(t_i) = Q_0 \\ \frac{dQ}{dt}|_{t_i} = 0 \end{cases} \quad (\text{B.23})$$

Using Green's functions [100], we find the solution

$$Q(t) = Q_0 \cos(\omega_R(t - t_i)) + \int_0^\tau dt' \frac{\sin(\omega_R(t - t'))}{\omega_R} F(t') \quad (\text{B.24})$$

In this framework the force is impulsively applied only for a short time, τ , corresponding to the pulse duration. Hence the force, oscillating at ω_f with phase ϕ_f is approximated by the following function

$$F(t) = \begin{cases} 0, & t_i < t < 0 \\ f \sin(\omega_f t + \phi_f), & 0 < t < \tau \\ 0, & \tau < t < t_f \end{cases} \quad (\text{B.25})$$

Inserting this definition in Equation B.24 we obtain

$$Q(t) = Q_0 \cos(\omega_R(t - t_i)) + \int_0^\tau dt' \frac{\sin(\omega_R(t - t'))}{\omega_R} f \sin(\omega_f t' + \phi_f) \quad (\text{B.26})$$

The integral in the last term can be manipulated as follows

$$\begin{aligned} -\frac{f}{2\omega_R} \int_0^\tau dt' [\cos((\omega_f - \omega_R)t' + \omega_R t + \phi_f) - \cos((\omega_f + \omega_R)t' - \omega_R t + \phi_f)] &= \\ = -\frac{[\sin((\omega_f - \omega_R)\tau + \omega_R t + \phi_f) - \sin(\omega_R t + \phi_f)]}{\omega_f - \omega_R} + & (\text{B.27}) \\ + \frac{[\sin((\omega_f + \omega_R)\tau - \omega_R t + \phi_f) - \sin(-\omega_R t + \phi_f)]}{\omega_f + \omega_R} & \end{aligned}$$

The forcing is most effective when $\omega_f = \omega_R$. Using this condition and Equation B.27, Equation B.26 becomes

$$\begin{aligned} Q(t) = Q_0 \cos(\omega_R(t - t_i)) - \frac{\tau f}{2\omega_R} \cos(\omega_R t + \phi_f) + \\ + \frac{[\sin(2\omega_R \tau - \omega_R t + \phi_f) - \sin(-\omega_R t + \phi_f)]}{2\omega_R} \end{aligned} \quad (\text{B.28})$$

It is reasonable to assume that the force, being an oscillating function, rises and vanishes periodically, in other words that $\sin(\phi_f) = \sin(\omega_R \tau + \phi_f) = 0$, which gives a condition on the phase $\phi_f = n\pi$ and allows to rewrite the parameter $\tau = n \frac{\pi}{\omega_R}$. Making these assumptions Equation B.28 becomes

$$Q(t) = Q_0 \cos(\omega_R(t - t_i)) - \frac{\tau f}{2\omega_R} \cos(\omega_R t + \phi_f) \quad (\text{B.29})$$

Equation B.29 can be further simplified using the following relation in the complex plane

$$\begin{aligned} & a \cos(x + \phi_a) - b \cos(x + \phi_b) = \\ & = \sqrt{(a-b)^2 + 4ab \sin^2\left(\frac{\phi_a - \phi_b}{2}\right)} \cos\left(x + \frac{\phi_a + \phi_b}{2} + \arctan\left(\frac{a+b}{a-b} \tan\left(\frac{\phi_a - \phi_b}{2}\right)\right)\right) \end{aligned} \quad (\text{B.30})$$

resulting in the following expression for the amplitude of the harmonic driven oscillator

$$Q(t) = \sqrt{\left(Q_0 - \frac{\tau f}{2\omega_R}\right)^2 + 2\frac{Q_0 f \tau}{\omega_R} \sin^2\left(\frac{-\omega_R t_i - \phi_f}{2}\right)} \cos(\omega_R t + \Phi) \quad (\text{B.31})$$

where we defined the oscillator phase $\Phi = \frac{\omega_R t_i + \phi_f}{2} + \arctan\left(\frac{Q_0 + \frac{\tau f}{2\omega_R}}{Q_0 - \frac{\tau f}{2\omega_R}} \tan\left(\frac{\omega_R t_i - \phi_f}{2}\right)\right)$. Because of the simple relation between sine and cosine ($\sin(x) = \cos(x - \pi/2)$) we define an effective phase difference $\Delta\phi = -\omega_R t_i - \phi_f + \pi/2$ between vibration and force and rewrite Equation B.31 as

$$Q(t) = \sqrt{\left(Q_0 - \frac{\tau f}{2\omega_R}\right)^2 + \frac{Q_0 f \tau}{\omega_R} (1 - \sin(\Delta\phi))} \cos(\omega_R t + \Phi) \quad (\text{B.32})$$

The oscillator thus evolves at its proper frequency but its amplitude is influenced by the parameters of the applied force. We notice in particular the dependence on the force phase: when $\Delta\phi = -\pi/2$ the amplification of the amplitude is maximum, while when $\Delta\phi = +\pi/2$ the amplitude is decreased.

Appendix C

Pulse shaper calibrations

In this Appendix we provide the description of the pulse shaper calibration procedure.

C.1 Phase

Our pulse shaper based is based on a liquid crystal spatial light modulator. We described, in Section 3.1.2, the working principle of this device: despite being a phase only modulator, the application of a sawtooth grating allows to simultaneously and independently control the amplitude and phase of the spectral components which are dispersed onto the matrix. First of all, therefore, a "look up table" must be generated for the effective liquid crystals phase values to match the software generated values. These might not correspond exactly as the liquid crystals have a frequency dependent response, there could be imperfections in the electrodes, and so on.

To calibrate the phase, a binary phase grating is applied to the liquid crystal matrix, and the diffracted intensity is measured by one linear photodiode array as the amplitude of the grating is scanned in the range allowed by the SLM electronics. In Figure C.1 we show the appearance of such a pattern for three amplitude values. The measured intensity is shown in panel c) of the same Figure. As the intensity drops to zero multiple times within the voltage extrema, we deduce that the liquid crystals undergo more than one complete rotation during the scan. We focus on the first rotation as this will be enough to produce a $0 - 2\pi$ phase interval, and it will allow us to increase the number of points within the range, therefore increasing the voltage, and phase, sensi-

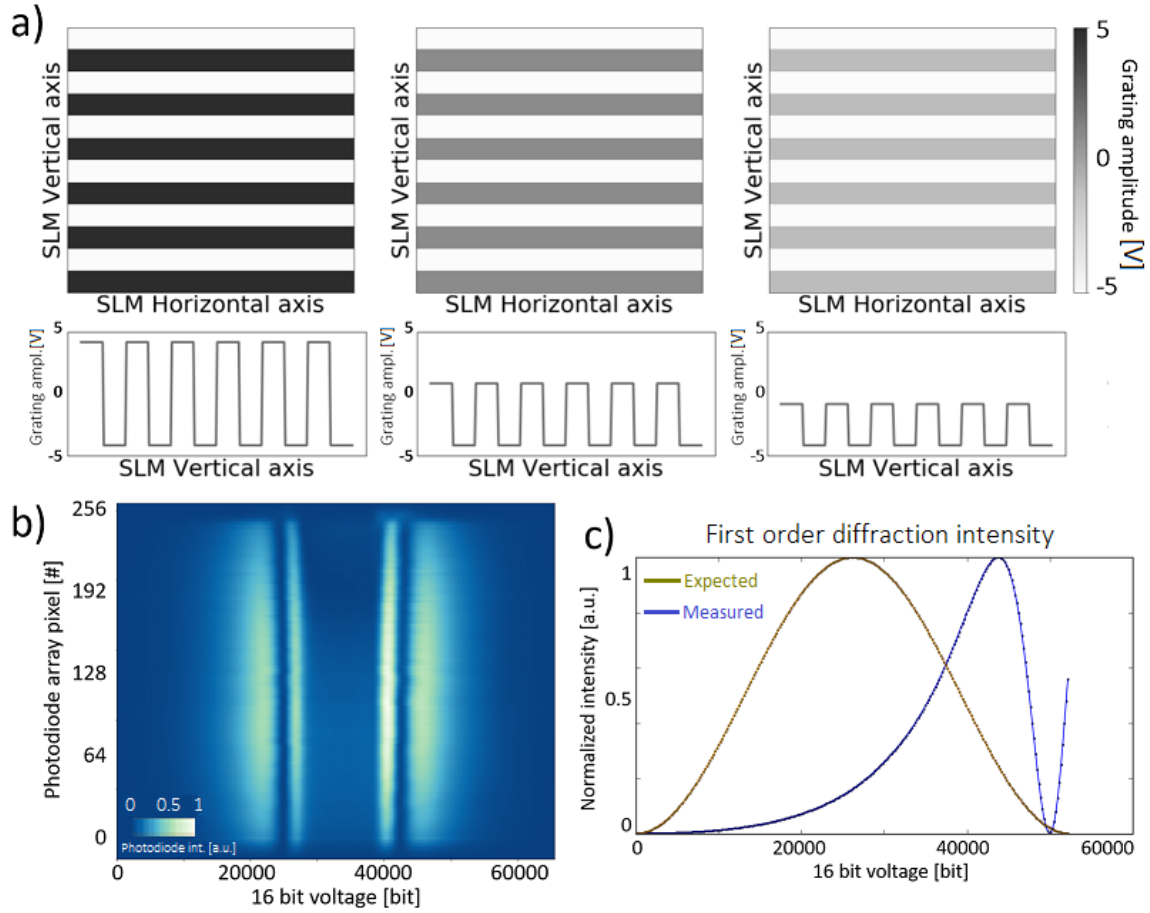


Figure C.1: a) Applied pattern to reproduce a binary grating. The bottom plots are vertical cuts representing the grating profile. b) First order diffraction intensity as a function of the applied voltage, in the full available range. c) Integral of the diffraction intensity along the wavelength axis, in the voltage range where the phase goes from 0 to 2π (blue curve), compared to the expected efficiency (brown curve).

tivity. Because we do not detect any appreciable frequency dependence of the diffracted intensity, we integrate the photodiode array signal and compare the curve to the expected diffraction efficiency. The latter reads [50]

$$I_{m=1} \propto \sin^2(A_G/2) \quad (\text{C.1})$$

where A_G is the amplitude of the binary diffraction grating. The function mapping each point of the measured curve onto the expected one allows to translate the effective voltage into any desired phase values.

C.2 Amplitude

To account for further imperfections in the device, an amplitude calibration of the applied sawtooth grating is performed. This must necessarily follow the phase calibration, to guarantee that a proper sawtooth is applied in the vertical direction.

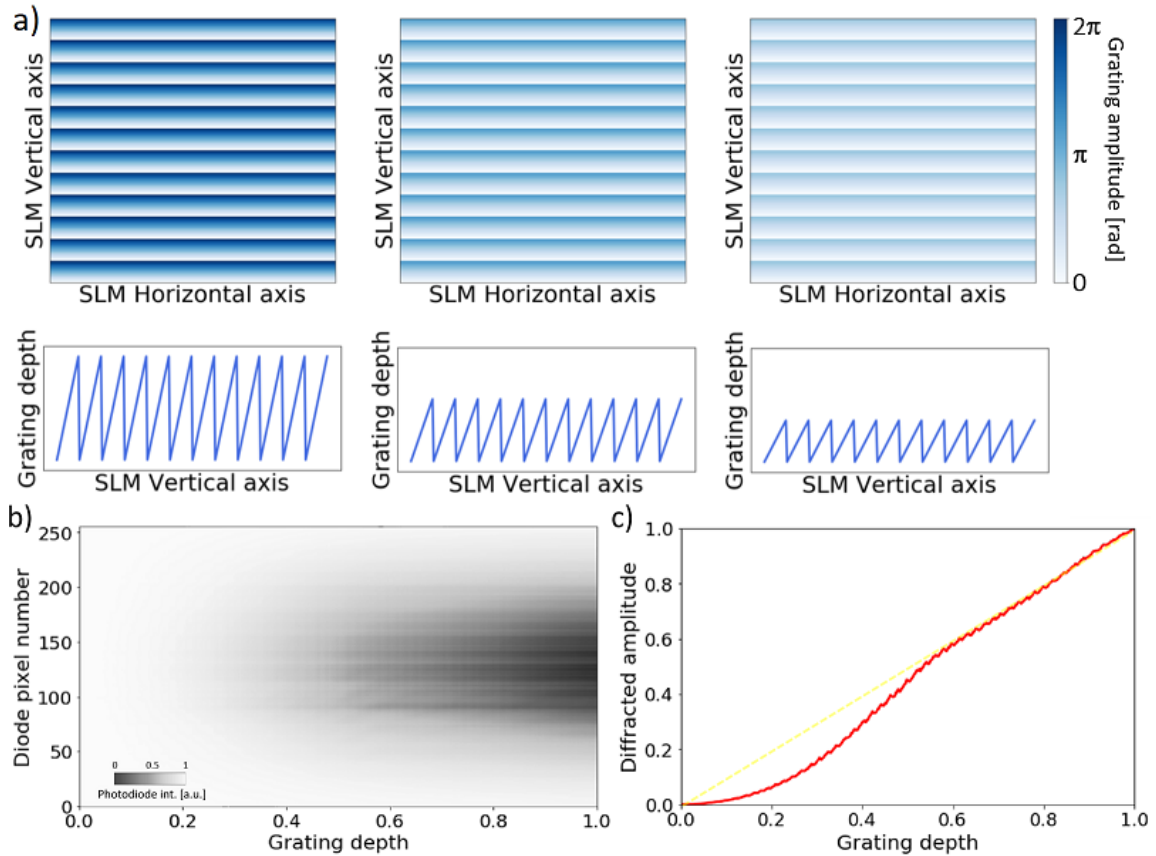


Figure C.2: a) Applied pattern to reproduce a sawtooth grating. The bottom plots are vertical cuts representing the sawtooth profile. b) First order diffraction intensity as a function of the applied phase, normalized to 2π . c) Integral of the diffraction intensity along the wavelength axis (red curve), compared to the diagonal representing a linear relationship.

To accomplish an amplitude calibration, a sawtooth function must be applied all along the SLM matrix, and its amplitude has to be scanned, as shown at the top of Figure C.2. As the measured diffracted intensity is only weakly dependent on the wavelength, we normalize the measured intensity at each wavelength and integrate the intensity along the wavelength axis. The amplitude of the

diffracted field is expected to be linearly proportional to the amplitude of the sawtooth grating, as reported in Equation 3.10 [50]. Therefore any variations are encoded in a second "look up table" that is used by the software to adjust the voltage values in order to produce a scattering intensity varying linearly with the sawtooth amplitude.

C.3 Frequency

A relationship must be found between the wavelength content of the pulse, the SLM pixel and the photodiode pixel. This can only be done with the aid of some external device which is able to recognize or select specific wavelengths.

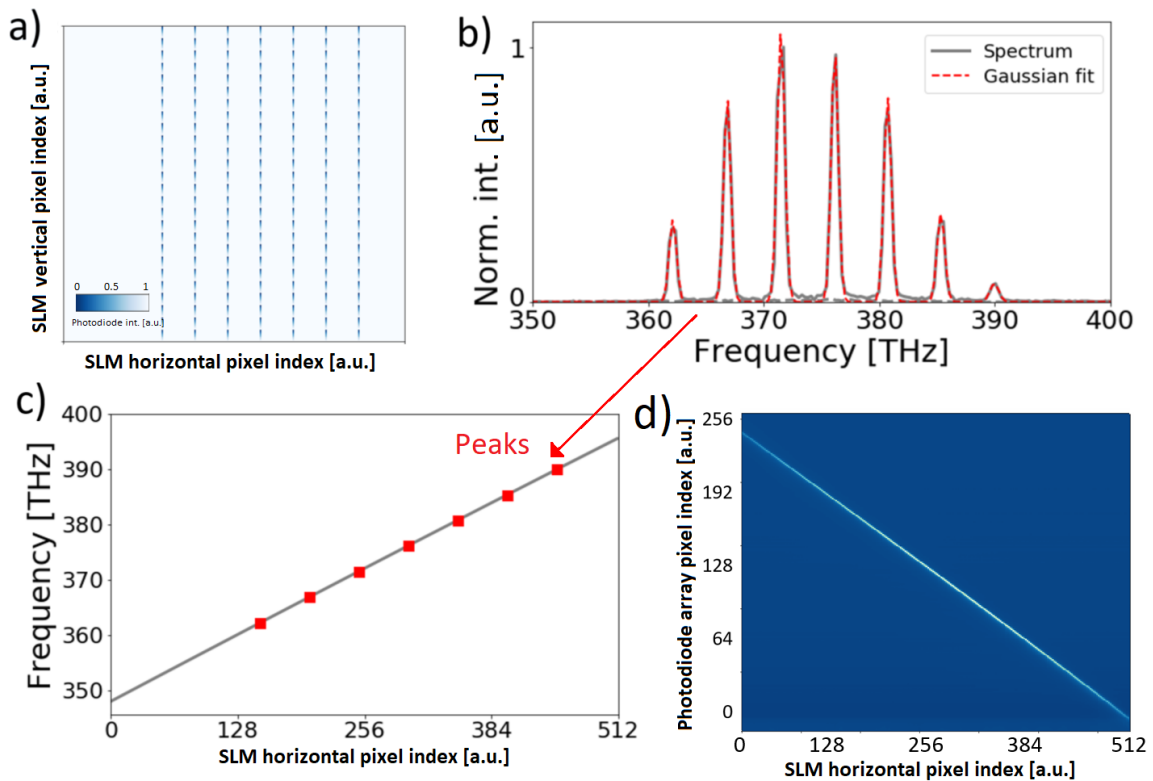


Figure C.3: a) Pattern consisting of multiple narrow diffraction gratings, and b) measured intensity spectrum as a function of the calculated frequency scale. c) Fit of the frequency at the peak position as a function of the SLM pixel. d) Map of the peak as measured by one of two photodiode arrays, as a function of the its pixel index and of the SLM pixel index.

A pattern is applied on the SLM matrix consisting of narrow sawtooth gratings, with pixel width roughly corresponding to the horizontal dimension of a

frequency component diffraction spot. The comb is measured, after the pulse shaper, using the aforementioned spectrometer, which allows to retrieve the frequency at the centre of each peak. Therefore a relation between frequency and SLM pixel is found. A pattern consisting of a single narrow diffraction grating is used to scan the SLM horizontal pixel and build a map consisting of a single peak whose coordinates are the SLM pixel (given) and the the single photodiode array pixel. Therefore the dispersion is calculated on each of the photodiode arrays independently. The pattern consisting of multiple spikes is finally exploited to optimize the alignment of the beam onto the photodiode arrays, in order to match the dispersion. In practice, the photodiode arrays are translated manually by means of mechanical stages, up to the point when the measured narrow spikes overlap.

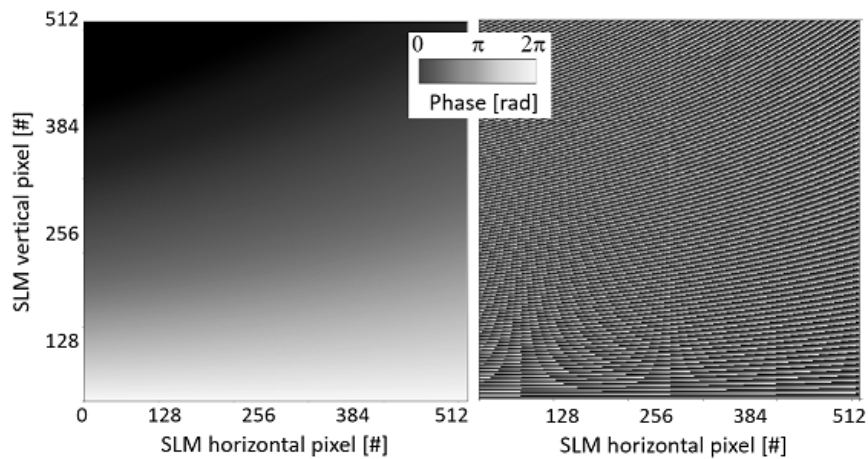


Figure C.4: *Phase offset applied along the horizontal direction to compensate for the output angle mismatch (left). Same pattern after wrapping the voltage pattern along the vertical direction to create a sawtooth grating (right).*

Finally, one can perform the frequency correction that allows to reshape the beam focus and eliminate the frequency chirp along the vertical direction, as shown in Figure 3.5. A phase offset is applied along the horizontal direction, then the map is wrapped along the vertical direction to create a sawtooth, as shown in Figure C.4.

Publications

- ✓ **Giorgia Sparapassi**^{*}, Jonathan Owen Tollerud^{*}, Angela Montanaro, Shahaf Asban, Filippo Glerean, Francesca Giusti, Alexandre Marciniak, Georgios Kouroussias, Fulvio Billè, Federico Cilento, Shaul Mukamel, & Daniele Fausti (**2019**). *Femtosecond covariance spectroscopy*. Proceedings of the National Academy of Sciences, 116(12), 5383–5386. [14]
- ✓ Filippo Glerean, Stefano Marcantoni, **Giorgia Sparapassi**, Andrea Blason, Martina Esposito, Fabio Benatti, & Daniele Fausti (**2019**). *Quantum model for Impulsive Stimulated Raman Scattering*. Journal of Physics B: Atomic, Molecular and Optical Physics. [15]
- ✓ Francesca Giusti, Alexandre Marciniak, Francesco Randi, **Giorgia Sparapassi**, Federico Boschini, Hiroshi Eisaki, Martin Greven, Andrea Damascelli, Adolfo Avella, & Daniele Fausti (**2019**). *Signatures of Enhanced Superconducting Phase Coherence in Optimally Doped $\text{Bi}_2\text{Sr}_2\text{Y}_{0.08}\text{Ca}_{0.92}\text{Cu}_2\text{O}_{8+\delta}$ Driven by Mid Infrared Pulse Excitations*. Physical Review Letters, 122(6), 067002. [101]
- ✓ **Giorgia Sparapassi**, Jonathan Owen Tollerud, Filippo Glerean, & Daniele Fausti (**2018**). *Noise Correlation Spectroscopy for spectroscopic measurements of low energy modes*. In CLEO: Applications and Technology (pp. ATh30–7). Optical Society of America. [102]
 - Alexandre Marciniak, Stefano Marcantoni, Francesca Giusti, Filippo Glerean, **Giorgia Sparapassi**, Tobia Nova, Andrea Cartella, Stefano Latini, Francesco Valiera, Andrea Cavalleri, Angel Rubio, Jerome Van Der Brink, Fabio Benatti, & Daniele Fausti *Vibrational coherent control of localized d-d electronic excitation*. In preparation [75]
- In preparation: *Coherent Phonons in Femtosecond Covariance Spectroscopy*.
- In preparation: *Femtosecond Covariance Spectroscopy in Resonant Conditions*.

^{*}Contributed equally to the work.

References

- [1] G. B. Benedek and F. M. H. Villars. *Physics with illustrative examples from Medicine and Biology*. Springer Science & Business Media, 2000.
- [2] F. Träger. *Springer handbook of lasers and optics*. Springer Science & Business Media, 2012.
- [3] N. Bloembergen. *Nonlinear Optics*. World Scientific, 1996.
- [4] R. W. Boyd. *Nonlinear Optics*. Elsevier, 2003.
- [5] E. O. Potma and S. Mukamel. “Theory of Coherent Raman Scattering”. In: *Coherent Raman Scattering Microscopy*. Ed. by J. X. Cheng. Ed. by X. Sunney Xie. CRC Press. Taylor & Francis Group, LLC., 2013. ISBN: 978-1-4398-6765-5.
- [6] S. Mukamel. *Principles of nonlinear optical spectroscopy*. Oxford University Press, 1995.
- [7] M. Esposito et al. “Photon number statistics uncover the fluctuations in non-equilibrium lattice dynamics”. In: *Nature communications* 6 (2015), p. 10249.
- [8] L. Gammaitoni et al. “Stochastic Resonance”. In: *Reviews of Modern Physics* 70.1 (1998), p. 223.
- [9] F. Caruso et al. “Highly efficient energy excitation transfer in light-harvesting complexes: The fundamental role of noise-assisted transport”. In: *The Journal of Chemical Physics* 131.10 (2009), 09B612.
- [10] X. G. Xu et al. “Noise autocorrelation spectroscopy with coherent Raman scattering”. In: *Nature Physics* 4.2 (2008), p. 125.
- [11] L. J. Frasinski, K. Codling, and P. A. Hatherly. “Covariance mapping: A correlation method applied to multiphoton multiple ionization”. In: *Science* 246.4933 (1989), pp. 1029–1031.

- [12] I. Noda and Y. Ozaki. *Two-dimensional correlation spectroscopy: applications in vibrational and optical spectroscopy*. John Wiley & Sons, 2005.
- [13] J. Laane, ed. *Frontiers and Advances in Molecular Spectroscopy*. Elsevier, 2017.
- [14] J. O. Tollerud et al. “Femtosecond Covariance Spectroscopy”. In: *Proceedings of the National Academy of Sciences* 116.12 (2019), pp. 5383–5386.
- [15] F. Glerean et al. “Quantum model for Impulsive Stimulated Raman Scattering”. In: *Journal of Physics B: Atomic, Molecular and Optical Physics* (2019).
- [16] A. Montanaro. *Noise Correlation Spectroscopy*. 2018. URL: http://www.inceptproject.eu/wp-content/uploads/2019/09/Tesi_Def_Montanaro_Master_18.pdf.
- [17] F. Glerean. *Noise Correlation Spectroscopy for Impulsive Stimulated Raman Scattering*. 2017. URL: http://www.inceptproject.eu/wp-content/uploads/2019/09/Tesi_Filippo_Glerean_Master_17.pdf.
- [18] Chandrasekhara Venkata Raman and Kariamanikkam Srinivasa Krishnan. “A new type of secondary radiation”. In: *Nature* 121.3048 (1928), pp. 501–502.
- [19] “Light Scattering in Solids VIII”. In: *Topics in Applied Physics (Springer, Berlin, 2000)* 76 (2000).
- [20] W. H. Weber and R. Merlin. *Raman scattering in materials science*. Vol. 42. Springer Science & Business Media, 2013.
- [21] J.-X. Cheng and X. S. Xie. *Coherent Raman scattering microscopy*. CRC press, 2016.
- [22] E. Smith and G. Dent. *Modern Raman spectroscopy: a practical approach*. John Wiley & Sons, 2019.
- [23] A. Laubereau and W. Kaiser. “Vibrational dynamics of liquids and solids investigated by picosecond light pulses”. In: *Reviews of Modern Physics* 50.3 (1978), p. 607.
- [24] P. Kukura, D. W. McCamant, and R. A. Mathies. “Femtosecond stimulated Raman spectroscopy”. In: *Annu. Rev. Phys. Chem.* 58 (2007), pp. 461–488.
- [25] J.-X. Cheng and X. S. Xie. “Coherent anti-Stokes Raman scattering microscopy: instrumentation, theory, and applications”. In: (2004).

- [26] Toshiaki Hattori, Akira Terasaki, and Takayoshi Kobayashi. “Coherent Stokes Raman scattering with incoherent light for vibrational–dephasing–time measurement”. In: *Physical Review A* 35.2 (1987), p. 715.
- [27] M. J. Stimson, D. J. Ulness, and A. C. Albrecht. “Frequency and time resolved coherent Stokes Raman scattering in CS₂ using incoherent light”. In: *Chemical Physics Letters* 263.1–2 (1996), pp. 185–190.
- [28] C. W. Freudiger et al. “Label-free biomedical imaging with high sensitivity by stimulated Raman scattering microscopy”. In: *Science* 322.5909 (2008), pp. 1857–1861.
- [29] R. C. Prince, R. R. Frontiera, and E. O. Potma. “Stimulated Raman scattering: from bulk to nano”. In: *Chemical reviews* 117.7 (2017), pp. 5070–5094.
- [30] S. Chandra, A. Compaan, and E. Wiener–Avnear. “Coherent Raman scattering with three lasers”. In: *Applied Physics Letters* 33.10 (1978), pp. 867–869.
- [31] H. Frostig et al. “Single-pulse stimulated Raman scattering spectroscopy”. In: *Optics letters* 36.7 (2011), pp. 1248–1250.
- [32] Y.-X. Yan, E. B. Gamble Jr., and K. A. Nelson. “Impulsive stimulated scattering: General importance in femtosecond laser pulse interactions with matter, and spectroscopic applications”. In: *The Journal of chemical physics* 83.11 (1985), pp. 5391–5399.
- [33] S. Ruhman, A. G. Joly, and K. A. Nelson. “Coherent molecular vibrational motion observed in the time domain through impulsive stimulated Raman scattering”. In: *IEEE journal of quantum electronics* 24.2 (1988), pp. 460–469.
- [34] A. M. Weiner et al. “Femtosecond multiple-pulse impulsive stimulated Raman scattering spectroscopy”. In: *JOSA B* 8.6 (1991), pp. 1264–1275.
- [35] C. Mencuccini and V. Silvestrini. *Fisica II*. Liguori Editore, 1995.
- [36] C. A. Marx, U. Harbola, and S. Mukamel. “Nonlinear optical spectroscopy of single, few, and many molecules: Nonequilibrium Green’s function QED approach”. In: *Physical Review A* 77.2 (2008), p. 022110.

- [37] O. Roslyak, C. A. Marx, and S. Mukamel. “Generalized Kramers–Heisenberg expressions for stimulated Raman scattering and two–photon absorption”. In: *Physical Review A* 79.6 (2009), p. 063827.
- [38] S. Mukamel and S. Rahav. “Ultrafast nonlinear optical signals viewed from the molecule’s perspective: Kramers–Heisenberg transition–amplitudes versus susceptibilities”. In: *Advances in atomic, molecular, and optical physics*. Vol. 59. Elsevier, 2010, pp. 223–263.
- [39] R. Loudon. *The quantum theory of light*. 3rd edition. Oxford University Press, 2000.
- [40] N. W. Ashcroft and N. D. Mermin. “Solid State Physics”. In: (1976).
- [41] Andy Rundquist et al. “Polarization–dependent detection of impulsive stimulated Raman scattering in α -quartz”. In: *Journal of Modern Optics* (2005).
- [42] M. M. Wefers, H. Kawashima, and K. A. Nelson. “Optical control over two–dimensional lattice vibrational trajectories in crystalline quartz”. In: *The Journal of Chemical Physics* 108.24 (1998), pp. 10248–10255. DOI: 10.1063/1.476485.
- [43] J. F. Scott and S. P. S. Porto. “Longitudinal and Transverse Optical Lattice Vibrations in Quartz”. In: *Phys. Rev.* 161 (3 Sept. 1967), pp. 903–910. DOI: 10.1103/PhysRev.161.903.
- [44] *Legend Elite Series*. Coherent Inc. URL: <https://www.coherent.com/lasers/laser/legend-elite-series>.
- [45] J. C. Diels and W. Rudolph. *Ultrashort laser pulse phenomena*. Elsevier, 2006.
- [46] A. Weiner. *Ultrafast optics*. John Wiley & Sons, 2011.
- [47] Joanna Rose. *Tools made of light. The Nobel Prize in Physics 2018 – Popular Science Background*. Ed. by Anders Irbäck Olga Botner Gunnar Ingelman and the Nobel Committee for Physics Mats Larsson. The Royal Swedish Academy of Sciences. 2018. URL: https://s3.eu-de.cloud-object-storage.appdomain.cloud/kva-image-pdf/2019/10/pop_fy_en_18.pdf.
- [48] A. Monmayrant, S. Weber, and B. Chatel. “A newcomer’s guide to ultra–short pulse shaping and characterization”. In: *Journal of Physics B: Atomic, Molecular and Optical Physics* 43.10 (2010), p. 103001.

- [49] A. M. Weiner. “Femtosecond pulse shaping using spatial light modulators”. In: *Review of scientific instruments* 71.5 (2000), pp. 1929–1960.
- [50] J. C. Vaughan et al. “Diffraction-based femtosecond pulse shaping with a two-dimensional spatial light modulator”. In: *Optics letters* 30.3 (2005), pp. 323–325.
- [51] D. N. Nikogosyan. “Beta barium borate (BBO)”. In: *Applied Physics A* 52.6 (1991), pp. 359–368.
- [52] M. Bradler, P. Baum, and E. Riedle. “Femtosecond continuum generation in bulk laser host materials with sub- μ J pump pulses”. In: *Applied Physics B* 97.3 (2009), p. 561.
- [53] R. Trebino et al. “Measuring ultrashort laser pulses in the time-frequency domain using frequency-resolved optical gating”. In: *Review of Scientific Instruments* 68.9 (1997), pp. 3277–3295.
- [54] J.-C. M. Diels et al. “Control and measurement of ultrashort pulse shapes (in amplitude and phase) with femtosecond accuracy”. In: *Applied Optics* 24.9 (1985), pp. 1270–1282.
- [55] R. Beach and S. R. Hartmann. “Incoherent photon echoes”. In: *Physical Review Letters* 53.7 (1984), p. 663.
- [56] N. Morita and T. Yajima. “Ultrahigh-time-resolution coherent transient spectroscopy with incoherent light”. In: *Physical Review A* 30.5 (1984), p. 2525.
- [57] M. A. Dugan, J. S. Melinger, and A. C. Albrecht. “Terahertz oscillations from molecular liquids in CSRS/CARS spectroscopy with incoherent light”. In: *Chemical physics letters* 147.5 (1988), pp. 411–419.
- [58] K. Meyer et al. “Noisy optical pulses enhance the temporal resolution of pump-probe spectroscopy”. In: *Physical Review Letters* 108.9 (2012), p. 098302.
- [59] K. Meyer et al. “Temporal resolution beyond the average pulse duration in shaped noisy-pulse transient absorption spectroscopy”. In: *Applied optics* 55.36 (2016), pp. 10318–10322.

- [60] D. J. Ulness and A. C. Albrecht. “Four-wave mixing in a Bloch two-level system with incoherent laser light having a Lorentzian spectral density: analytic solution and a diagrammatic approach”. In: *Physical Review A* 53.2 (1996), p. 1081.
- [61] P. P. Aung et al. “Effects of beam polarization on coherent anti-Stokes Raman scattering using noisy light”. In: *Journal of Raman Spectroscopy: An International Journal for Original Work in all Aspects of Raman Spectroscopy, Including Higher Order Processes, and also Brillouin and Rayleigh Scattering* 36.5 (2005), pp. 409–419.
- [62] G. Fumero et al. “On the Resolution Limit of Femtosecond Stimulated Raman Spectroscopy: Modelling Fifth-Order Signals with Overlapping Pulses”. In: *ChemPhysChem* 16.16 (2015), pp. 3438–3443.
- [63] J.-X. Cheng, L. D. Book, and X. S. Xie. “Polarization coherent anti-Stokes Raman scattering microscopy”. In: *Optics letters* 26.17 (2001), pp. 1341–1343.
- [64] N. Akansu A. et al. *Multiresolution signal decomposition: transforms, sub-bands, and wavelets*. Academic press, 2001.
- [65] G. P. Agrawal. “Modulation instability induced by cross-phase modulation”. In: *Physical Review Letters* 59.8 (1987), p. 880.
- [66] B. Akhremitchev, C. Wang, and G. C. Walker. “A femtosecond absorption spectrometer tunable from 50000 to 800 cm^{-1} : Nonlinear optics and pump/probe geometries”. In: *Review of scientific instruments* 67.11 (1996), pp. 3799–3805.
- [67] G. Batignani et al. “Genuine dynamics vs cross phase modulation artifacts in femtosecond stimulated Raman spectroscopy”. In: *ACS Photonics* 6.2 (2019), pp. 492–500.
- [68] S. L. Palfrey and T. F. Heinz. “Coherent interactions in pump-probe absorption measurements: the effect of phase gratings”. In: *Journal of the Optical Society of America, B* 2.4 (1985), pp. 674–679.
- [69] D. Zhang et al. “Spectrally modulated stimulated Raman scattering imaging with an angle-to-wavelength pulse shaper”. In: *Optics Express* 21.11 (2013), pp. 13864–13874.

- [70] S. Lim et al. “Spectral modulation of stimulated Raman scattering signal: Beyond weak Raman pump limit”. In: *Journal of Raman Spectroscopy* 49.4 (2018), pp. 607–620.
- [71] M. J. Stimson, D. J. Ulness, and A. C. Albrecht. “Time-resolved coherent Raman spectroscopy controlled by spectrally tailored noisy light”. In: *Journal of Raman spectroscopy* 28.8 (1997), pp. 579–587.
- [72] M. Hase and M. Kitajima. “Interaction of coherent phonons with defects and elementary excitations”. In: *Journal of Physics: Condensed Matter* 22.7 (2010), p. 073201.
- [73] C. Giannetti et al. “Disentangling thermal and nonthermal excited states in a charge-transfer insulator by time- and frequency-resolved pump-probe spectroscopy”. In: *Physical Review B* 80.23 (2009), p. 235129.
- [74] Z. V. Popović et al. “Phonons in CuGeO_3 studied using polarized far-infrared and Raman-scattering spectroscopies”. In: *Physical Review B* 52.6 (1995), p. 4185.
- [75] A. Marciniak et al. “Vibrational coherent control of localized d-d electronic excitation”. 2019. In preparation.
- [76] G. Margaritondo and P. Rebernik Ribic. “A simplified description of X-ray free-electron lasers”. In: *Journal of synchrotron radiation* 18.2 (2011), pp. 101–108.
- [77] E. Allaria et al. “Highly coherent and stable pulses from the FERMI seeded free-electron laser in the extreme ultraviolet”. In: *Nature Photonics* 6.10 (2012), p. 699.
- [78] *The Elastic and Inelastic Scattering (EIS) beamline*. URL: <https://www.elettra.trieste.it/lightsources/fermi/fermi-beamlines/eis/eis-home.html>.
- [79] O. Y. Gorobtsov et al. “Seeded X-ray free-electron laser generating radiation with laser statistical properties”. In: *Nature Communications* 9.1 (2018), p. 4498.
- [80] M. Smeu et al. “Electronic properties of Si (111)- 7×7 and related reconstructions: Density functional theory calculations”. In: *Physical Review B* 85.19 (2012), p. 195315.
- [81] A. Marinelli et al. “Optical shaping of X-ray free-electron lasers”. In: *Physical Review Letters* 116.25 (2016), p. 254801.

- [82] E. Roussel et al. “Multicolor high-gain free-electron laser driven by seeded microbunching instability”. In: *Physical Review Letters* 115.21 (2015), p. 214801.
- [83] J. van den Brink. *Lecture Notes of the Autumn School on Correlated Electrons 2016*. Ed. by E. Pavarini et al. Forschungszentrum Jülich GmbH, Institute for Advanced Simulation, 2016. Chap. Resonant Inelastic X-ray Scattering on Elementary Excitations.
- [84] C. Weninger and N. Rohringer. “Stimulated resonant x-ray Raman scattering with incoherent radiation”. In: *Physical Review A* 88.5 (2013), p. 053421.
- [85] C. Weninger et al. “Stimulated electronic x-ray Raman scattering”. In: *Physical review letters* 111.23 (2013), p. 233902.
- [86] V. Kimberg and N. Rohringer. “Stochastic stimulated electronic x-ray Raman spectroscopy”. In: *Structural Dynamics* 3.3 (2016), p. 034101.
- [87] C. Monney et al. “Determining the short-range spin correlations in the spin-chain Li_2CuO_2 and CuGeO_3 compounds using resonant inelastic X-ray scattering”. In: *Physical Review Letters* 110.8 (2013), p. 087403.
- [88] T. P. Devereaux and R. Hackl. “Inelastic light scattering from correlated electrons”. In: *Reviews of Modern Physics* 79.1 (2007), p. 175.
- [89] E. Wolf. “Optics in terms of observable quantities”. In: *Il Nuovo Cimento (1943-1954)* 12.6 (1954), pp. 884–888.
- [90] P. Pääkkönen et al. “Partially coherent Gaussian pulses”. In: *Optics Communications* 204.1–6 (2002), pp. 53–58.
- [91] H. Lajunen, P. Vahimaa, and J. Tervo. “Theory of spatially and spectrally partially coherent pulses”. In: *JOSA A* 22.8 (2005), pp. 1536–1545.
- [92] E. Wolf. *Introduction to the Theory of Coherence and Polarization of Light*. Cambridge University Press, 2007.
- [93] G. S. Agarwal, G. Gbur, and E. Wolf. “Coherence properties of sunlight”. In: *Optics Letters* 29.5 (2004), pp. 459–461.
- [94] Y.-C. Cheng and G. R. Fleming. “Dynamics of light harvesting in photosynthesis”. In: *Annual review of physical chemistry* 60 (2009), pp. 241–262.

- [95] F. Fassioli, A. Olaya-Castro, and G. D. Scholes. “Coherent energy transfer under incoherent light conditions”. In: *The journal of physical chemistry letters* 3.21 (2012), pp. 3136–3142.
- [96] D. B. Turner et al. “Two-dimensional electronic spectroscopy using incoherent light: theoretical analysis”. In: *The Journal of Physical Chemistry A* 117.29 (2013), pp. 5926–5954.
- [97] D. B. Turner et al. “Coherent multidimensional optical spectra measured using incoherent light”. In: *Nature Communications* 4.1 (2013), pp. 1–9.
- [98] D. J. Ulness and D. B. Turner. “Lineshape analysis of coherent multidimensional optical spectroscopy using incoherent light”. In: *The Journal of chemical physics* 142.21 (2015), p. 212420.
- [99] D. J. Ulness and D. B. Turner. “Coherent two-quantum two-dimensional electronic spectroscopy using incoherent light”. In: *The Journal of Physical Chemistry A* 121.48 (2017), pp. 9211–9220.
- [100] D. B. Kaplan. *Solving the damped harmonic oscillator using Green functions*. Institute for Nuclear Theory – University of Washington. 2001. URL: http://www.int.washington.edu/users/dbkaplan/228_01/green.pdf.
- [101] F. Giusti et al. “Signatures of Enhanced Superconducting Phase Coherence in Optimally Doped $\text{Bi}_2\text{Sr}_2\text{Y}_{0.08}\text{Ca}_{0.92}\text{Cu}_2\text{O}_{8+\delta}$ Driven by Midinfrared Pulse Excitations”. In: *Physical Review Letters* 122.6 (2019), p. 067002.
- [102] G. Sparapassi et al. “Noise Correlation Spectroscopy for spectroscopic measurements of low energy modes”. In: *CLEO: Applications and Technology*. Optical Society of America. 2018, ATTh3O–7.